Local Structure of Al-based Amorphous Alloys after Microalloying by Element Substitution and after Ball Milling

vorgelegt von
Yao Liu

von der Fakultät III - Prozesswissenschaften
der Technischen Universität Berlin
zur Erlangung des akademischen Grades

Doktor der Ingenieurwissenschaften
-Dr.-Ing.-

genehmigte Dissertation

angefertigt am Helmholtz-Zentrum Berlin für Materialien und Energie
Institut für Angewandte Materialforschung

Promotionsausschuss:

Vorsitzender: Prof. Dr. rer. nat. Helmut Schubert
Berichter: Prof. Dr. rer. nat. John Banhart
Berichter: Prof. Dr. rer. nat. Gerhard Wilde

Tag der wissenschaftlichen Aussprache: 08. Dezember 2011

Berlin, Oktober 2011

D83

Abstract

Structural stability of glassy $Al_{85}Ni_{10}La_5$ as-atomized powder was investigated after ball milling using scanning electron microscopy (SEM), differential scanning calorimetry (DSC), X-ray diffractometry (XRD), transmission electron microscopy (TEM), and X-ray absorption spectroscopy (XAS). Fcc-Al nanocrystals were found after ball milling. The crystallization behaviour upon thermal treatment depends on the deformation level. Because the solute atoms Ni and La diffuse out of the Al crystal and create a solute rich area around the crystal, the composition of the residual amorphous phase changes towards higher contents of Ni and La. Furthermore, crystallization under ball milling depends on the ball milling temperature indicating a combined role of temperature and plastic deformation for the crystallization behavior of $Al_{85}Ni_{10}La_5$ powder during ball milling. The coordination number $\boldsymbol{N}$ of Ni obtained by XAS measurements decreases exponentially as a function of ball milling time. The exponential decrease in $\boldsymbol{N}$(Ni) during plastic deformation was described in the frame of a shear band model, in which $\boldsymbol{N}$(Ni) is 6 outside the shear bands and 5 within the shear bands.

The local structures around nickel and cobalt atoms in $Al_{86}Ni_8Y_6$ and $Al_{86}Ni_6Co_2Y_{4.5}La_{1.5}$ bulk amorphous alloys were measured by XAS. The same local structure around Ni and Co atoms was found which is ascribed to a site substitution of Ni by Co atoms in the amorphous structure. The configurational entropy is estimated to be the main thermodynamic driving force for the increase in glass forming ability when substituting Ni by Co and Y by La. The cluster-line model is not supported by our results.

The local structure after minor substitution of Ni by Co, Ge, Pd, Ag and Zr in Al-Ni-Y and Al-Ni-La systems was also investigated by XAS. Three groups of elements which are “small”, “medium” and “large” atoms were identified and discussed in terms of coordination number as a function of the interatomic distance. The most striking result is the bond-shortening between the absorbing atoms and Al resulting in large changes of the effective radii compared to their metallic radii and a concomitant reduction of the number of nearest neighbours. This effect is most pronounced for the small atoms, especially for Ag atoms, allowing the Ag atoms to have the same local environment as Ni and Co.

Acknowledgements

I have been very fortunate with my supervisor, Prof. John Banhart, who offered me the opportunity to do my PhD at the Institute of Applied Materials of the Helmholtz-Zentrum Berlin für Materialien und Energie (HZB). I would like to thank the second examiner Prof. Gerhard Wilde, who is ready to examine my thesis. I would like to thank Prof. Helmut Schubert for being the chairman during the defence of my PhD. I would like to express my greatest gratitude to PD Dr. Gerhard Schumacher, who guided me through the science of metallic glasses during my PhD. With his enthusiasm, his inspiration, and his great efforts to explain things clearly and simply, he helped to make scientific fun for me. Throughout my thesis-writing period, he provided encouragement, sound advice, good teaching, good company, and lots of good ideas. I would have been lost without him.

I would like to thank Dr. Ivo Zizak and Dr. Heinrich Riesemeier from Berlin synchrotron radiation facility (BESSY) for their interest in my topic and their support in performing the XAS experiments. Many thanks to my colleagues: Dr. Tobias Scherb, Dr. Stefan Mechler, Jatinkumar Rana and Jessica Kohnke for the kind assistance on the XAS experiments at the various beam times. I am especially grateful to Dr. Tobias Scherb, who gave me thousand times of helps. He is a great scientist and of course my role model.

For this research, data were essential. Thanks therefore to Dr. Markus Wollgarten and Dr. Heinz-Eberhard Mahnke who let me their EXAFS raw data measured at HASYLAB and give me a chance to reanalyse them to compare them with my own measurements. Markus Wollgarten also helped me to use TEM. Thank you.

I would like to thank Mrs Christiane Ciceron, who is a great secretary in our department and gave me a lot of help for documents management. Special thanks to Soeren Zimmerman, who was kind of my student, whose work is really valuable for my thesis.

There were many people who helped me to prepare sample and assisted me to do many in-house experiments, for which I would like to thank them: Claudia Leistner, Christiane Foerster, Holger Kropf and Harald Stapel.

I would like to thank my parents and my fiancée, who are the toughest and nicest shield to support me to go through the hardest time. I love you.

Finally, I would like to thank my country and the Chinese Scholarship Council for giving me the financial support for research.

Contents

1 Introduction

Aluminium-based amorphous alloys containing both transition metals (TM) and rare-earth elements (RE) promise excellent mechanical properties such as high strength and corrosion resistance and therefore are of practical interest [1, 2]. The high yield strength of amorphous alloys can be increased to approximately 1000 MPa by primary crystallization of fcc-Al nanocrystals embedded in a residual amorphous matrix [3]. Precipitation of fcc-Al nanocrystals can be induced by thermal treatment [3-11] or by plastic deformation [12-16], the latter., by cold rolling [17] , nanoindentation [18] , high pressure torsion [16, 19] , equal channel angular pressing [20], ball milling [15, 21] and extreme bending [12]. It is yet unclear whether the underlying mechanism for stress-induced crystallization is thermal or athermal.

This work reports structural changes of helium-atomized $Al_{85}Ni_{10}La_5$ amorphous powder during plastic deformation by ball milling at different temperatures. The structural changes are compared to those observed after thermal treatment.

In addition, the change in local atomic structure of Al-based amorphous alloys by using minor elements substitution was investigated. Al-based amorphous alloys generally reveal rather poor glass forming ability (GFA) [8]. One of the reasons for this is that their glass forming composition range lies on the Al-rich side of the eutectic point where the liquidus temperature rises steeply resulting in a strongly reduced glass transition temperature [22]. The GFA of $Al_{86}Ni_8Y_6$ has been found to be higher compared to most other Al-based amorphous alloys and it could even been improved by partial substitution of Ni by Co and of Y by La [23, 24].

Recently, by means of X-ray absorption spectroscopy (XAS) it was shown for several amorphous and quasicrystalline Zr-Ti-Ni-Cu alloys that Cu substitutes for Ni and occupies the Ni-sites in local amorphous and quasicrystalline structures [25]. This site substitution was suggested to be the reason for the improvement of GFA by element substitution. Although several XAS-studies of local order in Al-based amorphous alloys exist [26-32] there is no XAS study on site substitution on one and the same alloy up to date. Due to the similar metallic radii R of Ni (**r**(Ni) = 124.6 pm) and Co (**r**(Co) = 125.1 pm) [33] and due to the similar electronic structure of Ni and Co (both Ni and Co are 3d-elements), the $Al_{86}Ni_6Co_2Y_{4.5}La_{1.5}$ bulk metallic glass (BMG) provides an appropriate alloy system to study the effect of element substitution on local structure in one and the same alloy system. Second, the determination of the coordination number in both $Al_{5.9}Ni_{9.1}Y_{5.1}$ and $Al_{86}Ni_6Co_2Y_{4.5}La_{1.5}$ provides additional information on the cluster structure in Al-based alloys and therefore also on the optimum composition with respect to the GFA of these alloys.

Based on the model of Dense Random Packing of Hard Sphere (DRPHS), which is a common model to describe the structure of amorphous alloys, the coordination number of the absorbing atom as a function of the sum of metallic radii of absorbing atom and neighbouring atoms follows a linearly increasing trend. In another words, metallic radii were used in this model to predict the cluster structure. However, the local structures around Ni, Co and Fe disagree with the DRPHS model [28, 32, 34-36]. Therefore, to investigate the role of atomic size in the local structure arrangement, various elements with different atomic radii as a minor substitution of Ni were produced in $Al_{86}Ni_8La_6$ amorphous alloys. Local structures around those elements are investigated by XAS in this work.

This work contains a literature survey and experimental details in chapter 2 and 3, respectively. The effects of deformation on microstructure and local structure in $Al_{85}Ni_{10}La_5$ amorphous alloy are described and discussed in chapter 4. The role of element substitution on local structure in Al-TM-RE alloys is analysed and discussed in chapter 5. Chapter 6 summarizes the main results and conclusions. Chapter 7 gives an outlook for future work.

2 Literature Survey

2.1 Metallic glasses

Metallic glasses are metastable materials having no long-range atomic order [37]. They can be formed by a number of different techniques which are based on rapid solidification. The alloys in gas or liquid phases were quenched too rapidly to form crystals. The crystallization is suppressed as a result of insufficient time for nucleation and growth of crystalline phases. The atomic packing orders, therefore, stay at their liquid configuration and the shear viscosity of the melt, η, increases continuously, as shown in Figure 2.1 (a). Short-range order can be observed in most of these "frozen-in" solids, but no long-range order can be found. The temperatures T_g and T_m denote the glass transition temperature and the melting temperature, respectively. At T_g, the marked increase in specific heat, C_p, is accompanied by an abrupt and reversible decrease in viscosity, as shown in Figure 2.1(a) and (b), which corresponds to an increase of atom mobility with increasing temperature. At temperature T_x, which often is only slightly higher than T_g, the amorphous alloy starts to crystallize.

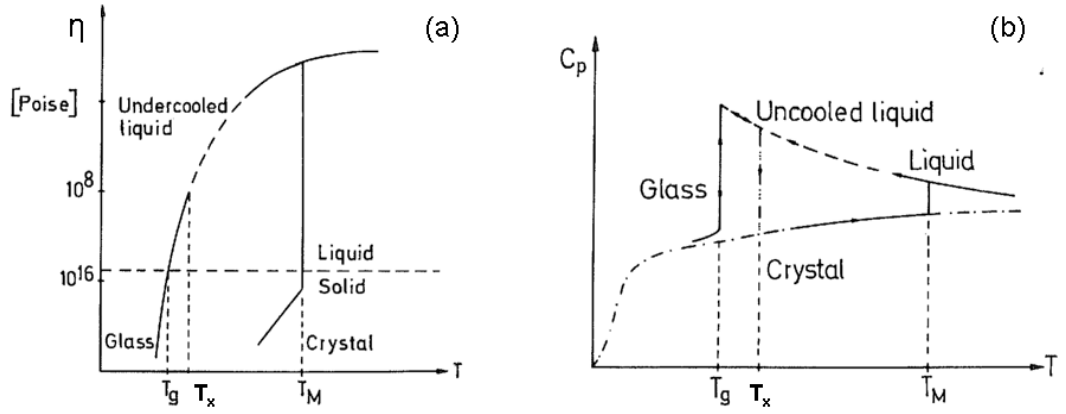

Figure 2.1: Temperature dependence of viscosity $\boldsymbol{\eta}$ *and the specific heat* C_p *corresponding to crystallization and vitrification of a metallic melt [38].*

2.1.1 Glass Forming Ability

Glass forming ability (GFA) is used to describe the glass formation from a kinetic point of view. This means that metallic glasses obtained by quenching from the liquid require a fast cooling rate below $\boldsymbol{T_g}$. As the speed of solidification becomes higher, the nucleation and growth associated with equilibrium phase formation can be constrained resulting in an increase of alloy metastability. The evolution of a phase diagram from stable to metastable equilibrium is shown in Figure 2.2. Slowing down of kinetics results in metastable equilibrium condition, where the crystallization bypasses the formation of equilibrium γ phase (see Figure 2.2 (a)) to yield a metastable eutectic phase diagram between α and β phase (see Figure 2.2(b)). Increasing the cooling rate to an extreme situation, the liquidus and solidus boundaries collapse to the $\boldsymbol{T_0}$ curves (Figure 2.2(b)). These curves reflect the limitation of partitionless transformation by a thermodynamic suppression [39]. If the α and β phase are isomorphous, the $\boldsymbol{T_0}$ curve is successive with composition (Figure 2.2(c)), while if the α and β phase have different structures, the $\boldsymbol{T_0}$ curves may not continuous (Figure 2.2(d)). In the latter case, crystallization is avoided, thus glass formation is favored in the composition range where the $\boldsymbol{T_g}$ curve is higher than the $\boldsymbol{T_0}$ curves.

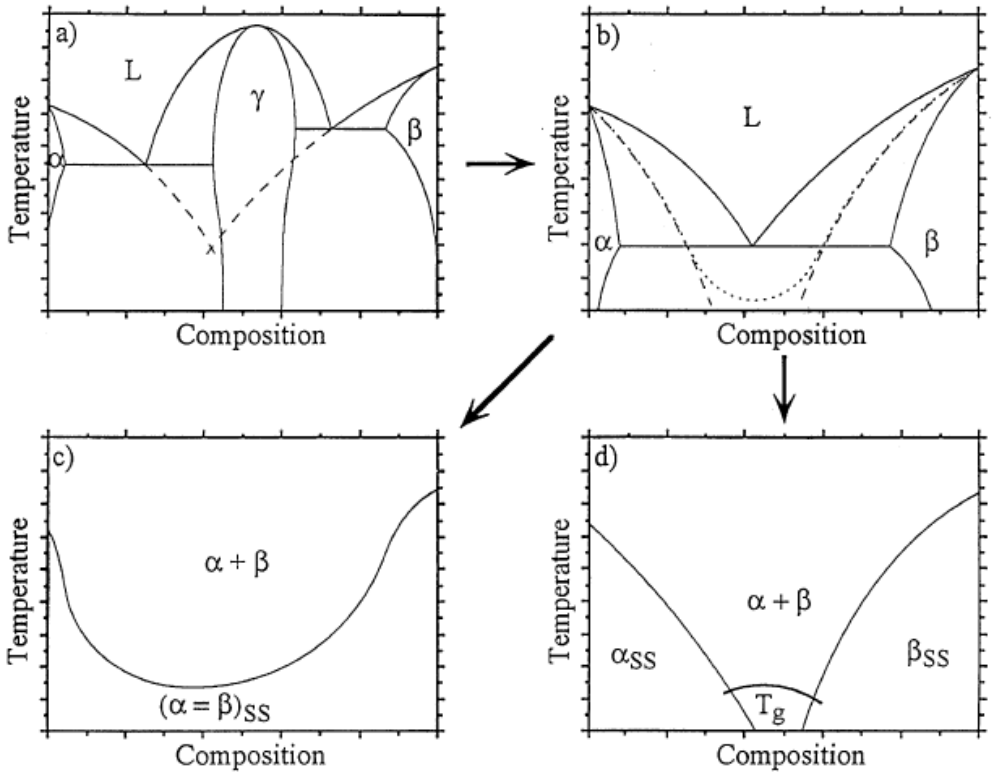

Figure 2.2: Schematic illustration of the evolution of stable to metastable equilibrium[40]. The common equilibrium phase diagram of a system is given in (a) The metastable extensions of the liquidus and solidus curves for the primary solution phases shown as dashed lines (b) shows the phase diagram of metastable equilibrium conditions, which can yield a metastable eutectic phase diagram between α and β. The T_0 curves for the primary solutions shown as dashed line are included in (b). If the α and β phases are isostructural, a metastable solid solution can develop throughout the entire composition range as in (c). If the primary phases have different crystal structures, then the T_0 curves might not intersect. In this case, the glass formation is fevered in the composition range where the T_g curve is higher than the T_0 curves in (d).

The first report for the synthesis of metallic glasses in an Au-Si system formed by rapid quenching was presented by Klement et al. in 1960 [41]. However, the maximum thickness of amorphous alloys is limited to below 100 μm due to the requirement of critical rate of about 10^6 K/s by means of melt spinning. Over the years, it was found that a great number of new glass forming liquids can yield bulk metallic glasses (BMG) which are multicomponent eutectic or close to eutectic alloys. Amorphous alloys with much higher glass forming ability require a very low critical cooling rate ranging from 10 K/s to1 K/s yielding in critical specimen dimensions of a few cm. These alloys have been found in a number of alloy systems based on

Ln [42, 43], Mg [44, 45], Zr [46, 47], Ti [48, 49], Pd [50, 51] and Fe [52, 53] (Ln = lanthanide metal). Consequently, Al based alloys with high glass forming ability as inexpensive materials became a popular topic.

Three empirical principles to predict a good GFA were given by Inoue [54, 55]:

1. Use three or more elements.
2. The difference of atomic size should be larger than 12%
3. Negative heat of mixing between solute and solvent atoms is required

The rules 1 and 2 correspond to the composition criterion to predict the composition limit for glass formation in binary (A-B) system, which is given as:

$$c_B^{\min} = 0.1\frac{V}{|\Delta V|} \tag{2.1}$$

Where $c_B^{\min}$ is the minimum concentration of the B element as a solute in the A matrix to form a glass, V is the average atomic volume of A and B elements, and $\Delta V = V_A - V_B$. This represents the requirement of destabilizing the solid solution to form a glass.

Rule 3 can be understood as a competition between two attractive forces. One is the attractive force between solvent atoms causing crystallization of these atoms; another one is the attractive force between solute elements and solvent elements. When the mixing enthalpy is negative and relatively large, the attractive force for crystallization of solvent atoms can be offset. The mobility of solvent atoms becomes relatively low which enhances the GFA during solidification.

Furthermore, another tool to describe GFA was given by Turnbull [56]. He described the reduced glass transition temperature $\boldsymbol{T_{rg}}$ by the ratio of $\boldsymbol{T_g/T_m}$. Good GFA can be expected, if $\boldsymbol{T_{rg}}$ is larger than 2/3.

2.1.2 Al-based Bulk Metallic Glasses

It is very difficult to form an Al-based bulk amorphous alloy by the use of the direct solidification method, because the glass forming range is far away from the eutectic point where the

liquidus temperature rises steeply resulting in a strongly reduced glass transition temperature. Al-transition metal (TM) - rare earth (RE) type amorphous alloy which exhibit an excellent strength and ductility was first produced in 1988 [1, 57]. Nitsche mentioned that in Al-TM-RE amorphous alloys , the hetero-coordination pairs of Al-RE, Al-TM and RE-TM occur preferentially in the as-quenched state [58], as exemplified schematically in Figure 2.3 (a). Homo-coordinated TM-TM or RE-RE pairs are ignorable. The probability of Al bonds to TM-atoms or RE-atoms increases with adding more solute. If the solute content decreases, homo-coordinated bonding of Al-Al is obtained as precursors for Al nanocrystals. To pursue the Al-based bulk amorphous alloy with high glass forming ability, a cluster line model based on the hetero-coordination pairs was used to predict the alloy composition with good GFA, as shown in Figure 2.3 (b). For $Al_{86}Ni_6Co_2Y_{4.5}La_{1.5}$ as an Al-based bulk amorphous alloy, the diameter can reach up to 1 mm which is the biggest thickness known for Al-based glasses [24].

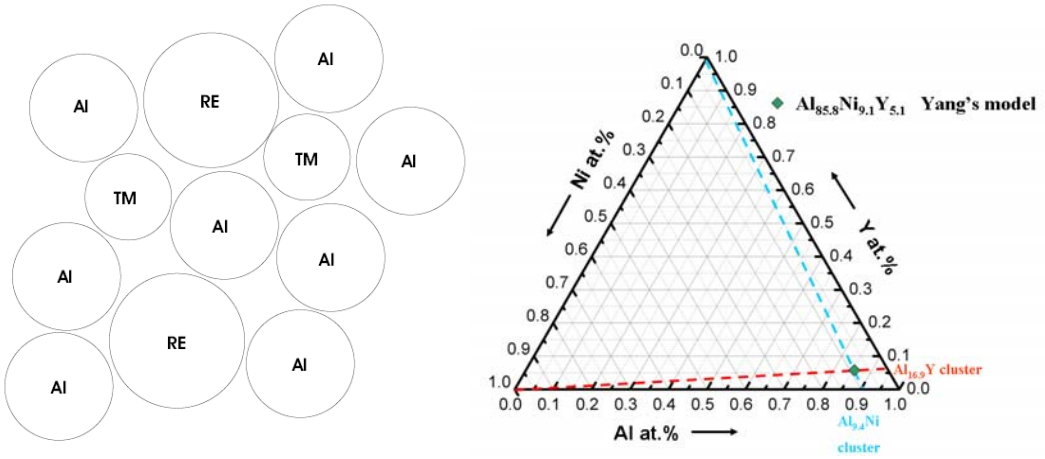

(a) (b)

Figure 2.3: (a) Schematical graph of chemical short-range order of amorphous Al-TM-RE amorphous alloys in the as-quenched state[58]. (b) An illustration of Yang's composition design. The two dashed lines denote the cluster stability line used by Yang et al. [23, 24]. The cubic symbol at the intersection of two dashed lines is the favourable composition predicted in Yang's work.

2.2 Topological Models for the Atomic Structure

To describe the amorphous structure in metallic glasses, many models were created. Four models (Free volume conception, dense random packing of hard sphere model, Miracle's model and atomic configuration for Al-based metallic glasses by ab-initio calculation) used in this work are introduced in detail. There are many other models such as Oliveira's model [59] and Fang's model [60] etc. which are not used in this work. They are, therefore not discussed here.

2.2.1 Free Volume

The conception of free volume for metallic liquids was quantified by Cohen and Turnbull [61, 62]. The conception was started with the recognition that the viscosity of a liquid highly correlates to its volume. Different from a gas, a liquid is a densely packed matter in which an atom is trapped in the "cage" constituted by the neighbouring atoms. Most of the time, an atom that is fixed in the "cage" cannot move to another place. Only if it gets enough space, larger than a critical volume v^*, next to the atom, the atom can jump into this space, see Figure 2.4.

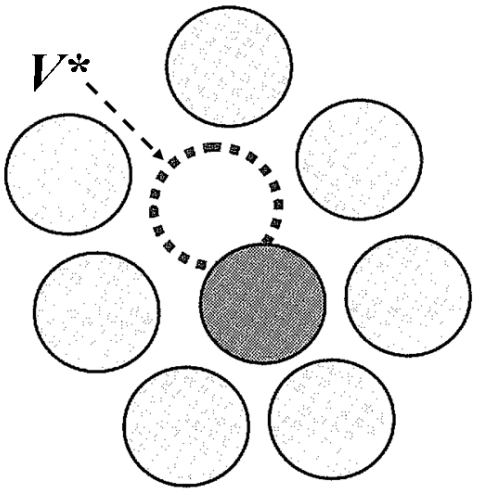

Figure 2.4: Schematic representation of free volume for an atom to move into [63]. v^* is marked in the figure.

The diffusivity is given by [63]

$$D = D(v^*)\int_{v^*}^{\infty} p(v)dv = D(v^*)\exp\left(-\frac{\gamma v^*}{v_f}\right) \tag{2.2}$$

where $p(v)$ is the probability distribution of space between atoms, γ is a constant of order of unity and v_f is the total free volume.

The lattice structure remains the same in a crystal while the volume expands only due to the vibration of atoms during heating if there is no phase transformation. By contrast, the structure and volume of a glass show significant temperature dependence. From below $\boldsymbol{T_g}$ to above $\boldsymbol{T_g}$, the slope of volume as a function of temperature becomes steeper, which reflects that above $\boldsymbol{T_g}$ the changes in the structure with temperature change occur quickly below $\boldsymbol{T_g}$, however, the kinetics of changes slows down. Annealing the metallic glass below $\boldsymbol{T_g}$, causes the structure to slowly relax from an energetically higher metastable state towards an energetically lower metastable state [64] with a decrease of free volume and correlated changes in topological and chemical short-range order (SRO).

The free volume theory was also used to describe plastic flow during deformation [65, 66]. Free volume cannot induce shear deformation by itself, although atoms could move because of diffusion. The basic conception is that shear bands need free space on the atomic scale to propagate. Therefore, the free volume controls shear flow. Furthermore, plastic deformation induces free volume in the shear bands [67].

2.2.2 Dense Random Packing and Bernal's Model

Bernal proposed that the atomic arrangement of a simple liquid is determined by volume exclusion [68]. Because the density of a liquid is only a few percent lower than the crystal density, the coordination number in a simple liquid must be high. The experimental value (in a pure liquid) is around 8-12. Furthermore, he created a model in which the atoms were considered as hard spheres, and their atomic structure was determined based on the dense random packing which is restricted by the principle that two atoms cannot come closer than

one atomic diameter. There are only five different types of clusters defined by nearest neighbors, as shown in Figure 2.5, constituted by equal triangular faces which are the smallest unit.

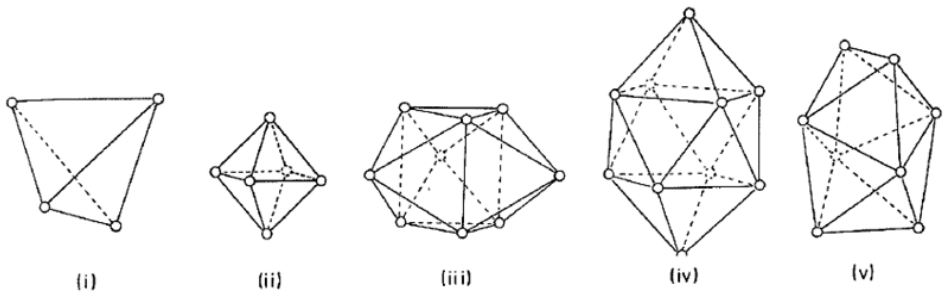

Figure 2.5: Polyhedra formed by packing equal spheres. (i) tetrahedron, (ii) octahedron, (iii) trigonal prisms "capped" with tree half octahedra, (iv) Archimedean antiprisms capped with two-half octahedra, (v) tetragonal dodecahedron [69].

Using these five polyhedra with almost equal nearest neighbour distance, a large number of structures can be formed. Bernal showed that it is possible to pack them together in 197 different ways. The relative statistic in these polyhedra shows a preference proportion of tetrahedra and half octahetra, which are 48% and 27% respectively. The larger clusters with smaller proportion (8% for trigonal prisms, 2% for Archimedean antiprisms and 15% for tetragonal dodecahedra) are enfolded around by a network of the tetrahedra and half octahetra.

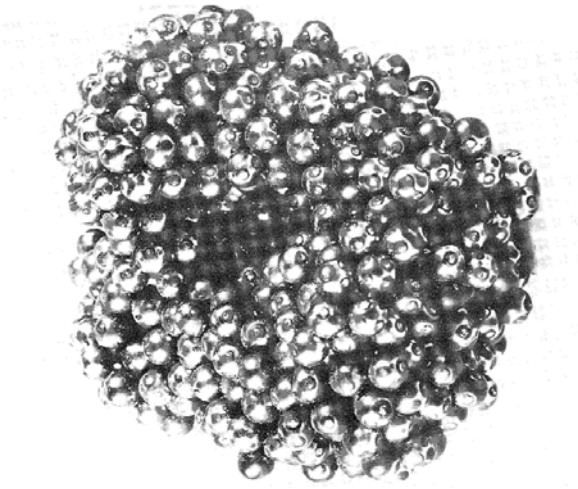

Figure 2.6: A laboratory-constructed random close packing of hard-spheres shows no lattice ordering [37].

The random close packing model structure is illustrated in Figure 2.6. It is obvious that the structure reveals no crystallinity. Although it is simple, this model demonstrated many of the structure features of simple liquids, and provided excellent explanation of supercooling, nucleation, melting, fluidity and diffusion. The random close packing model was further developed by Finney [70] who made a large model with 7994 atoms with a packing density of $\eta_f = 0.6366 \pm 0.0004$.

2.2.3 Miracle's Model

Miracle reported an atomic structure model for metallic glasses which is based on a conception of dense packing of atomic clusters [71-73]. The primary atomic cluster is constituted by the largest, primary solute atom α wrapped by the solvent atoms Ω. The preferred size of primary clusters is determined by using the discrete solute to solvent radius ratio R_d which satisfies an efficient solute centred packing in the local cluster. The cluster ordering provides two additional topological species, which is a secondary solute β sitting in an octahedral cavity and a tertiary solute γ sitting in a tetrahedral interstice. This means that only three topologically distinct solutes are contained in a metallic glass, as shown in Figure 2.7. All solutes satisfying the ratio R_d (solute radius/solvent radius) can be efficiently packed in the first coordination shell. Hence, only in the first coordination shell, the clusters are densely packed to form a structure of overlapping clusters. If the difference of atomic radius between two solutes is within ±2%, these two solutes can be considered as topologically equivalent. This model presents not only the short-range order, medium-range atomic order up to ~1 nm can also be explained.

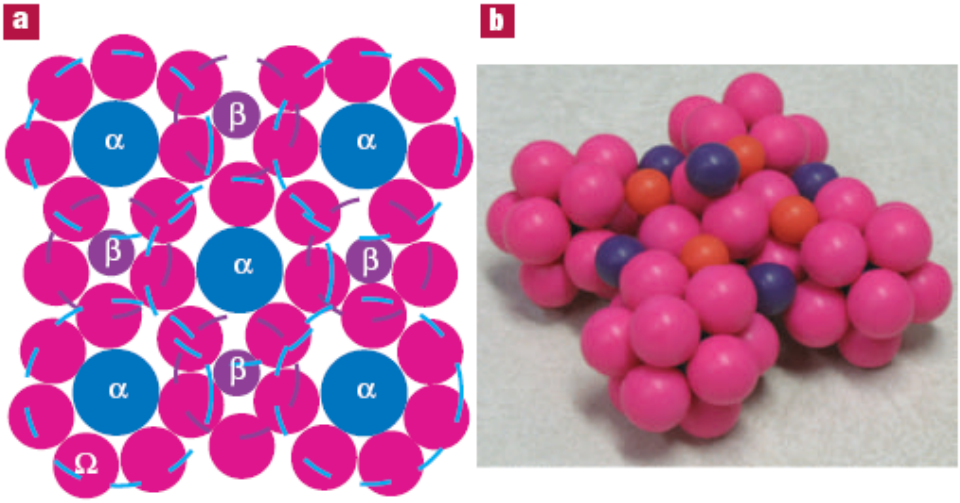

*Figure 2.7: Schematical graph of a dense cluster packing model. (a) A two dimensional illustration of a dense cluster packing structure in (100) plane. (b) A laboratory-constructed model for a Zr-(Al, Ti)-(Cu, Ni)-Be alloy. Blue spheres represent **α**-sites, purple spheres stand for **β**-sites, orange spheres represent **γ**-sites, pink spheres as solvent Zr atoms. No orientational order in icosahedral cluster is observed [71].*

2.2.4 Atomic Configuration in Al-based Metallic Glasses

Three-dimensional model of atomic arrangement for Al-based metallic glasses going far beyond hard-sphere models was reported by Sheng et al. [74]. Ab-initio molecular dynamics simulation using inverse Monte Carlo (IMC) method was performed to obtain information about solute-centred atomic clusters.

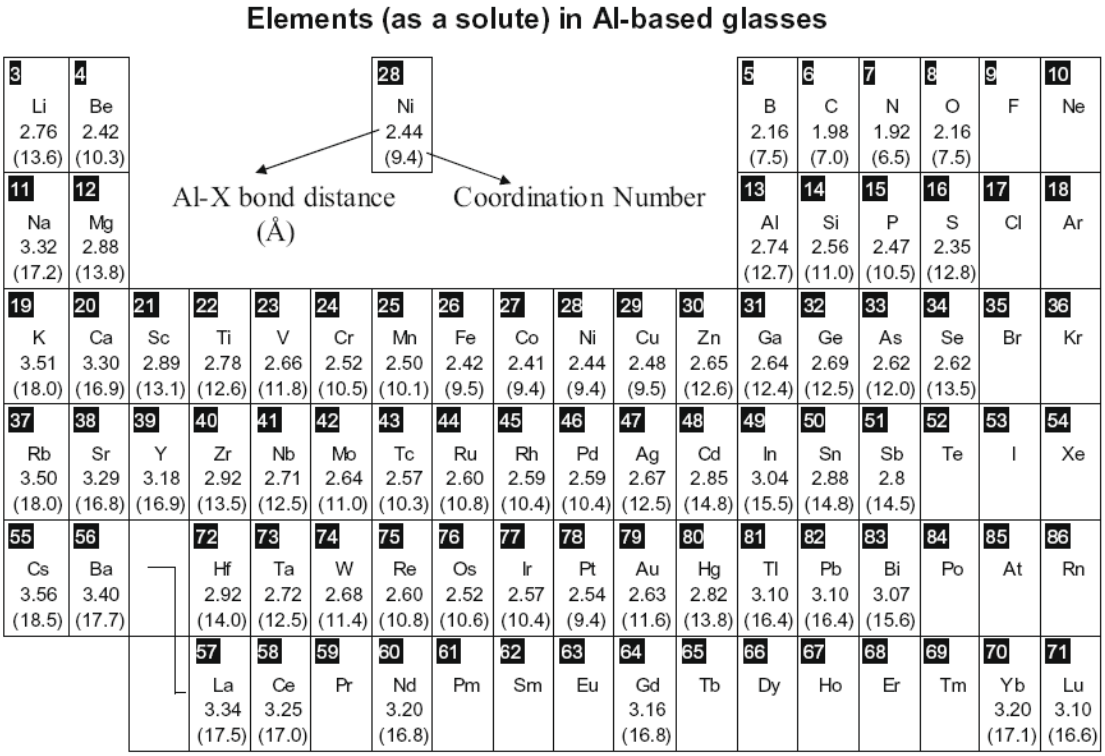

Figure 2.8: Bond length (Al-solute element) and coordination number of Al atoms around solute elements in Al-based metallic glasses determined by ab-initio calculations [74].

Al-solute bond distance in Al-based metallic glasses derived from ab-initio calculation according to Sheng et al. [74] is shown in Figure 2.8. The coordination numbers in solute-centred clusters are also included. Yang et al. used this cluster model to predict the favourable composition as $Al_{85.8}TM_{9.1}RE_{5.1}$ [23, 24].

2.3 Stability of Metallic Glasses

Metallic glasses as metastable materials have relatively sensitive thermal properties because they are far from thermodynamic equilibrium. Devitrification can occur during annealing [19, 75] or plastic deformation [15, 16]. It gives an opportunity to produce a new class of materials with nanocrystals embedded in the amorphous matrix. Nanocrystalline materials show a wide range of unique mechanical properties, for example, high toughness, long fatigue life and

good wear resistance [76, 77]. Nanocrystals can be produced by many methods in Al based amorphous alloys [2, 40]. The common methods are basically classified as:

1. Nuclei induced during rapid quenching of a liquid.
2. Primary crystallization by annealing of amorphous matrix.
3. Nanocrystals induced by plastic deformation.
4. Mechanical alloying of crystalline powders.

Method 1 and 2 is based on the thermal treatment, and methods 3 and 4 mechanical processes.

2.3.1 Alloy Stability during Thermal Treatment

The time range of metallic glass formation is an important parameter for the vitrification and devitrification because of the limitation of the nucleation and growth kinetics. One approach to describe the kinetic restraint is represented by time-temperature-transformation (TTT) diagrams, as shown in Figure 2.9. The "nose" shape is due to the competition of increasing driving force for crystallization with decreasing atomic mobility [78]. Three different path ways were applied to describe glass formation and partially crystallization. The quenching process follows path 1 with a high cooling rate which restricts nucleation and bypasses crystallization to successively form an amorphous phase. The difference between path 1 and 2 is the different cooling rate. Path 2 has a lower quenching speed, and crosses over the crystalline-supercooled liquid boundary curve, where the driving force for nucleation and grain growth is sufficient for crystallization. Therefore, crystals in the supercooled liquid start to precipitate. However, as soon as path 2 runs out of the "crystalline range" grain growth is restricted and final nanocrystals are obtained. Furthermore, another approach to produce nanocrystalline materials carries out with path 3. Annealing the amorphous alloy to a certain temperature, primary crystallization occurs. Grain growth is highly dependent on the temperature and annealing time.

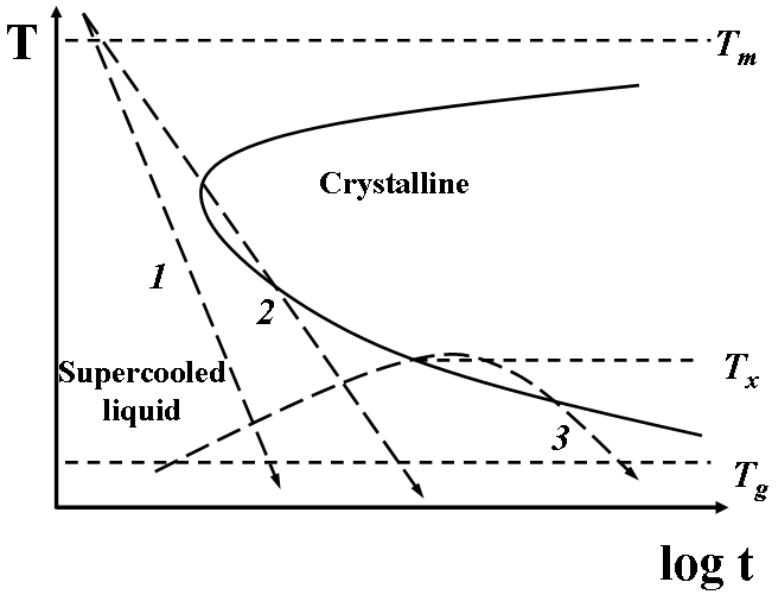

Figure 2.9: Time-temperature-transformation diagram to explain three path ways to gain glassy or crystalline phase.

Crystallization behavior also highly depends on the alloy composition. Three categories can be generally classified:

1. Polymorphous crystallization: a crystal with the same composition as the glass matrix grows, requiring no long-range diffusion.
2. Eutectic crystallization: two crystalline phases grow at the same time and the total composition of these two phases remains the same as that of the glassy matrix. Therefore, no long range diffusion is required
3. Primary crystallization: A primary crystalline phase with a different composition precipitates in the glassy matrix. Solute atoms diffuse out of the crystal and create a solute rich shell around the crystal. This shell can limit the crystallite size. Due to this phenomenon, primary crystallization became the favor reaction to produce nano-crystals in amorphous materials.

2.3.2 Stability during Plastic Deformation

The deformation mechanism of metallic glasses is different from crystalline metals and alloys because metallic glasses do not show long-range translational symmetry. In crystalline metals

and alloys, dislocations permit the structure changes by the requirement of a low energy or low stress. Metallic glasses have no dislocations. This results in the requirement of a higher energy and higher stress when rearranging the atoms in the amorphous matrix.

A two-dimensional schematic model according to Schuh et al. [79] is shown in Figure 2.10. A "shear transformation zone" (STZ) as an important structural unit was originally introduced by Argon [80], see Figure 2.10 (a). STZ exhibits a local cluster of atoms deformed from a state with relatively low energy to a second position of higher energy under a shear force. The local free volume distribution is shown schematically in Figure 2.10 (b). Metallic glasses with higher free volume would be easier deformed by a local shear force.

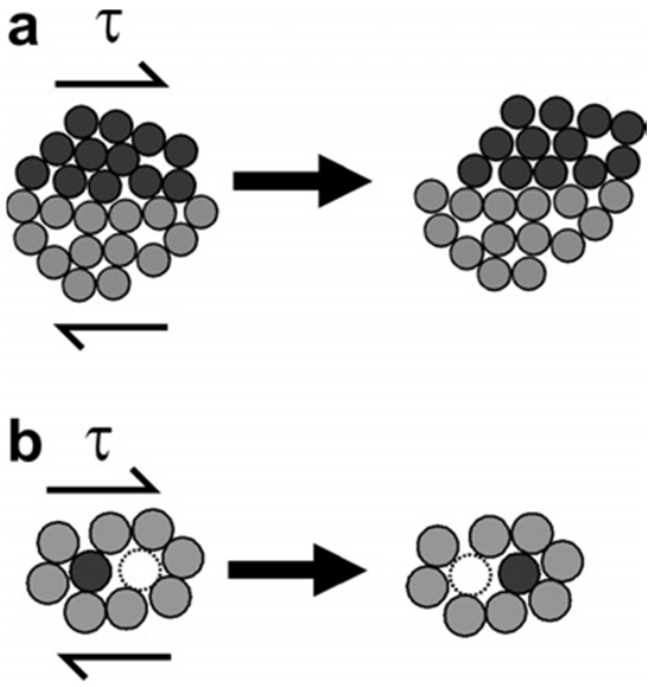

Figure 2.10: Schematical diagram of two dimensional atomic rearrangement during deformation [79], including (a) shear transformation zone, and (b) a local atomic jump

Several articles reported the precipitation of nanocrystals inside shear bands induced by plastic deformation. Deformation was performed by bent ribbon [12, 14, 81], nanoindentation [18, 82], microhardness [83], ball milling [13, 15] and cold rolling [17].

The mechanism by which crystallization occurs during deformation is still not fully understood. One possible explanation is the localized heating in the shear bands. This view point is supported by the direct observation of a drastic rise of temperature in the shear bands [84]. However, an opposite view was represented, namely that the localized heating is not sufficient for crystallization [85]. This conception is supported by the observation that in bent ribbon, nanocrystals only can be observed in the shear band in compressive areas but not in tensile strained areas. Both deformed areas had the same strain rate and associated heating which indicated that the type of deformation (sign of strain) plays an important role in crystallization.

Chen et al. suggested that deformation-induced crystallization is the result of the destruction of short-range order by shear forces, but not of the heating in shear bands [12]. Consequently, many other works present a similar view that the dominant reason for crystallization during plastic deformation is an increase in atomic mobility [86, 87] related to an increase in free volume.

In addition, there is another possibility that plastic deformation could change thermodynamics of metallic glasses, not only kinetics [85]. Short-range chemical ordering and phase separation caused by deformation may dramatically reduce the activation energy of crystallization [88].

3 Experimental

Information on the μm and below scale was obtained by a scanning electron microscopy (SEM). Grain sizes of the powders were compared after different milling treatments with regard to ball milling time and temperature. Additionally, the surface structures of the powder particles were analysed in detail.

An X-ray diffractometer with monochromatic X-rays enables the identification of crystal structures and lattic parameters. It also allows to roughly determine the particle size of the resulting crystals.

Differential scanning calorimetry was used in this work to obtain accurate information regarding the glass transition and crystallization temperatures at specific heating rates. By varying the heating rate and using the Kissinger method, the activation energy of phase transitions was calculated.

Transmission Electron Microscopy (TEM) was used to study fine microstructures, especially for verifying the amorphous nature of a sample and analyzing the crystallized precipitates embedded in a metallic glass matrix.

We used X-ray-absorption spectroscopy (XAS) as a method to probe the local atomic environment. The advantage of XAS over many other techniques is its ability to select a specific element as a central atom and to study the radial distribution of its nearest neighbours.

All methods and the equipment used in this work are presented and explained below in more detail.

3.1 Materials

In this work, Al-transition metal (TM)-rare earth (RE) ternary system was chosen for its glass forming ability that is higher compared to other known Al-rich metallic glasses [1, 89]. Inoue's empirical composition graph for ductile metallic glasses is shown in Figure 3.1.

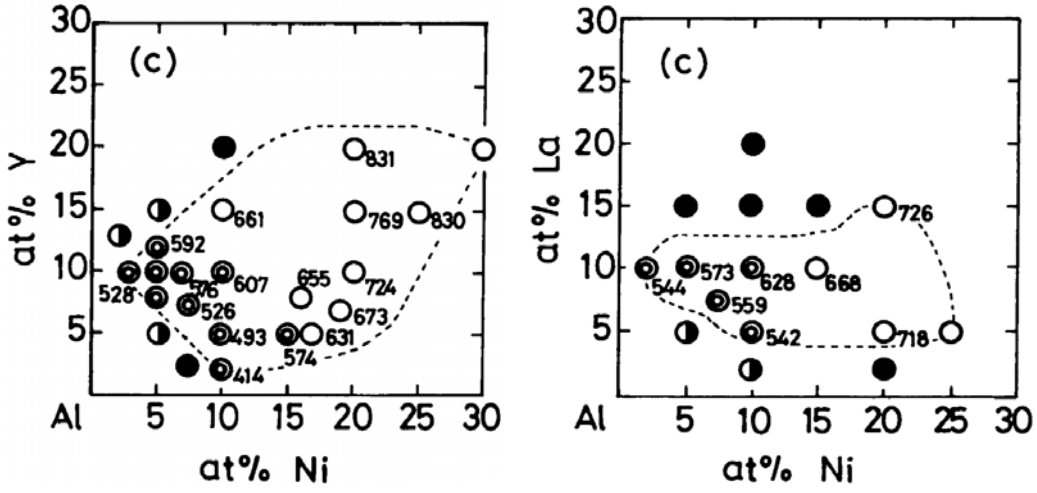

Figure 3.1: Compositional range for formation of amorphous phase and the difference of crystallization temperatures in Al-Ni-Y (left), Al-Ni-La (right) systems: (◎) amorphous (ductile); (○) amorphous (brittle); (◑) amorphous plus crystalline; (●) crystalline. [89]

These two figures indicate that both $Al_{85}Ni_{10}La_5$ and $Al_{86}Ni_8Y_6$ used in this work can be produced as ductile amorphous alloys. The amorphous $Al_{85}Ni_{10}La_5$ powder was produced by gas-atomization, while the $Al_{86}Ni_8Y_6$ alloy was produced by splat quenching. This alloy was used as a reference to investigate the substitution of 1 at% Ni by Ag ($Ag_1Al_{86}Ni_7Y_6$), Zr ($Zr_1Al_{86}Ni_7Y_6$), Hf ($Hf_1Al_{86}Ni_7Y_6$), Ge ($Ge_1Al_{86}Ni_7Y_6$), or Pd ($Pd_1Al_{86}Ni_7Y_6$), and substitution of Ni by Co and Y by La ($Al_{86}Ni_6Co_2Y_{4.5}La_{1.5}$). For investigating Ag-Ni and Zr-Ni substitution, we also used the compositions $Ag_1Al_{87}Ni_5La_7$ and $Zr_1Al_{87}Ni_5La_7$.

3.2 Splat Quenching

Preparation of metallic glasses requires rapid quenching. Splat quenching can quench a droplet of a molten metal by roughly 1000 K in one millisecond, producing splats typical 50 μm thick. The ingots with a nominal composition of $Al_{86}Ni_6Co_2Y_{4.5}La_{1.5}$, $Al_{86}Ni_8Y_6$, $Ag_1Al_{86}Ni_7Y_6$, $Ge_1Al_{86}Ni_7Y_6$, $Zr_1Al_{86}Ni_7Y_6$, $Pd_1Al_{86}Ni_7Y_6$ and $Hf_1Al_{86}Ni_7Y_6$ were produced by alloying pure elements Al (99.98%), Ni (99.7%), La (99.7%), Y (99.7%), Ag (99.7%), Zr (99.7%), Pd (99.7%), and Hf (99.7%) using a high frequency electromagnetic levitation furnace. Oxidation during induction melting was minimized by working under a purified argon atmosphere. The liquid alloy was levitated at high temperature for 2 to 7 min to remove the oxidation surface and then fell down into a water cooled copper crucible where it formed a crystalline ingot. This course of solidification was repeated several times after turning the ingot upside down to homogenize the master alloy. After that, the ingot was cut into cubes of approximately 2×2×2 mm^3. Splats of $Al_{86}Ni_6Co_2Y_{4.5}La_{1.5}$, $Al_{86}Ni_8Y_6$, $Ag_1Al_{86}Ni_7Y_6$, $Ge_1Al_{86}Ni_7Y_6$, $Zr_1Al_{86}Ni_7Y_6$, $Pd_1Al_{86}Ni_7Y_6$ and $Hf_1Al_{86}Ni_7Y_6$ amorphous alloys were produced by rapid solidification in a Buehler G.m.b.H. twin piston splat quencher at ~ 10^{-5} mbar. The thickness of the splats ranged from 35 to 45 μm.

3.3 Ball Milling

Plastic deformation of as-atomized $Al_{85}Ni_{10}La_5$ powder was performed by ball milling using the Spex Mixer Mill 8000 shown in Figure 3.2 (a). The movement of the mill is cyclical with a frequency of 1020 per minute. Powder container and balls is shown in Figure 3.2(b). The set includes a solid zirconia ceramic grinding vial, a slip-on cap and two zirconia ceramic balls with a diameter of 12.7 mm, which ensure very low abrasion during grinding. The grinding vial is 5.8 cm in diameter and 6.8 cm long; the inner diameter and inner length are both 4cm. The mass of the two balls is 6.2 g each. The mass of as-atomized $Al_{85}Ni_{10}La_5$ powder in the mill is 6.2 g, thereby the charge ratio is 2:1. Before starting milling, the amorphous powder is into the grinding bowl together with the two balls. The bowl is then flushed with argon and hermetically sealed in order to prevent oxidation. Seven ball milling times (60 min, 120 min, 240 min, 480 min, 600 min, 1200 min, and 6000 min) were applied. We denote these batches

of powder as BM 60, BM 120, BM 240, BM 480, BM 600, and BM 1200. Ball milling performed every 15 min and stopped for 45 min to cool down to ambient temperature. After each grinding process the grinding vial and the balls were cleaned by concentrated sodium hydroxide solution.

(a) (b)

Figure 3.2: Spex Mixer Mill 8000 and (a) zirconia ceramic grinding vial and (b) two balls

Ball milling was performed at four different temperature ranges (-80°C < T < -50°C, "low temperature", LT; "room temperature", RT; 50°C < T < 60°C, "intermediate temperature", IT; 80°C < T < 100°C, "high temperature", HT). Ball milling performed in temperature ranges beyond room temperature (LT, IT or HT) needs cooling or heating. Solid carbon dioxide (dry ice) was used as a cooling agent to supply a low temperature atmosphere and not leaving any residue. At atmospheric pressure, CO_2 sublimates at −78.5 °C with no transient liquidus state form. Around the zirconia ceramic grinding vial we made a box of chloroprene rubber (neoprene) to fill dry ice as shown in Figure 3.3. A thermocouple was pasted to the outer skin of the zirconia container. Heat conduction from the outer to the inner skin of the grinding vial was found to be faster than 10 s. Therefore, the temperature measured after outer skin can be roughly estimated as the temperature of the sample during ball milling.

(a) (b)

Figure 3.3: chloroprene rubber box before fell dry ice (a) and after (b)

3.4 Optical Microscope

Optical Microscopy (Zeiss, Axioplan 2 and Axiophot 2) were used for a first rough characterization of powder particles including an estimate of particle size. Images of as-atomized powders and powders after ball milling for 60, 120, 240, 600, 1200 and 6000 min were recorded.

3.5 Scanning Electron Microscope

Scanning electron microscopy (SEM) was done using either a Philips XL30 ESEM or a Zeiss CrossBeam 1540ESB. Electrons are released from a field emission cathode by an applied acceleration voltage (5-20 kV). A condenser and objective lens system is used for focusing the beam of high-energy electrons and to generate a variety of signals at the surface of solid specimens. The signals that derive from electron-sample interactions reveal information about the sample including external morphology (texture), chemical composition and crystal parameters and orientation of materials making up the sample. These signals include secondary electrons, backscattered electrons (BSE), diffracted backscattered electrons, photons, visible light, and heat. Secondary electrons and backscattered electrons are commonly used for imaging samples: secondary electrons are most useful for showing the morphology and topography

of samples and backscattered electrons are most valuable for illustrating contrasts in composition in multiphase samples. X-rays are produced by inelastic collisions of the incident electrons with electrons in discrete shells of atoms in the sample. As excited electrons return to lower energy states they yield characteristic X-rays.

3.6 X-ray Diffractometry

X-ray diffraction (XRD) was used as a tool to identify and analyse amorphous and crystalline phases. The measurement is based on the elastic diffraction of X-rays by the electron shells of atoms. An incident monochromic beam diffracted by a crystalline sample resulting in discrete sharp maximum peaks at certain angles θ when they satisfy the condition of Bragg's law referring constructive interference. In the following, discrete maximum intensities of the diffracted beam are named either Bragg reflections or Bragg peaks. The glancing angles θ following a relationship between the wavelength λ of the incident X-rays, an integer denotes the order of the scattering maximum n, the lattice spacing d_{hkl} and follow Bragg's formula:

$$n\lambda = 2d_{hkl}\sin\theta \qquad 3.1$$

The geometry of an X-ray diffractometer is shown in Figure 3.4. The sample set in the path of the collimated X-ray beam at an angle θ while the X-ray detector is mounted on an arm to collect diffracted X-rays at an angle of 2θ. The instrument used to control the angle and rotate the sample is termed a goniometer. XRD patterns consist of several components related to the X-ray spectrum, the most common being K_α and K_β. K_α consists, in part, of $K_{\alpha1}$ and $K_{\alpha2}$. $K_{\alpha1}$ has a slightly shorter wavelength and twice the intensity as $K_{\alpha2}$. For Cu K_α radiation, Ni foil was performed as a filter to avoid K_β peak intensity.

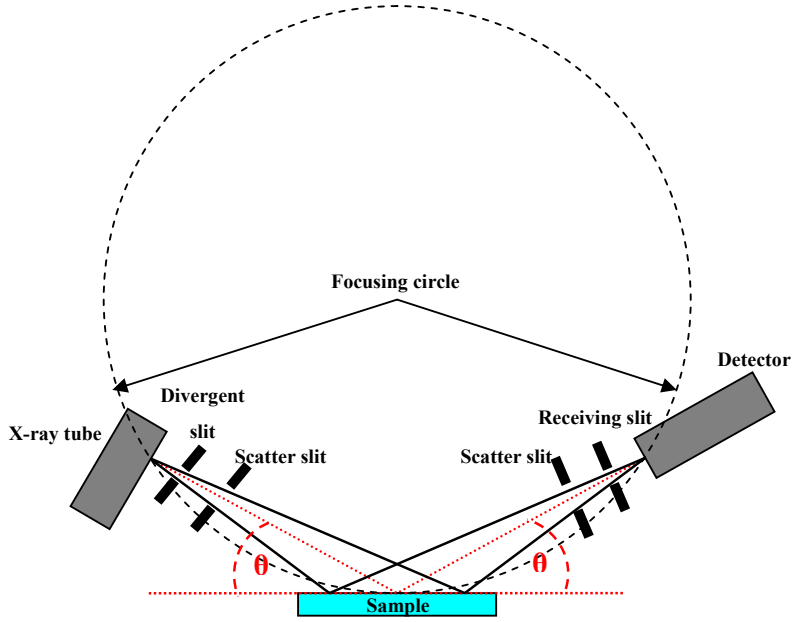

Figure 3.4: Geometry of an X-ray diffractometer

Unlike diffraction from in a single crystal, in the powder (Debye-Scherrer) method, the X-rays fall on a variety of tiny crystals aligned in many different orientations and the diffracted beams of all of the Bragg reflections of randomly oriented crystallites form a cone. Peak position of the XRD pattern of specimens can be analyzed by searching for matches with PDF-data of the International Center for Diffraction Data (ICDD).

We can determine crystallite sizes by employing Scherrer's Formula [90, 91] which is associated with a broadening of Bragg reflections. The relationship between full-width-at-half-maximum D and crystallite size M is shown below[90]:

$$M = \frac{0.9\lambda}{D \cdot \cos\theta}, \qquad 3.2$$

where λ is the wavelength of the X-ray, θ is a Bragg angle.

Metallic glasses have only short-range order not a long-range order, which means that only the occupancy of the nearest neighbours of a random atom is correlated. The correlations of an atom to its neighbours decrease with increasing radius to second and further neighbour

shells. The scattered intensity, therefore, does not show discrete Bragg peak as in crystalline materials but a broad diffuse scattering maximum or an amorphous halo. Partial crystallization yields a combined condition of the broad diffuse scattering and discrete Bragg reflections. After heat treatment, the complete crystallization shows Bragg reflections only.

In our experiment, a Brucker D8 Advance diffractometer was used, which contained a Bragg-Brentano geometry, Cu K_α radiation (λ = 0.15406nm), a secondary graphite monochromator and a scintillation counter detector. The Bragg angle 2θ range was set from 10° to 100°, in steps of 0.02° with a scattering time of 10 s per step. Scattering slits of 0.2 mm were used for both incident and diffracted beams.

3.7 Differential Scanning Calorimetry

In this work, phase transformations upon continuous heating of amorphous specimens were investigated by using differential scanning calorimetry (DSC). The measurements were performed by using a Perkin-Elmer DSC Pyris 1 with a flowing argon atmosphere. The signal obtained from the difference in the amount of heat required during increasing the temperature of a sample and reference is recorded as a function of temperature, while both the sample and reference are maintained at nearly the same temperature throughout the experiment. Due to the slight difference of the thermal properties between the specimen furnace and reference furnace, a base line has to be recorded before an experiment to compensate for drifts. Some error was induced by impurities on the holders and furnaces, therefore, one hour of isothermal heating at 600°C is necessary to counteract the reactions of impurities. The calibration of the calorimeter was down by using pure In and Zn. The accuracy of temperature and specific energy of melt is about ±0.3°C and ±0.02mW, respectively.

Continuous heating experiments were carried out in seven steps. (1) isothermal at 50°C for 15min; (2) continuous heating with a certain heating rate (from 5 to 80°C/min) to 600°C at which the specimen completely crystallized; (3) keep the temperature at 600°C for 5min; (4) cooling down to 50°C with the cooling rate of 60°C/min; (5) continuous heating to 600°C

with a same heating rate as process 2; (6) constant 600°C for 5min; and (7) cooling down to 50°C with the cooling rate of 60°C/min. The DSC curve used in this work obtained by using the signal of heating of process 2 subtract of process 5. Continuous heating at 20°C/min of all specimen repeated 3 times to get the qualitatively identical curves. Peak maximum T_p, onset temperature of glass transition T_g, crystallization temperature T_x and peak areas were extracted from DSC curves. In addition, activation energies of phase transformations were determined by applying Kissinger analysis [92-94]:

$$\frac{d\left(\ln\frac{\Phi}{T^2}\right)}{d\left(\frac{1}{T}\right)} = -\frac{E}{R_{gas}}, \tag{3.3}$$

where $\boldsymbol{\Phi}$ is the heating rate, $\boldsymbol{T}$ can be $\boldsymbol{T_p}$.$\boldsymbol{T_g}$ or $\boldsymbol{T_x}$, $\boldsymbol{E}$ is the activation energy and $\boldsymbol{R_{gas}}$ is the gas constant. This type of analysis required DSC parameters from continuous heating experiments at various heating rates between 5 and 80°C/min.

The powders did not require any special preparation. For each experiment we filled ~15mg powder into a Al crucible and chose an empty Al crucible as an reference. For the splats, we cut them in a way that they just fitted into the Al crucible.

3.8 Transmission Electron Microscopy

The samples were investigated by Transmission Electron Microscopy (TEM). In contrast to scanning electron microscopy, TEM is a technique to characterise very fine microstructures and to provide local information. In this work, TEM measurements were done by using a Philips CM30 operated at a voltage of 300kV, thus ensuring transmission through metallic glasses up to a thickness of about 80 nm. Bright field (BF), dark field (DF), and selected area diffraction (SAD) images were recorded using AGFA films and imaging plates.

A free-source software named “ImageJ” was used to adjust the brightness and contrast of TEM images. The crystallite size was calculated by fitting the cross section area of a crystal by a circle. It has to be noted that TEM can only determine a crystallite only locally.

Crystalline phases were identified by comparing the electron diffraction patterns with PDF-2-data of the International Centre for Diffraction Data. A gold standard consisted of a Au sputtered on a carbon grid and was used to calibrate the length scale of the 2θ-axis. d values were calculated by Bragg's law using a wavelength of 0.00197 nm, which corresponds to an acceleration voltage of 300 kV [95].

The preparation of TEM specimens of powder particles included the following steps: (1) an epoxy resin was mixed with titanium nitride powder (particle size ranging from 2 to 5 μm) as a medium because of their mechanical properties and sputter yield similar to amorphous and nanocrystalline powders; (2) a small amount of amorphous or nanocrystalline powder was added to the medium and mixed; (3) the mixture was hardened at 80°C for 30 min, resulting in a compact and well processable bulk; (4) bulk mixture was cut this into slices between 5 and 8 μm thick and mechanically polished; and (5) ion milling was applied to obtain the final TEM specimen.

3.9 X-ray Absorption Spectroscopy

X-ray Absorption Fine Structure (XAFS) measurements were performed by X-ray absorption spectroscopy (XAS) at BESSY II at the experimental stations KMC-2 (Ni K-edge and Co K-edge for $Al_{86}Ni_6Co_2Y_{4.5}La_{1.5}$ and $Al_{86}Ni_8Y_6$) and the BAMline (Ni, Ge, Zr, Ag, Pd, Yand La K-edge for other samples), respectively. The experimental setup is schematically shown in Figure 3.5. The experimental stations were equipped with a double-crystal quartz monochromator. Spectra were collected in the fluorescence mode at KMC-2 and in the transmission mode at the BAMline.

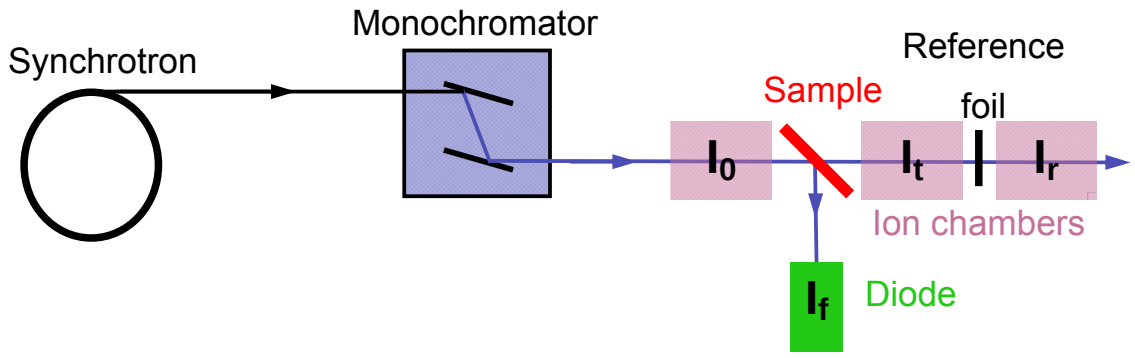

Figure 3.5: Experimental setup for XAFS measurements

Table 3.1: The type and pressure of gases were adjusted to the corresponding energies of edge of each element we measured in this work.

Edge of elements	Energy K-edge (KeV)	Gas in I_0	Gas pressure I_0 (Torr)	Gas in I_t	Gas pressure I_t (Torr)
Co	7709	90%Air 10%Ar	760	100%Ar	200
Ni	8333	90%Air 10%Ar	760	100%Ar	200
Ge	11103	90%Air 10%Ar	760	100%Ar	200
Y	17038	100%Kr	300	100%Kr	300
Zr	17998	100%Kr	300	100%Kr	300
Pd	24350	100%Kr	300	100%Kr	300
Ag	25514	100%Kr	300	100%Kr	300
La	38925	100%Kr	100	100%Kr	760

For the fluorescence mode, the signal was detected by an ionization chamber (I_0) and a diode detector (I_f). The energy calibration for Ni and Co was monitored using reference materials measured with the sample. The energy dependence of the X-ray absorption coefficient ***μ(E)*** is calculated as:

$$\mu(E) \propto I_f / I_0 \qquad (3.4)$$

For the transmission mode, the X-ray intensities were monitored using ionization chambers filled with gases, the type and pressure of which were adjusted to the corresponding energies, see Table 3.1. The energy calibration for the Ni-edge was done by using pure Ni foil as a reference material. The absorption coefficient ***μ(E)*** in transmission mode is given by:

$$\mu(E) = \log(I_0 / I_t) \tag{3.5}$$

The measured EXAFS spectra were transformed into k-space ***χ(k)*** using the standard software combination `ATHENA/ARTEMIS` [96, 97]. Then, the region where the amplitude of the non-weighted χ(k) is significant was Fourier transformed (FT) (for details see Ref [98, 99]). The FT gives a radial distribution function (RDF), modified by the phase shift due to the absorbing and backscattering atoms. In order to obtain a definitive value for the number of nearest neighbours ***N***, the interatomic distance ***R*** and the mean squared relative displacement of the effective interatomic distance $\boldsymbol{\sigma^2}$, we fitted our data by using the EXAFS equation based on the single-scattering approximation[98, 99]:

$$\chi(k) = \sum_i \frac{(N_i S_0^2) F_i(k)}{kR_i^2} \sin(2kR_i + \varphi_i(k)) \exp(-2\sigma^2 k^2), \tag{3.6}$$

where ***F(k)*** and ***φ(k)*** are scattering properties of the atoms neighboring the excited atom, S_0^2 is the energy-independent many-body amplitude reduction factor and ***k*** is the photoelectron wave vector.

The structural data needed for calculating the fitting standards were prepared by applying the `ATOMS` code [100], while the theoretical scattering paths were calculated with the ab-initio software `FEFF` [101], A single-shell model was fitted to the data since it was found to described our data.

4 Local structure of $Al_{85}Ni_{10}La_5$ Metallic Glass after Ball milling

4.1 Results

4.1.1 Microstructure of As-atomized and Ball-milled Powders

Optical micrographs of powder in both as-atomized condition and after different ball milling times are shown in Figure 4.1 (a)-(f). The particle size was found to increase during ball milling to 1200 min followed by a decrease on subsequent milling. The size distribution of particles was roughly estimated by counting ~300 particles from optical micrographs of each powder specimen as shown in Figure 4.2. The mean sizes of powder after ball milling to 120 min, 240 min, 1200 min, and 6000 min are 22.7 μm, 28.8 μm, 70.5 μm, and 65.8 μm, respectively. The particle size of as-atomized powder is out of the resolution of optical microscope, therefore we investigated it by SEM.

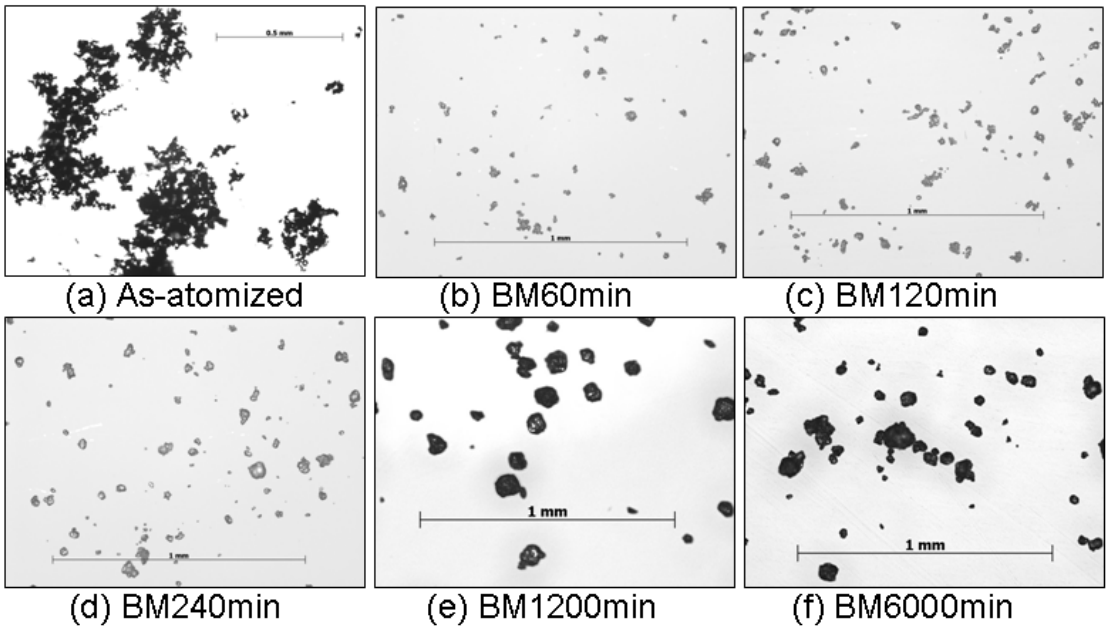

Figure 4.1: Optical micrograph of as-atomized (a) and ball-milled powder particles (b)-(f).

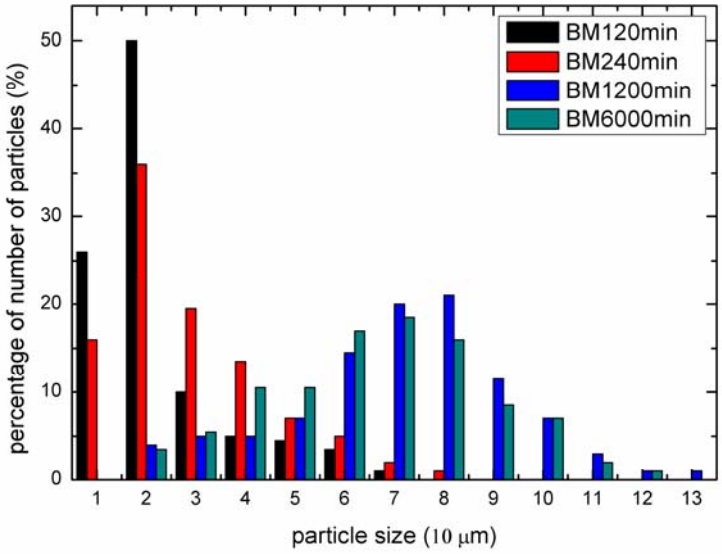

Figure 4.2: Size distribution of powder particles after 4 different ball milling times (120 min, 240 min, 1200 min, and 6000 min).

Microstructures of the powder particles in the as-atomized state and after ball milling for 1200 min as observed by SEM are shown in Figure 4.3 (a) and (b), respectively. The powder parti-

cles in the as-atomized state have a spherical shape and a smooth surface. Small particles of the order of 0.2 μm in size are attached to the surface of powder particles with particle diameters of several micrometers. The mean particle diameter was determined to d=11±1μm [20]. Furthermore, the surface of the particles has got rough compared to the as-atomized particles pointing to severe plastic deformation of the individual particles and cold welding during ball milling, and explaining the increase in particle size by about one order of magnitude. The decrease in particle size beyond 1200 min is ascribed to embrittlement due to the precipitation of fcc-Al nanocrystals and the related change in composition of the residual amorphous matrix.

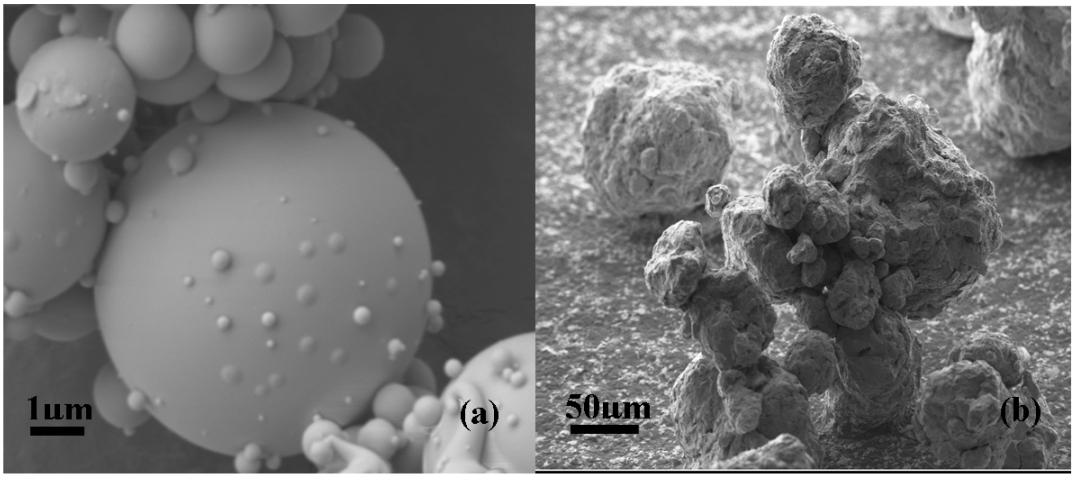

Figure 4.3: Scanning electron micrograph of $Al_{85}Ni_{10}La_5$ in the as-atomized condition (a) and after ball milling to 1200 min (b).

4.1.2 Crystallization during Continuous Heating Characterised by DSC

Figure 4.4 shows the DSC signal measured during continuous heating of the powder in the as-atomized state and after ball milling at room temperature for different times using a heating rate of 20 K/min. The DSC curve of the as-atomized powder reveals a pronounced glass transition at T_g = 253.5°C as shown in Figure 4.4 (b). The pronounced glass transition points to the glassy nature of the as-atomized material. As a function of ball milling time the glass transition gradually vanishes. This might be due to a fragile to strong glass transition in accordance to Louzguine et al.[102] who observed the disappearance of a glass transition in Al-Y-Ni-Co-Sc glasses with an increase of Sc content.

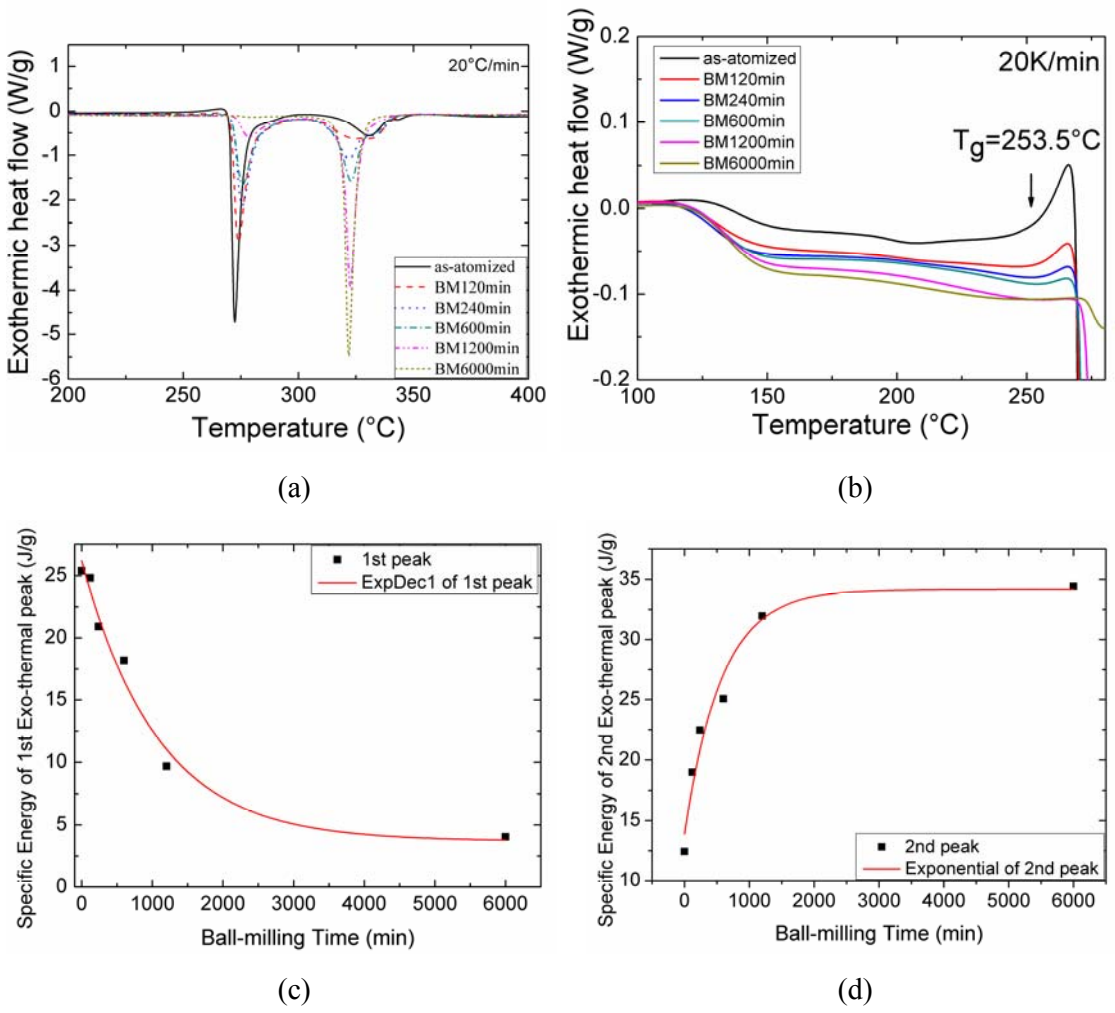

Figure 4.4: DSC curves of $Al_{85}Ni_{10}La_5$ powders ball-milled at room temperature to different times in the whole measured temperature range (a) and in the temperature range up to the glass temperature (b). (c) and (d), respectively, are the specific energy of 1st and 2nd exo-thermal reactions..

The heat release of the first exothermal reactions decreases with increasing ball milling time and vanishes nearly completely after ball milling to 6000 min, while the second peak increased. This is ascribed to the deformation-induced precipitation of fcc-Al crystals which can be proved by X-ray diffraction (XRD) and transmission electron microscopy (TEM). This partial crystallization leads to the related change in composition of the residual amorphous phase that has a different thermal stability from the as-sprayed powder. The energy gain cor-

responding to the second exothermal peak due to the formation of the final crystallization products Al_3Ni and $Al_{11}La_3$ is markedly increased during ball milling.

Figure 4.4 (b) illustrates that above 120°C, the structural relaxation releases more heat with increasing ball milling times. This indicates that plastic deformation could perturb the amorphous matrix, e.g. by forming free volume, shear bands or fracture etc.

The specific energy of the 1st exothermic peak integrated over a temperature range between 267.5°C and 300°C and the 2nd exothermic peak between 300°C and 358°C are shown in Figure 4.4 (c) and (d) respectively. The corresponding specific crystallization energies extracted from the two exothermal peaks are fitted by using two exponential functions:

$$E_{1st} = A' * \exp(-t/\tau) + E_0' \tag{4.1}$$

and

$$E_{2nd} = A'' * \exp(\kappa * t) + E_0'' \ , \tag{4.2}$$

where E_{1st} and E_{2nd} are the specific energies of the first and second exothermal peaks, respectively; E_0' and E_0'' are the final values of specific energy of the first and second exothermal peaks after infinite ball milling time; A' and A'' are the differences between the initial and final values of the first and second heat release stages, respectively; t is the ball milling time; τ is the decay rate and κ is growth rate. The fitting results are shown in Table 4.1. The half lifes of the two functions were calculated as 743 min and 408 min, respectively.

Table 4.1: Fitting results of exponential decay function for the first exothermal reaction and of an exponential function for the second exothermal reaction of the DSC curve.

$E_{1st} = A' * \exp(-t/\tau) + E_0'$			$E_{2nd} = A'' * \exp(\kappa * t) + E_0''$		
parameters	fitting	uncertainty	parameters	fitting	uncertainty
A'	22.5	1.8	A''	-20.3	2.1
E_0'	3.7	1.5	E_0''	34.2	1.7
τ	1072	214	κ	-0.0017	0.0005

The exponential decrease of the first exothermal peak during ball milling reflects the precipitation of Al nanocrystals and arrestment of the crystallization of metastable phase (MS) during ball milling, more details see chapters 4.1.4 and 4.1.5. The exponential increase of the second reactions leading to the final products Al_3Ni and $Al_{11}La_3$, indicates a change of thermal property in the residual amorphous matrix.

The peak temperature T_p at which the maximum heat release occurred in the DSC curves changes with heating rate. Thus, the activation energy E related to the crystallization of the fcc-Al was deduced directly from the values of T_p of the first exothermal reaction applying Kissinger analysis [93] and is shown in Table 4.2. The activation energy for the precipitation of fcc-Al was found to decrease from 295 kJ/mol for the as-atomized powder to 240 kJ/mol for the specimen ball-milled to 6000 min. This decrease in activation energy indicates a decrease in the stability of the amorphous phase.

Table 4.2: Activation energy of crystallization of $Al_{85}Ni_{10}La_5$ powder ball-milled for different times.

Alloy condition	E (kJ/mol)
As-atomized	295±11
BM 30min	275±14
BM 60min	286±11
BM 240min	276±13
BM 600min	248±14
BM 1200min	240±13

4.1.3 α-Al Precipitation during Ball milling

In order to assign the exothermal reactions of DSC to crystallization products we performed XRD measurements after each of the ball milling times. The XRD patterns of the material in the as-atomized state and after different ball milling times are shown in Figure 4.5 (a). The XRD pattern of the as-atomized material reveals a broad maximum at $2\theta \approx 37°$ with a shoulder at $2\theta \approx 44°$ pointing to an amorphous structure. We fitted the spectrum of the as-atomized

powder by two Gaussian functions according to Louzguine and Inoue [103] and deduced from the fit to the shoulder a coherency length of 1.9 nm by the use of Scherrer's equation. The coherency length is assigned to nuclei of fcc crystals. Nanocrystals of about the same size have been found in several Al-based amorphous alloys. Sahoo et al. [104] found nanocrystals smaller 2 nm in size in amorphous $Al_{89}Ni_6La_5$ alloy by means of small angle neutron scattering (SANS). Louzguine and Inoue [103] deduced from the shoulders in the X-ray spectra of their Al-based amorphous materials fcc-Al nanocrystals of 2.5–2.7 nm in size. It is obvious from Figure 4.5 (a) that the shoulder at about 44.0° moves to smaller angels ($2\theta \approx 43.5°$) after ball milling for 1200 min and then goes back to about its original value ($2\theta \approx 44.4°$) after ball milling for 6000 min. These shifts in the peak shoulder reflect two different mechanisms acting on the nuclei during ball milling causing an increase and subsequent decrease of the mean atomic distance in the nuclei.

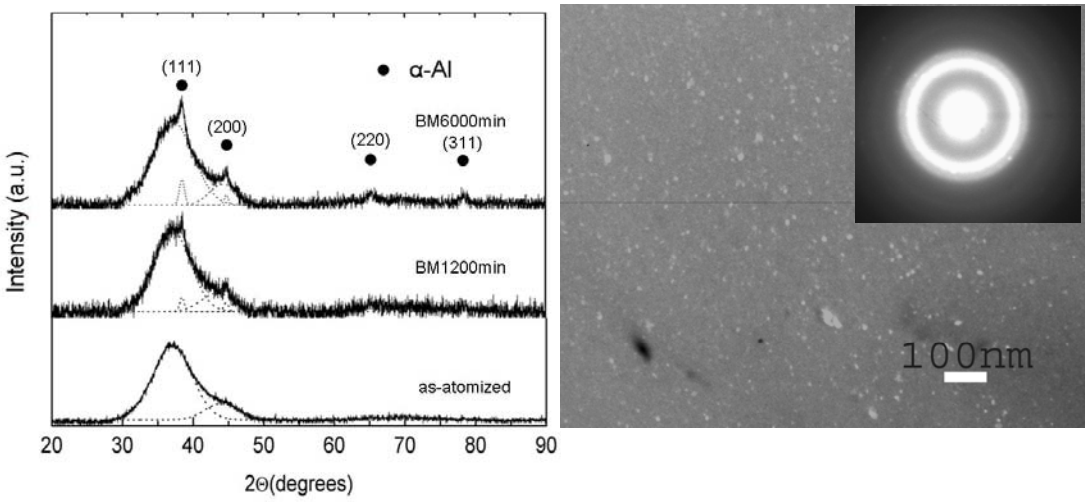

(a) (b)

Figure 4.5: (a) XRD pattern of $Al_{85}Ni_{10}La_5$ powder in as-atomized condition (bottom), after ball milling for 1200 min (middle) and after ball milling for 6000 min. (b) Dark-field image of TEM of $Al_{85}Ni_{10}La_5$ powder after ball milling for 6000 min with SAD ring pattern shows in inner figure. The dotted lines denote separation of two short-order-range broad maximum in as-atomized powder and two diffraction peaks of (111), (200) of α-Al in ball-milled powder.

The XRD pattern of the powder ball-milled to 1200 min reveals reflections of low intensity at $2\theta = 38.5°$ and $2\theta = 44.8°$ which we assigned to the 111 and 200 reflections, respectively, of the fcc-Al phase. The intensity of these peaks increased during ball milling to 6000 min. Furthermore, reflections at $2\theta = 65.3°$ and $2\theta = 78.5°$ are now clearly visible. These maxima are

assigned to the 220 and 311 reflections of the fcc-Al phase. This is in qualitative agreement with the results obtained after high pressure torsion of the same powder where fcc nanocrystals have been detected by means of energy-dispersive diffraction of X-rays [16]. The size of the Al nanocrystals was determined by fitting a Gaussian to the 111- and 200-reflections and by the use of Scherrer's equation taking into account the intrinsic line width. The crystallite size in the specimen ball-milled for 1200 min is 11±1 nm, while the crystallite size in the specimen ball-milled for 6000 min is 12±1 nm. Within the experimental uncertainty, the crystallite size is therefore the same for the two milling times while the volume amount increases from ~3 % to ~6 % by increasing the milling time from 1200 min to 6000 min. Figure 4.5 (b) shows a TEM dark field (DF) image of powder after ball milling for 6000 min along with a selected area diffraction (SAD) pattern. The ring pattern indicates the presence of nanocrystals induced by ball milling. The DF image shows fcc-Al crystallises with size of about 10 nm embedded homogenously in the amorphous matrix. It is generally accepted that formation of fcc-Al nanocrystals during plastic deformation occurs in or close to shear bands which typically have a thickness of ~10 nm [79]. The distance between shear bands after single deformation is of the order of ~1μm [57, 79]. The high volume fraction (6.1%) of Al nanocrystals in the specimen ball-milled for 6000 min therefore suggests a large volume fraction of shear bands produced due to multiple deformations during long ball milling times. The reason for the weak dependence of nanocrystal size on deformation level is not quite clear. It might be the result of a fragmentation mechanism acting at high deformation levels as proposed in [105].

4.1.4 Heat Treatment on As-atomized Powder

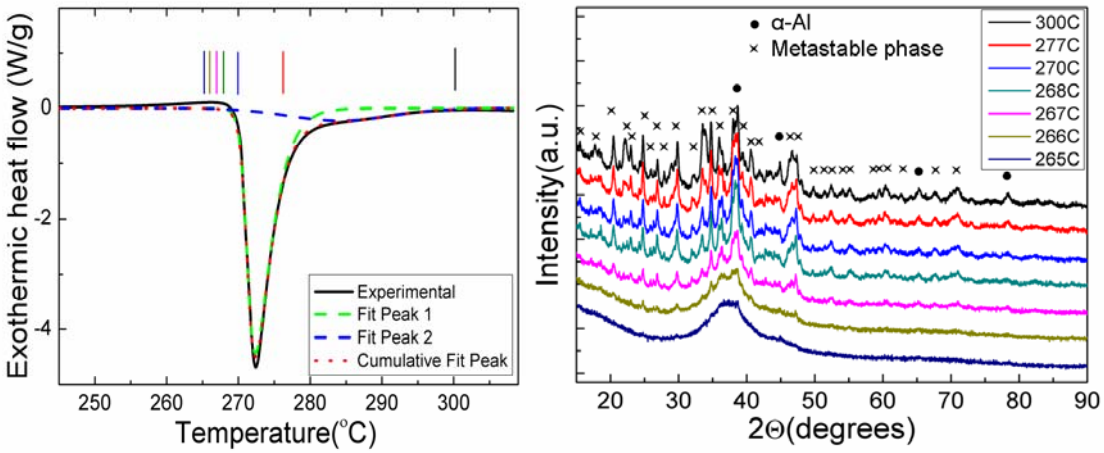

(a) (b)

Figure 4.6: (a) Experimentally determined exothermal peak (bold line) along with two fits (dashed green and dashed blue line) in the temperature range between 260°C and 300°C in DSC of as-atomized powder. (b) XRD patterns of as-atomized powder after continuous heating to different temperatures using a heating rate of 20K/min. The annealing temperatures are marked in (a) by vertical lines with corresponding colours.

Two exothermal reactions can be separated from the DSC curve of $Al_{85}Ni_{10}La_5$ as-atomized powder in the temperature range from 260°C to 300°C using a heating rate of 20 K/min, see Figure 4.6 (a). Due to the asymmetric shape of the DSC signal, fitting functions were chosen as asymmetric double sigmoidal (Asym2Sig) for peak 1 and as Gaussian for peak 2, respectively. XRD patterns of the same specimen after continuous heating to different temperatures are shown in Figure 4.6 (b). We can assign these two heat releases to two crystallization processes, namely the crystallization of α-Al and the formation of a metastable phase. Both reactions start at about the same onset temperature T_x of 270°C. Due to the delay of the temperature decrease after annealing sample to a certain temperature in the DSC, the actual temperatures marked in the XRD patterns in Figure 4.6 (b) should be 3-4°C higher than the temperature of DSC signal during continuous heating shown in Figure 4.6 (a).

In order to distinguish the two crystalline phases, we compared the crystallization speed by calculating the proportion of intensity of two XRD peaks after different annealing temperatures. One diffraction peak located at $2\theta = 65.3°$ is assigned to the (220) lattice plane of α-Al

and another one, at 2θ = 20.3°, is from the metastable phase with lattice spacing of 4.37Å, respectively. These two diffraction peaks were chosen because they can be easily distinguished from the other peaks. The ratio of peak1 area (fcc-Al phase) to peak2 area (metastable phase) is 0.34:1 after annealing to 267°C which is the temperature at which the two crystallization reactions start. The ratio increases to 1.56:1 after annealing to 268°C and to 2.0:1 after annealing to 300°C which is the final heating temperature. The peak ratio in the as-atomized state is lower than in the final state revealing that crystallization of α-Al is faster than of the metastable phase at the beginning of crystallization.

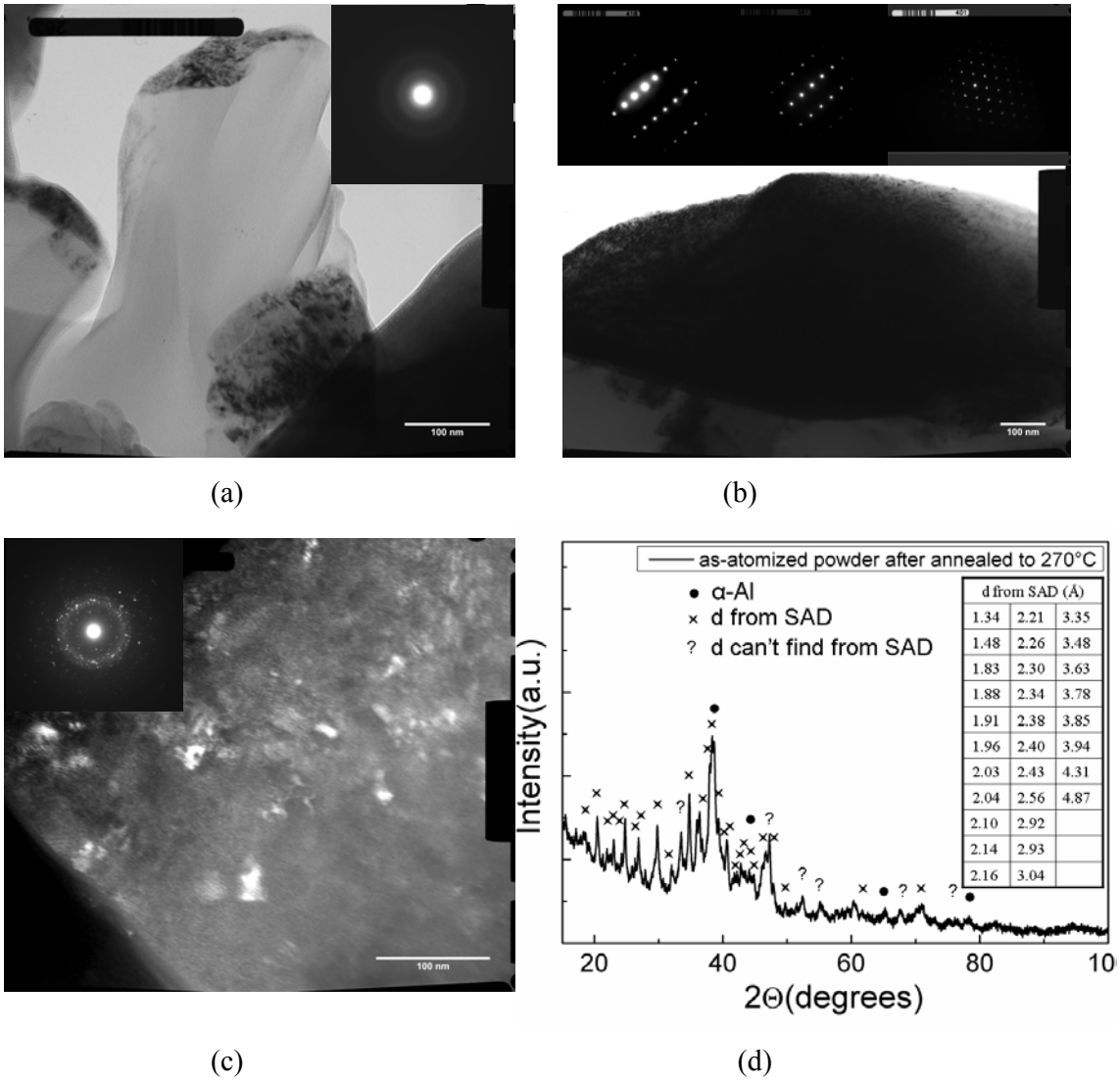

(a) (b)

(c) (d)

Figure 4.7: TEM bright field image of (a) amorphous area, and (b) areas containing fcc-Al, (c) dark field image of metastable phase with SAD pattern of powder after continuous annealing to 270°C. (d) shows the XRD pattern of the same specimen (continuous annealing to 270°C). The inner table shows lattice spacings d determined from the SAD patterns in (c).

Figure 4.7 (a) shows an amorphous area in $Al_{85}Ni_{10}La_5$ powder after continuous annealing to 270°C. Figure 4.7 (b), (c) show fcc-Al crystallized and grown up to ~ 1µm, while metastable phases stay at a scale of 10 nm, which proves the experimental finding from XRD above. The lattice spacing d determined from the SAD pattern is shown in the inner table of (d). Most of the diffraction peak positions in the SAD pattern of the metastable phase match with XRD peaks, while a few diffraction peaks in the XRD pattern were not found in the SAD pattern. This may be due to a few lattice planes that were not visible in SAD under the recorded conditions of Figure 4.7 (c).

4.1.5 Heat Treatment of Ball-milled Powder

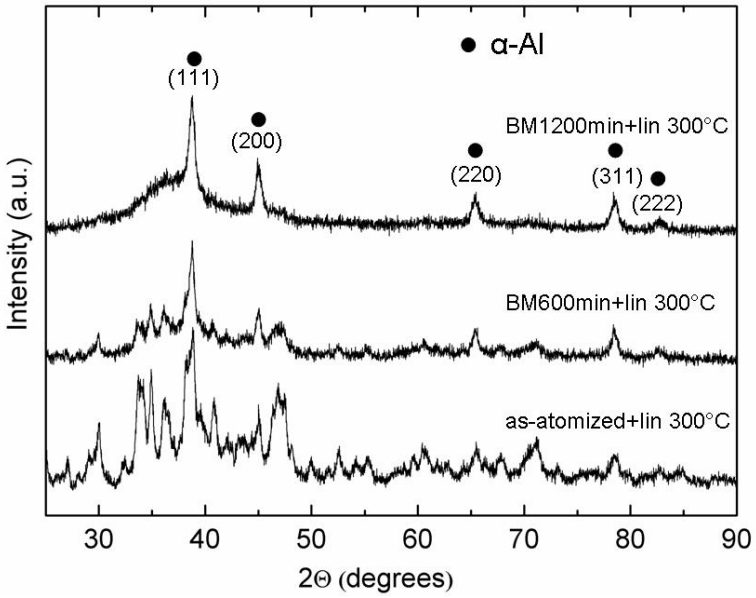

Figure 4.8: XRD pattern of $Al_{85}Ni_{10}La_5$ powder in the as-atomized condition (bottom), after ball milling to 600 min (middle), and after ball milling to 1200 min (top), each after additional annealing by linear heating to 300°C.

Figure 4.8 shows the XRD pattern of as-atomized powder and of powder ball-milled for 600 min and 1200 min, each thermally treated to 300°C with 20 K/min. The maxima in the intensities of the as-atomized powder can be indexed by the reflections of fcc-Al and by the maxima of an unknown metastable phase. Ball milling for 600 min leads to a relative decrease of the maxima of the metastable phase which completely vanish after ball milling to 1200

min. This leads to the conclusion that plastic deformation by ball milling leads to a change in the crystallization behaviour due to a shift of the composition of the residual amorphous matrix caused by the precipitation of fcc-Al.

4.1.6 Temperature Effects during Mechanical Alloying

Ball milling at temperatures between 80°C and 100°C for 240 min leads to an enhanced precipitation of fcc-Al nanocrystals compared to ball milling at room temperature, while ball milling at temperatures between -80°C and -50°C for 240 min hardly leads to the formation of fcc-Al precipitates (see Figure 4.9 (a)). Although all of the milling temperatures are far below the crystallization temperature, the precipitation process is affected in a way that higher temperatures enhance crystallization while lower temperatures hamper crystallization of fcc-Al nanocrystals. Our results therefore suggest a combined influence of temperature and plastic deformation on crystallization. This interpretation is in qualitative agreement with the finding of Lee et al. [106] who studied the influence of uniaxial pressure and plastic deformation of a Cu-based metallic glass. They found that hydrostatic pressure reduces the activation energy for nucleation while shear stress lowers the activation energy for the diffusion of a matrix atom to the nucleus. In ball milling experiments, both hydrostatic pressure and shear stresses act on the powder particles [107]. We therefore conclude that the activation energies for nucleation and growth during ball milling of $Al_{85}Ni_{10}La_5$ powder are also decreased, resulting in deformation-induced precipitation of fcc-Al in the amorphous matrix.

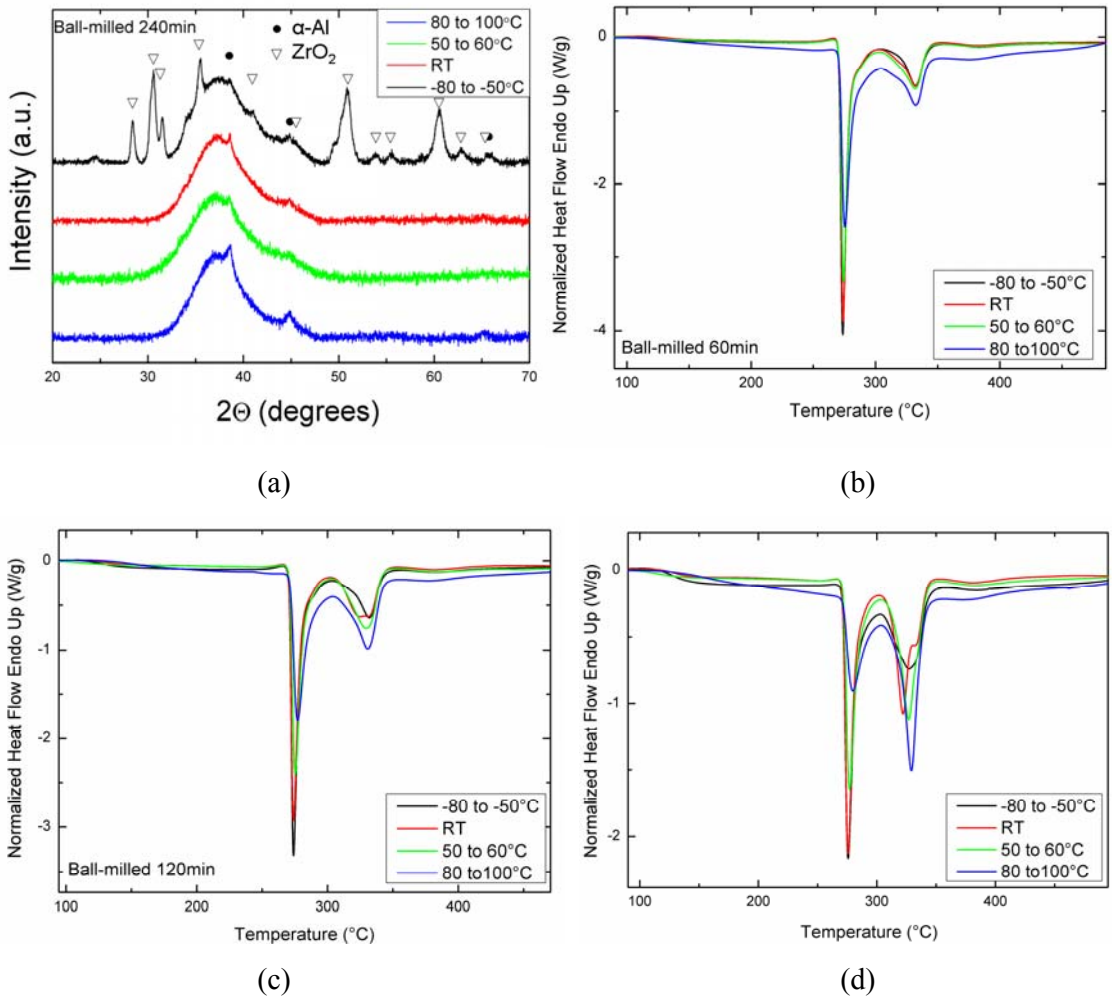

Figure 4.9: (a) shows XRD patterns of $Al_{85}Ni_{10}La_5$ powder ball-milled for 240 min at low temperature (LT; -80°C < T < -50°C, green), at room temperature (RT; blue), at intermediate temperature (IT; 50°C < T < 60°C, red) and at high temperature (HT; 80°C < T < 100°C, black). The peaks marked by triangles are due to ZrO_2 rubbed off the container and the balls during low temperature milling. DSC curves of $Al_{85}Ni_{10}La_5$ powders ball-milled at high temperature (HT), room temperature (RT), intermediate temperature (IT) and low temperature (LT) for 60 min (b), 120 min (c) and 240 min (d).

The influence of temperature on the precipitation of fcc-Al is also reflected by the DSC curves measured after ball milling for 60 min, 120 min and 240 min at different temperatures see Figure 4.9 (b-d)). First, the heat release assigned to the precipitation of Al-fcc nanocrystals decreases with increasing ball milling temperature. This means that the volume fraction of fcc-Al nanocrystals increases with increasing ball milling temperature in agreement with the

results from XRD measurements. Furthermore, the effect of the glass transition is reduced with increasing ball milling temperature.

4.1.7 Change of Local Structure after Ball milling

4.1.7.1 Local Structure around Ni Atoms in Ball-milled Powder

The local structures around Ni atoms in $Al_{85}Ni_{10}La_5$ alloy in the as-atomized state and after different ball milling times were investigated by measuring the extended X-ray absorption fine structure (EXAFS) via extended X-ray absorption spectroscopy (XAS). The experimental data were measured in the transmission mode. The EXAFS oscillations, χ, versus the energy, E, of the photoelectrons were determined by normalization and background removal. The normalized Ni K-edge EXAFS signals $k\chi(k)$ for different ball milling times are compared in Figure 4.10 (a). The spectra recorded after different milling times look similar which means that no large changes in local order around Ni are induced by ball milling. The signals show small and monotonous oscillations pointing to the lack of long-range order which is typical for amorphous alloys.

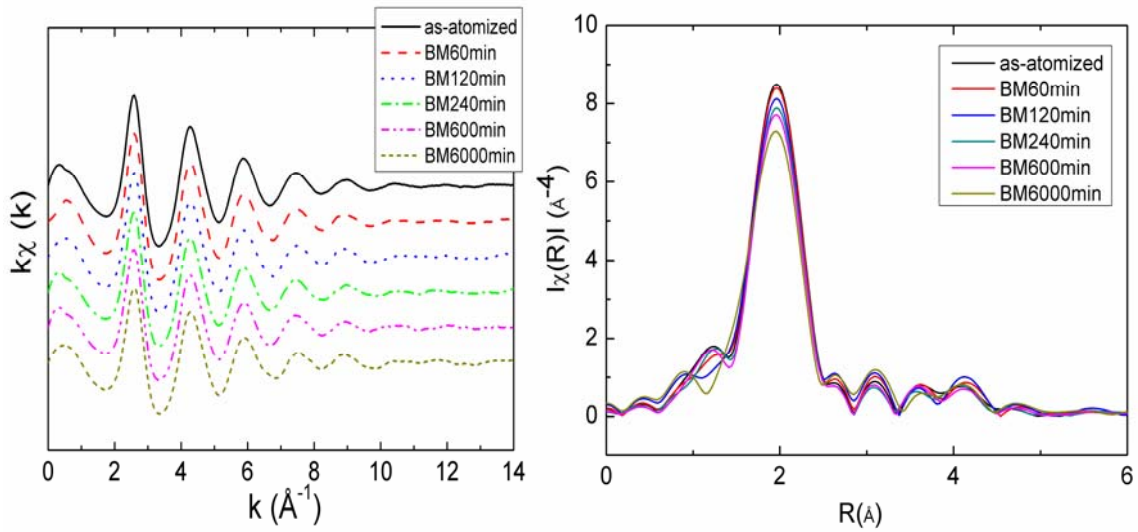

Figure 4.10: (a) Experimental kχ(k) and (b) Fourier transforms of the Ni EXAFS functions of $Al_{85}Ni_{10}La_5$ in the as-atomized condition and after ball milling for different times.

The Fourier transforms (FTs) ***χ(R)*** of the normalized spectra were calculated using a Hanning window between 2.5 and 12 $Å^{-1}$ in the *k* space. The single peak observed points to an amorphous structure without any medium-range order. The modulations of the FTs are similar to the radial distributions between the coordination atoms neighbouring the absorbing atom. However, the peak is shifted to lower R-distance due to a phase shift of the photoelectrons during scattering from the potentials of the absorbing atom and its nearest neighbours. Because of this phase shift, the scale on the x-axis of the FTs cannot directly explain the environments of the atoms. To obtain more accurate information of local structure, simulations are required.

According to Figure 4.10 (b), the peak amplitude of the FTs decreases with increasing ball milling time from the as-atomized state to ball milling times of 6000 min. This trend indicates a decrease of the coordination number ***N*** or an increase of the mean squared relative displacement of the effective interatomic distance, σ^2. The peak position reveals no clear shift on the ***R***-scale suggesting a constant bond length of atoms neighboured to the absorbing atom**.**

Parameters of local environment, for instance of ***N***, ***R***, and σ^2, were fitted by the ab-initio FEFF software using a single-shell model, assuming Al nearest neighbours. Only the normalized spectra, their FTs and the fits to the data of as-atomized powder are shown in Figure 4.11. The windows for fitting in k-space are from 2.5 to 12 $Å^{-1}$, in R-space from 1.1 to 2.8 Å as indicated by a green dashed line in Figure 4.11 (b), because the information of the first coordination shell around the absorbing atom is obtained from the first peak. The R-factor which is used to describe the goodness of fits is about 2×10^{-3}, indicating good quality of the fit. The amplitude reduction factor S_o^2 is defined by the inelastic losses of central atom [98, 99] and is normally in the range from 0.8 to 1.1. In this work, it is fixed to 0.9 for Ni [108] to calculate the ***N***. The fits to the data of the ball-milled powders are not shown here.

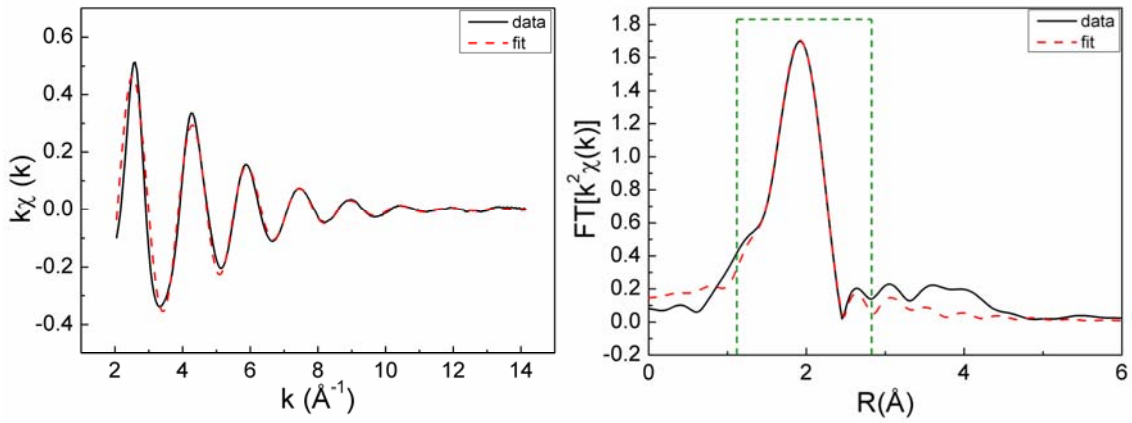

(a) (b)

Figure 4.11: Comparison of the experimental data (solid line) and calculated single-shell fit (dashed line) of Ni K-edge EXAFS data of as-atomized powder in k-space (a) with windows from 2.5 to 12 Å^{-1}, and in Real space (b) with windows from 1.1 to 2.8 Å.

Results of the fits to the data are listed in Table 4.3. The distance between the absorbing Ni atom and the coordination shell with Al atoms, ***R (Ni-Al)***, remains constant as 2.44 Å both in the as-atomized condition and after different ball milling times. Within experimental uncertainty, the mean squared relative displacement of effective interatomic distance, σ^2, is the same for all milling times. ***N*** decreases from ~6 to ~5 with increasing ball milling time.

*Table 4.3: Parameters obtained by using the one-shell model to fit the Ni-EXAFS data of $Al_{85}Ni_{10}La_5$ amorphous alloy after ball milling and contentious heating to 150°C for 10 min. **N**: number of nearest neighbours; **R:** distance of nearest neighbours; σ^2: mean squared relative displacement of the effective interatomic distance.*

Alloy treatment	Absorbing atom	N	R (Å)	σ^2 (Å^2)
as-atomized	Ni	5.9±0.3	2.44±0.01	0.0095±0.0010
BM60min	Ni	5.7±0.3	2.44±0.01	0.0092±0.0010
BM120min	Ni	5.3±0.3	2.44±0.01	0.0089±0.0010
BM240min	Ni	5.2±0.2	2.44±0.01	0.0089±0.0010
BM600min	Ni	5.1±0.2	2.44±0.01	0.0089±0.0010
BM6000min	Ni	5.0±0.4	2.43±0.01	0.0094±0.0018
BM240Anealed	Ni	5.5±0.3	2.44±0.01	0.0089±0.0010

The data of ***N*** were fitted by an exponential decay function $N = A_1 * \exp(-t/w) + N_0$, see Figure 4.12, where N_0 is the coordination number after infinite ball milling time, A_1 is the difference of ***N*** and N_0, and ***w*** stands for the decay rate. ***N*** follows an exponential decay function with half life of 99 min.

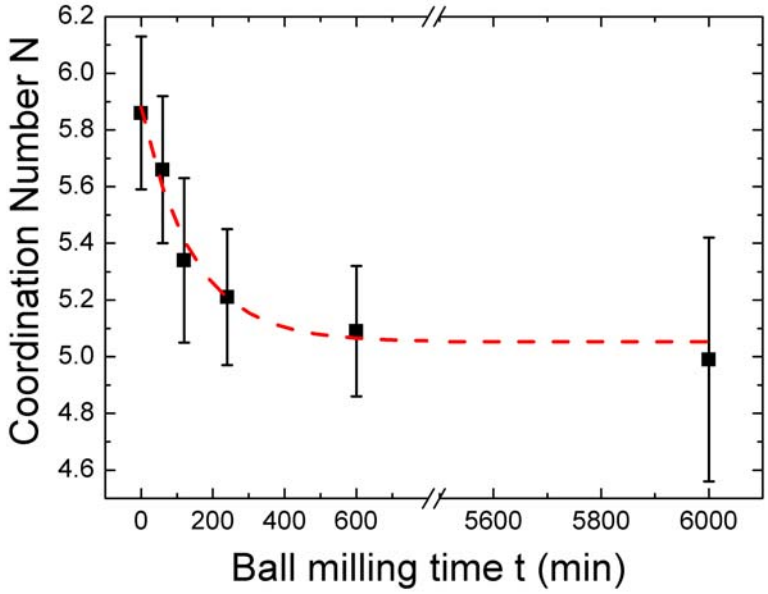

*Figure 4.12: Coordination number **N** as a function of ball milling time shown as black notes and the fitting curve using an exponential decay function (red line).*

Ni-EXAFS was also measured in powder ball-milled for 120 min and subsequently annealed to 150°C for 10 min. This temperature is far below T_g and no significant crystal growth was found in this specimen. The FTs of the EXAFS spectra are shown Figure 4.13. A decreasing peaks height can be obtained from the as-atomized condition to the powder after ball milling for 120 min, while the intensity of peak recovered after annealing. These two opposite trends can be observed clearly in the insert figure.

The fitting parameters (***N, R,*** σ^2) are 5.5±0.3, 2.44±0.01Å, 0.0089±0.0010Å^2, respectively, see Figure 4.13. Comparing the fitting results with the specimen before annealing, which marked as ***BM120min***, see Table 4.3, the value of ***N*** is slightly larger after annealing, but the difference lies within the experimental uncertainty.

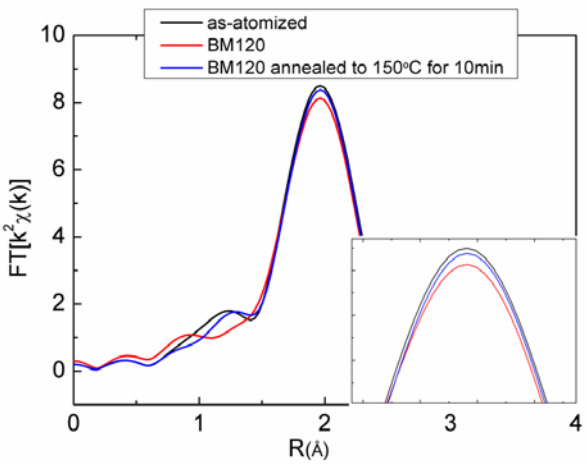

Figure 4.13: Fourier transforms of the Ni EXAFS functions of $Al_{85}Ni_{10}La_5$ at as-atomized condition, after ball milling for 120 min and after annealing to 150°C for 10 min.

4.1.7.2 Local Structure around La Atoms in Ball-milled Powder

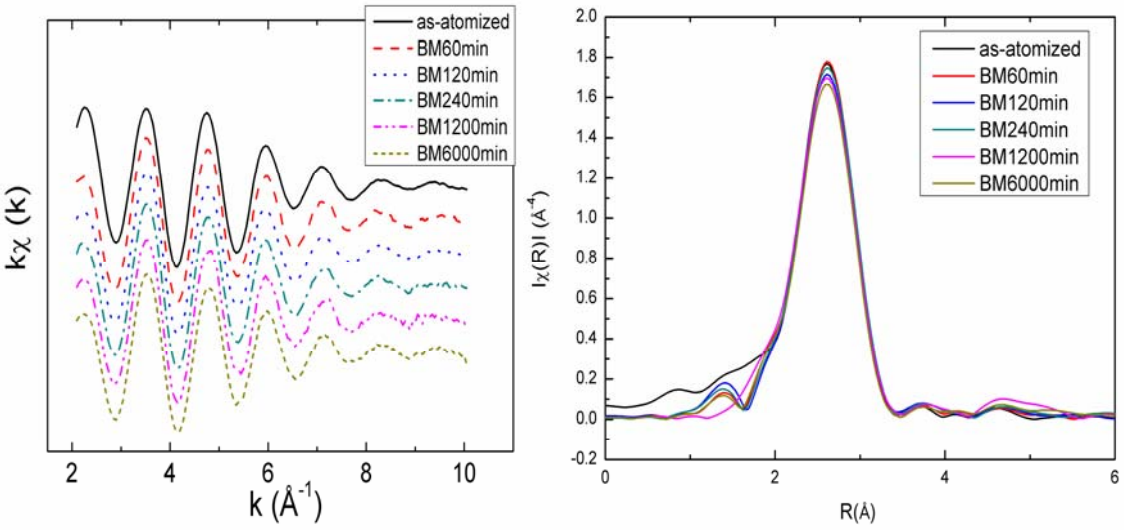

Figure 4.14: (a) Experimental kχ(k) and (b) Fourier transforms of the La EXAFS functions of $Al_{85}Ni_{10}La_5$ in the as-atomized condition and after different ball milling times.

La and Ni-EXAFS experiments were performed on the same specimen of $Al_{85}Ni_{10}La_5$ in the as-atomized condition and ball-milled for different times. The normalized La-EXAFS oscillations ***kχ(k)*** are presented in Figure 4.14 (a). The Fourier transformations of the normalized

La-EXAFS signals shown in Figure 4.14 (b) were computed using a Hanning window between 2.5 and 10Å^{-1}. The normalized La-EXAFS spectra look similar suggesting similar local structure around La in all specimens. Furthermore, the simple and monotonous shape of normalized signals and the single peak of the FTs suggest an amorphous structure. Figure 4.14 (b) shows a trend of FTs peak between 1.6 and 3.5 Å to decrease with increasing ball milling time. The fit spectra of as-atomized powder obtained by using a single shell of Al atoms around the La atom are shown in Figure 4.15. The experimental data and the fits to the data match quite well. The data from specimens with different ball milling times are not shown here because they have the same fit quality.

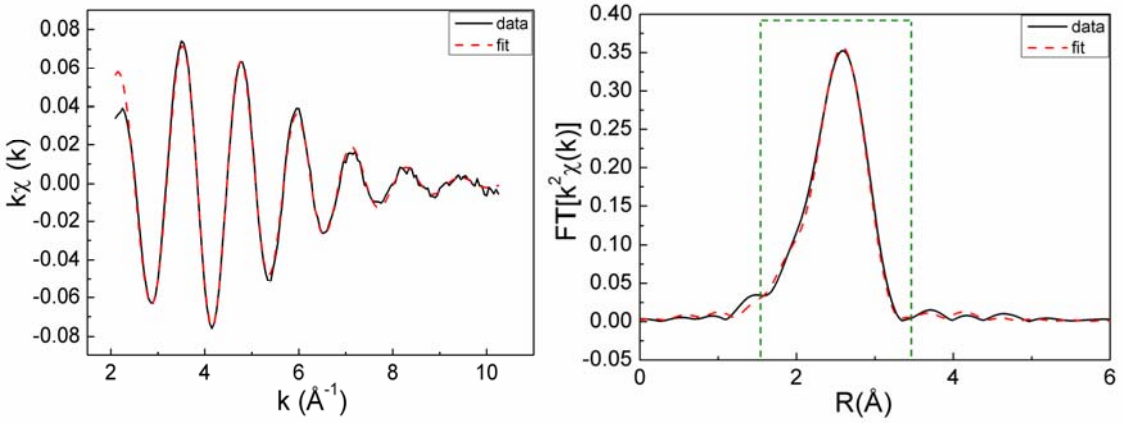

(a) (b)

Figure 4.15: Comparison of the experimental data (solid line) and calculated single-shell fit (dashed line) of La K-edge EXAFS data of as-atomized powder in k-space (a) with windows from 2.5 to 10 Å^{-1}, and in FTs space (b) with windows from 1.6 to 3.5 Å.

The La K-edge EXAFS data of powders in the as-atomized condition and ball-milled for various times were fitted using the single-shell model, resulting in R-factors of around 4 x 10^{-3} which indicated good quality of each fit. The $\boldsymbol{S_o^2}$ of La was set to 0.7 according to Bowron's work [109, 110]. The parameters obtained by fitting are shown in Table 4.4. The number of nearest neighbours decreases from 18.1 to 16.5 with increasing ball milling time. However, the fitting uncertainty is too large to indicate a clear trend.

The coordination number of La is plotted in Figure 4.16. It decreases strongly at small ball milling times, a trend we also found in the local structure of Ni, see chapter 4.1.7.1. ***R*** was

found to be constant, ~3.36 Å. This value is the same as the theoretical value of 3.31 given by the sum of the atomic radii of Al and La [33]. σ^2 at the La K-edge is constant, 0.018, which is bigger than σ^2 for the Ni K-edge, revealing stronger disorder of the local environment arround La. It is conmon in amorphous alloys that bigger atoms have more nearest neighbours, which leads to a stronger mismatch of the first coordination shell.

*Table 4.4: Parameters obtained by using the one-shell model to fit the data of the La K-edge. **N**: number of nearest neighbours; **R:** distance of nearest neighbours; σ^2: mean squared relative displacement of the effective interatomic distance.*

Alloy treatment	Absorbing atom	***N***	***R*** (Å)	σ^2 (Å^2)
as-atomized	La	18.1±2.6	3.37±0.05	0.018±0.003
BM60min	La	17.6±1.3	3.35±0.03	0.018±0.001
BM120min	La	17.4±1.4	3.36±0.03	0.018±0.002
BM240min	La	17.5±1.6	3.36±0.03	0.018±0.002
BM1200min	La	16.8±1.5	3.34±0.03	0.018±0.002
BM6000min	La	16.5±1.4	3.35±0.03	0.018±0.002

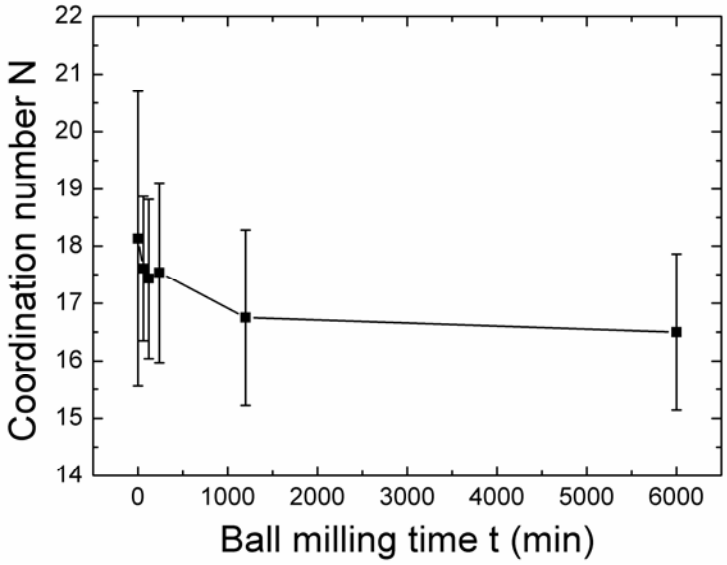

Figure 4.16: Coordination number of La atom in $Al_{85}Ni_{10}La_5$ amorphous powder as a function of ball milling time.

4.2 Discussion

4.2.1 Thermodynamical Model of the Crystallization of $Al_{85}Ni_{10}La_5$

Chapters 4.1.4 and 4.1.5 present the results obtained by DSC, XRD and TEM analysis of crystallization of $Al_{85}Ni_{10}La_5$ powder in the as-atomized state and after ball milling for various times. We can conclude for the path of crystallization of as-atomized powder that 1) from room temperature to 300°C, the powder transforms from the fully amorphous state to a mixed state comprising fcc-Al + metastable phase (MS) + residual amorphous phase. The fcc-Al and The MS phase occurred at about the same temperature T_x. Zhuang et al. [111] also found that the crystallization process of the $Al_{89}Ni_5La_6$ amorphous alloy is governed by an simultaneous reaction rather than by a primary reaction; 2) from 300°C to 500°C, the mixture of MS phase and partial glassy phase transforms to Al_3Ni and $Al_{11}La_3$. During ball milling, fcc-Al nanocrystals precipitate in the amorphous matrix and after continuous heat treatment of ball-milled material to 300°C the volume fraction of the MS phase is lower and vanishes after ball milling for 6000 min and continuous heat treatment to 300°C.

A thermodynamic model to explain the DSC and XRD results of crystallization of $Al_{85}Ni_{10}La_5$ alloy of as-atomized condition and after ball milling during annealed is shown in Figure 4.17.

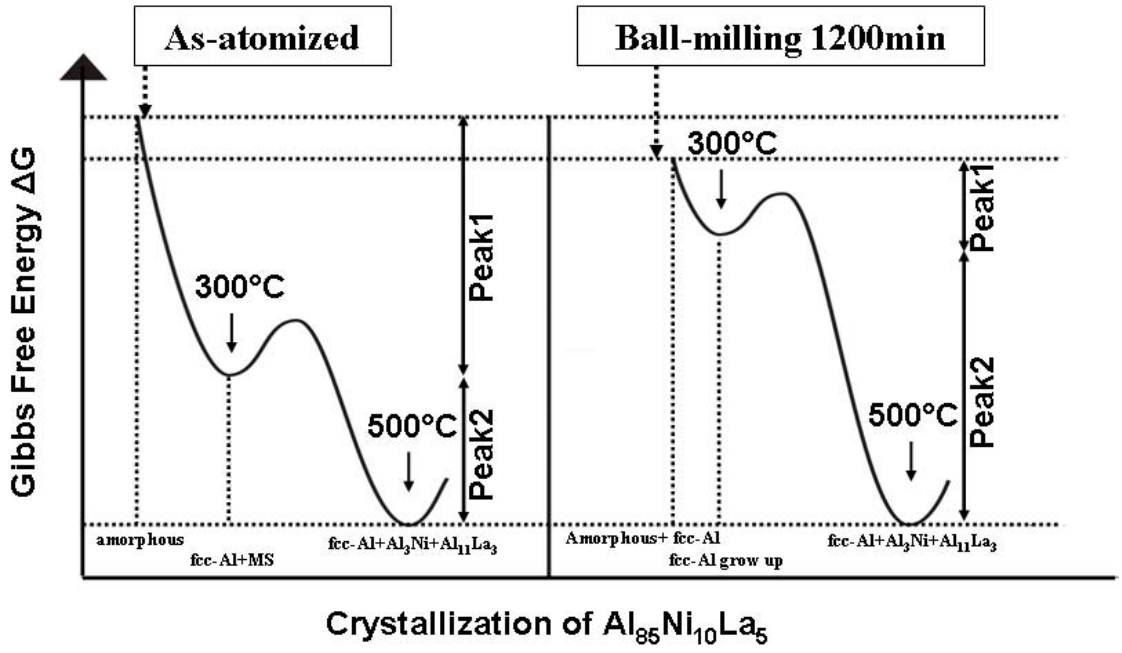

Figure 4.17: Thermodynamic model of crystallization of $Al_{85}Ni_{10}La_5$ alloy in the as-atomized condition and after ball milling to 1200 min and subsequent annealing.

Ball milling reduces the Gibbs free energy ΔG of the alloy at room temperature due to inducing the fcc-Al precipitates, but causes an increase in ΔG at 300°C because of avoiding crystallization of the metastable phase. Therefore, the 1st peak (peak 1) of heat release in the DSC curve decreases while the 2nd peak (peak 2) increases as a function of ball milling time. Two opposite mechanical processes during ball milling can be identified, which are (i) formation of fcc-Al precipitates and (ii) increase in thermal stability of the residual amorphous matrix.

4.2.2 Size Limitation of Fcc-Al Nanocrystals

Nanocrystalline Al is commonly produced in the Al-based amorphous alloys by either isothermal annealing or by lowering the quenching rate, e.g., reducing the wheel speed during melt quenching [112]. Radiguet et al. [113] investigated $Al_{89}Ni_6La_5$ amorphous alloy by 3D-AP (three-dimensional atom probe) and found α-Al particles with size of 12 nm which were almost pure Al and which were surrounded by a La-rich shell which controls the growth and

limits the size of α-Al precipitates. The reason for the formation of the La-rich shell was ascribed to the low diffusivity of the large La atoms [114].

However, in our work, a large fcc-Al crystal of Ø~1μm was found in the as-atomized powder continuously annealed to 270°C, indicating that segregation-controlled nanocrystallization during heat treatment in $Al_{85}Ni_{10}La_5$ did not occur. The crystallization behaviour also differs largely from that of $Al_{89}Ni_6La_5$ as described by Radiguet et al. In Sahoo's work [75, 104], investigation of various Al-Ni-La amorphous alloys with minor compositional differences is reported. A comparison of the DSC and XRD results of different alloys ($Al_{90}Ni_6La_4$, $Al_{89}Ni_6La_5$, $Al_{88}Ni_6La_6$, $Al_{87}Ni_6La_7$, $Al_{88}Ni_8La_4$, and $Al_{87}Ni_8La_5$) reported in Sahoo's work shows that small changes of element concentration could induce large differences in crystallization behaviour. However, the DSC results of all the alloys above have a common feature which is the lower intensity of the primary exothermal peak compared to the second exothermal peak. Furthermore, the first heat release of most of these alloys only formed fcc-Al except in $Al_{88}Ni_6La_6$ and $Al_{87}Ni_6La_7$ which formed fcc-Al along with small amounts of bcc-phase. Wilde and Perepezko [2, 115, 116] investigated nanocrystallization in several Al-rich metallic glasses, e.g. $Al_{92}Sm_8$, $Al_{88}Y_7Fe_5$ and $Al_{87}Y_7Fe_5Pb_1$ and found a similar small exothermic peak of DSC signal during primary crystallization of fcc-Al. The $Al_{85}Ni_{10}La_5$ alloy used in this work shows a large exothermic peak during primary crystallization with a specific energy of 25.5J/g and a small heat release of the second exothermal peak with the a specific energy of 9.5J/g. This demonstrates that the crystallization pathway of $Al_{85}Ni_{10}La_5$ alloy is completely different from those Al-Ni-La alloys. As we elaborated in 4.2.1, a simultaneous reaction rather than a primary reaction is the reason for the invalidation of the segregation-controlling function of the La shell.

Although in the annealed $Al_{85}Ni_{10}La_5$ alloy no size limit for the fcc-Al nanocrystals is observed, size-controlled crystallization was found during ball milling. The particle size of fcc-Al remains at about 10 nm even after ball milling 6000 min. Hence, according to Radiguet's work [113], a core-shell structure might limit the crystal size during ball milling process.

The limitation of the size of nanocrystalline Al during ball milling might be also due to shear band controlling. Wilde et al. [87] proved by TEM analysis that nanocrystals developed only within shear bands during plastic deformation. As a result of the increased atomic mobility in

the shear bands, which induces primary crystallization of Al, the atomic mobility is limited outside the shear bands so that the Al crystallite can only grow up to the thickness of the shear bands. The thickness of shear bands in metallic glasses has been characterized as ~10 nm [117]. Therefore, at room temperature, which is much lower than the glass transition temperature, the size of Al nanocrystals could not grow to more than the thickness of the corresponding shear band.

4.2.3 Deformation Mechanism

The question whether the mechanism of formation of plastic deformation-induced fcc-Al nanocrystals is thermal or athermal has received appreciable attention during the past two decades. Lewandowski and Greer [84] presented an experimental method based on a fusible coating, which reveals that the temperature rise can reach to a few thousands Kelvin in a few nanoseconds. However, Yang [67] reported only few degrees of temperature increase during severe plastic deformation and the intense heat from the shear bands was easily conducted into the surrounding material, leading to a wider and cooler “hot band” captured by an infrared camera. Furthermore, He [13] pointed out that due to the compositional dependence of the structural stability of Al-based amorphous alloys against ball milling, nanocrystal formation induced by ball milling is different from that caused by a thermal process.

By comparing XRD from ball-milled powders (Figure 4.5 (a)) with heat-treated material (Figure 4.6 (b)), two different primary crystallization pathways can be observed. Fcc-Al and metastable phase developed by heat treatment, while only fcc-Al nanocrystals were found in the powder after ball milling. This indicates that devitrification by ball milling is not only a thermal process. Moreover, Chapter 4.1.6 shows the temperature dependence of fcc-Al precipitation during ball milling. Higher temperatures (far below the crystallization temperature) could enhance precipitation of Al nanocrystals, while at temperatures below -50°C, fcc-Al hardly precipitated. Therefore, a combined influence of temperature and plastic deformation can be concluded. A critical temperature (below which Al precipitates cannot be produced by ball milling) should be determined in the future work.

4.2.4 A Schematic Model of Crystallization by Ball Milling and Subsequent Heat Treatment

To explain the different crystallization behaviour of ball-milled and as-atomized powders, a schematic diagram is shown in Figure 4.18. The $Al_{85}Ni_{10}La_5$ powder in the as-atomized condition has a homogeneous local structure. Zhang [118] reported that quenched-in Al nuclei were found in $Al_{85}Ni_{10}La_5$ alloy and the nanocrystalline Al could be developed by annealing the amorphous powder below the glass-transition temperature. We did not find the exactly same behaviours in our $Al_{85}Ni_{10}La_5$ powder, but the faint crystallization peaks assigned to fcc-Al and a metastable phase in the XRD pattern in Figure 4.6 were found at the same time below the primary crystallization temperature T_x. This finding may reveal quenched-in nuclei of Al and metastable phase embedded in the amorphous matrix.

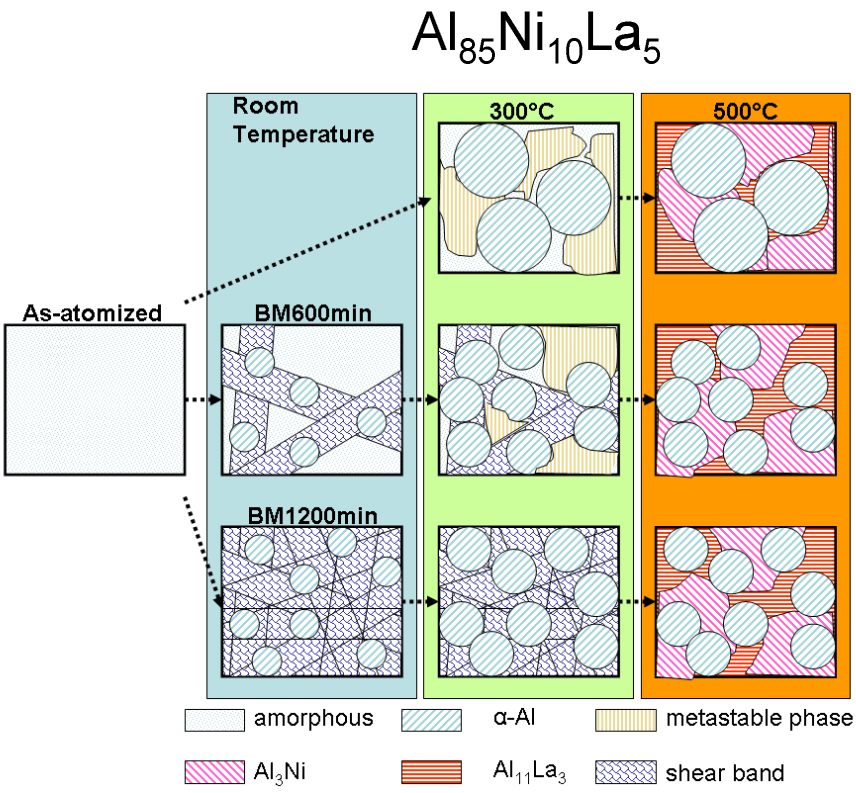

Figure 4.18: Schematic diagram of crystallization of $Al_{85}Ni_{10}La_5$ amorphous alloy along different paths by ball milling and by heat treatment.

After annealing the as-atomized powder to 300°C, a eutectic-like reaction associated with precipitation of the stable fcc-Al phase and a metastable phase which is hard to identify by XRD takes place. Consequently, from the metastable phase and the residual amorphous phase the final stable phases Al_3Ni and $Al_{11}La_3$ evolve after annealing to 500°C. This reaction was shown by DSC curve between 300 °C to 350 °C, see Figure 4.4.

Ball milling is supposed to induce size-controlled precipitation of nanocrystalline Al of ~10 nm in the shear bands and to increase the number density of fcc-Al nanocrystals with increasing ball milling time. At the same time, the amorphous phase in shear bands becomes enriched in La and Ni, making the nuclei of the metastable phase hard to grow. Therefore, the volume fraction of shear bands increases during ball milling while the volume fraction of the residual amorphous phase decreases. After continuous annealing to 300°C, thereby, the volume fraction of the metastable phase after ball milling decreases and consequently vanished in the powder after ball-milled 1200 min.

In summary, two different effects of mechanical deformation have been found: 1) devitrification of metallic glasses by precipitation of fcc-Al. 2) hampering the growth of the nuclei of the metastable phase. In other words, plastic deformation enhances the thermal stability of the residual amorphous matrix.

4.2.5 Local Structure of $Al_{85}Ni_{10}La_5$ As-atomized Powder after Ball milling

The continuous decrease in the number of nearest neighbours in Al-based metallic glass during ball milling is reported for the first time in this work. Table 4.3 shows that the number of nearest neighbours ***N*** of Al atoms at the Ni K-edge in $Al_{85}Ni_{10}La_5$ as-atomized powder is about 6 suggesting the occupation of centres of Al octahedra by Ni atoms as shown in Figure 4.19. This result can be explained by Miracle's model [71]. According to that model, metallic glasses should contain no more than three topologically distinct solutes and these solutes have specific and predictable sizes relative to the solvent atoms. The largest solutes form primary clusters with a large number of nearest neighbours of solvent atoms, while the progressively

smaller solutes occupy interstices of octahedral or tetrahedral clusters. Hence, according to Miracle's model, La forms primary clusters in $Al_{85}Ni_{10}La_5$ and Ni occupies the interstices of Al-octahedra, each Al atom belonging to one La-cluster. During ball milling, the decrease in ***N*** follows an exponential decay function from 6 in the as-atomized condition to 5 after ball-milled 6000 min. A decrease in ***N(Ni)*** was also found by Zhang [119] who performed XRD measurements on amorphous $Zr_{60}Cu_{30}Al_{10}$ and analyzed the radial distribution function and the pair correlation function. He reported that the coordination number decreased after deformation by cold rolling.

The observed decrease in ***N(Ni)*** can result from 1) the change in toplogical structure in the shear bands, or from 2) the composition change in residual matrix to a lower content of Al caused by Al nanocrystal precipitation. If the decreasing trend in ***N(Ni)*** is caused by composition change, the ***N(Ni)*** of ball-milled powder after annealing should decrease further, because fcc-Al nanocrystals growth reduces the content of Al in the residual matrix. However, Figure 4.13 indicates an opposite trend, where the intensity of the EXAFS peak increases when the ball-milled powder is annealed. This interpretation is supported by the fact that the volume fraction of fcc-crystals increases from 3% to 6% from BM1200 to BM6000 while N(Ni) hardly changes within this milling period. This confirms that the topological changes in structure of shear bands are the main reason for the decrease of ***N(Ni)*** during ball milling.

Plastic flow at room temperature in metallic glasses is inhomogeneous and localized in shear bands, which requires dislocation and hence the formation of free volume under applied shear stress [120]. Several models of the atomic structure of shear bands [65, 80, 121] suggest that severe plastic deformation reduces the degree of short-range order in bulk metallic glasses and locally enhance the free volume. According to the model presented in Figure 4.19, localized free space around Ni atoms created by ball milling can be seen as an evidence of increased free volume of local structure by plastic deformation. Our results of decreasing ***N*** around Ni from 6 to 5 (see Figure 4.19) support the idea of deformation-induced increase in free volume in the shear bands. The La-EXAFS results reported in this work also show a decreasing trend of ***N*** if we do not consider the fitting uncertainty.

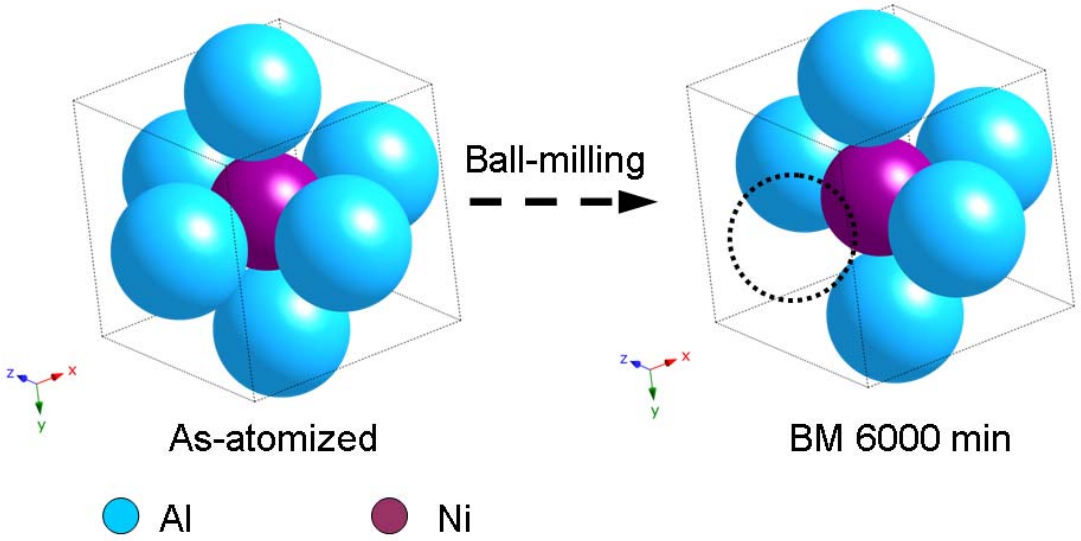

Figure 4.19: Local structure around Ni atoms with neighbouring Al atoms.

At different cooling rates a glass freezes into different states. A crystalline and two glassy states are shown in Figure 4.20. The glass has a lower viscosity or higher diffusivity, and larger specific volume and internal energy when produced at a faster cooling rate. During ball milling, the newly formed glass contains a high density of shear bands, a reduced ordering and a concomitant excess free volume. Therefore, the enthalpy ***H*** and the specific volume ***V*** increase while the viscosity decreases. This indicates that ball milling changes the properties of a glass which is initially in state 1 to the direction of glass 2. Furthermore, during annealing below the crystallization temperature, a broad exothermal reaction which was assigned to structural relaxation was shown in Figure 4.4 (b). The enthalpy ***H*** and the specific volume ***V*** decrease while the viscosity increases which demonstrates that heat treatment leads to an opposite structural trend compared to ball milling. The Fourier transforms of the Ni edge EXAFS signal of ball-milled and annealed powder also support this view, because the intensity of the peak of first coordination decreases with increasing ball milling time and consequently increases after annealing. Zhang's work [119] supports this finding. He found that the coordination number of $Zr_{60}Cu_{30}Al_{10}$ decreases from 13.0 to 12.4 and recovers to 12.7 after annealing. The determination of ***N*** is generally assigned with an appreciable uncertainty. An experimental uncertainty is however not given in Ref. [119].

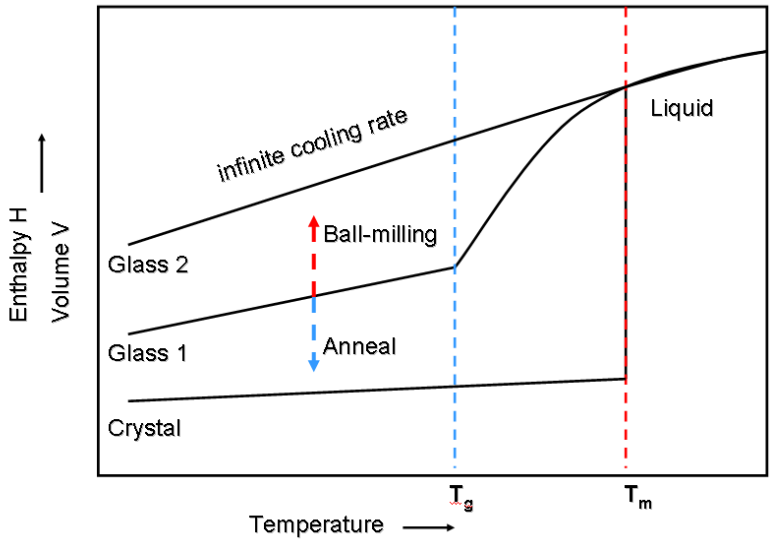

Figure 4.20: The temperature dependence of enthalpy H and specific volume V of $Al_{85}Ni_{10}La_5$ alloy in various states.

The bond length of the Al-Ni, $\boldsymbol{R}_{\text{Ni-Al}}$, is appreciably smaller than the sum of the atomic radii, $\boldsymbol{r}_{\text{Al}} + \boldsymbol{r}_{\text{Ni}}$, reflecting bond shortening due to the covalent environment between Al and Ni atoms. Shortening of TM-Al bonds along with anomalously low coordination numbers has been observed in several amorphous Al-TM-RE alloys [26-32, 36] and has been explained by the strongly covalent character of these bonds: electrons with s-p character of Al are transferred to the d-states of the TM [28].

The consequences of bonds with significant covalent character are evident. First, according to Inoue's criteria for strong glass formation [55], covalent bonds, characterized by large negative heats of mixing, should contribute to enhanced GFA; Second, the covalent character of the bonds may contribute to the high strength of Al-based amorphous alloys.

$\boldsymbol{R}_{\text{Ni-Al}}$ is independent of deformation while $\boldsymbol{N}$ decreases during ball milling. This phenomenon is similar to the phenomenon described in Takeuchi and Jacobs' work where the change of short-range-order of metallic melts is described by decrease in $\boldsymbol{N}$, while $\boldsymbol{R}$ remains unchanged or is only slightly changed when the temperature is increased [122, 123]. They demonstrated that in the liquid state of metal and alloys, the atoms are distributed in random close packed arrangement in which vacancies are included. It is shown that the distance between

neighbouring atoms remains nearly constant, independent of temperature. The thermal volume expansion accompanied by the temperature increase in the liquids is caused by an increase in vacancy concentration accompanied with a decrease in coordination number rather than by an increase in nearest neighbour distance.

4.2.6 Shear Bands Induced by Ball milling

As a function of ball milling time, ***N(Ni)*** decreases an exponentially, as shown in Figure 4.12. A shear band model was proposed to explain this exponential decrease, see Figure 4.21, the shear bands being created by each impact during ball milling. As nanocrystalline Al is generated only within shear bands, we assumed that the changes in local structure around Ni atoms only occurred in the shear bands created by ball milling. The number of nearest neighbours ***N(Ni)***, therefore, is 6 in the area outside the shear band, which can be non-deformed or elastically deformed powder. On the other hand, one neighbouring Al atom is removed from around Ni by deformation resulting in ***N(Ni)*** ≈ 5 in the shear bands. In differently deformed powder, an average ***N(Ni)*** between 5 and 6 was detected in a mixture of non-deformed, elastically deformed and plastically deformed (shear bands) powder. Furthermore, during ball milling, the shear bands overlapped and the overlapping area could not be deformed further. This is the reason for the exponential decrease. Finally, according to the shear band model, the increase of structural relaxations corresponding to the energy release in the DSC curves from 100°C to 170°C, see Figure 4.4(b), is mainly attributed to the addition of shear band relaxation during ball milling.

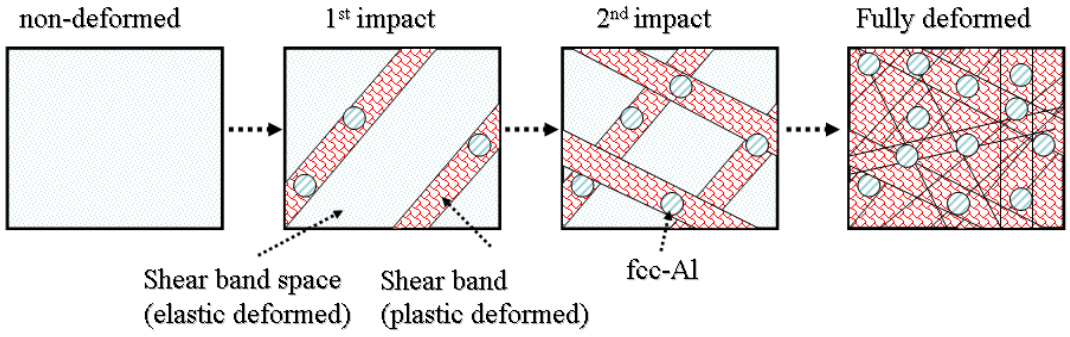

Figure 4.21: Schematic diagrams of the micro- structure changes during ball milling.

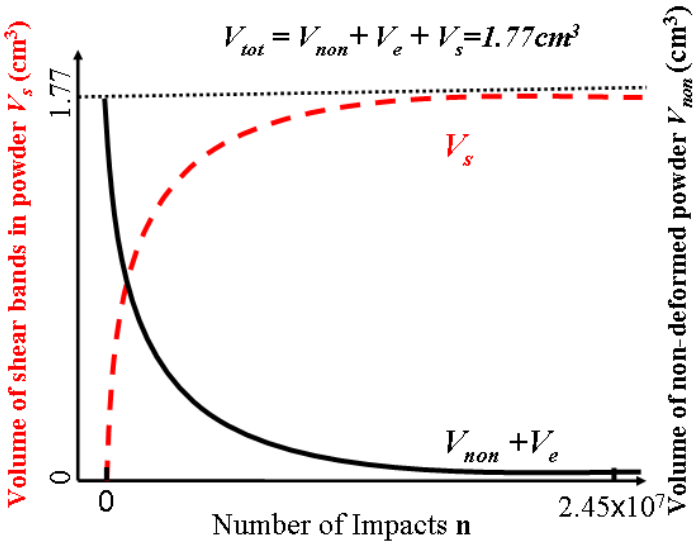

Figure 4.22: Schematic diagram of the volume of shear bands and non-deformed powder as a function of the number of impacts during ball milling.

As shown in Figure 4.12, ***N***(Ni) follows an exponential decay function with decay rate of ***w*** = 143 during ball milling. This indicates that the volume of shear bands in powder also follows an exponential function while the volume of non-deformed and elastically deformed powder $V_{non}+V_e$ follow an exponential decay function with the same decay rate, shown in Figure 4.22. The total volume V_{tot} of $Al_{85}Ni_{10}La_5$ powder in the mill container is 1.77 cm^3 calculated by the function of $V_{tot} = m * \rho_p$, where m = 6.2 g is the mass of the powder in the container, ρ_p is the density of $Al_{85}Ni_{10}La_5$ alloy as given in Vierke's work [20] and is in the range from 3.3 to 3.6 g/cm^3. We used ρ_p = 3.5 g/cm^3 in this work. V_{tot} is obviously equal to the sum of V_s, V_e and V_{non}. The equation for calculating $V_{non}+V_e$ is given by

$$V_{non} + V_e = V_{tot} * \exp(-t / w). \tag{4.3}$$

Then V_s is given by

$$V_s = V_{tot} - (V_{non} + V_e) = V_{tot} * [1 - \exp(-t / w)], \tag{4.4}$$

where t can be used instead of the number of impacts n by ball milling. The ball milling time as a function of number of impacts n is given by

$$t = \frac{n}{2 * n_B * f} \tag{4.5}$$

where n_B is the number of balls of the mill and f is the cyclical frequency of the SPEX mill. In our experiment n_B=2 and f = 1020/min. The factor of 2 in the denominator is due to the fact that the balls collide with the top and back to the bottom of the container each shaking round. Using Eq. (4.5), we can rewrite Eq. (4.4) as

$$V_s = V_{tot} * [1 - \exp(-n / 4080w)] \tag{4.6}$$

By applying Eq. (4.6), we can calculate the volume of shear bands created per impact, V_s'= 3.03 x 10^{-6} cm^3.

A geometrical model of ball milling was introduced by Maurice [124] in 1990. He modelled the collision event on the basis of Hertzian contacts between the grinding media which entrap a certain amount of material volume between the impacting surfaces. Due to the Hertz radius, r_h, is much less than that of the impacting ball, r_B, the contact surface is considered to be flat. Furthermore, the powder particle is much smaller than the entrapped volume. Therefore, the surface of impact volume can be seen as having an infinite curvature relative to the powder.

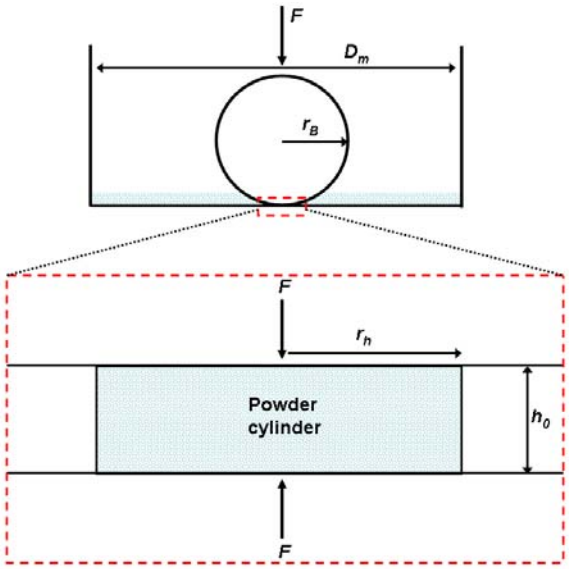

Figure 4.23: Schematic diagram of the collision event. Because of the Hertz radius, r_h, is much less than that of the impacting ball, r_B, the contact surface is considered to be flat. The powder entrapped between the colliding surfaces can be seen as a cylinder with an initial height, h_0.

The material volume V_c entrapped per impact can be estimated to

$$V_c = \pi \cdot r_h^{\,2} h_0 , \tag{4.7}$$

where h_0 is the height of the powder cylinder and r_h is given by

$$r_h = 1.475 v^{0.4} (\rho_B / E)^{0.2} r_B . \tag{4.8}.$$

The equation for h_0 is given by

$$h_0 = [16(L - 2r_B)\rho_B / 3\rho_p C_R][n_B r_B^3 / (3LD_m^2 - 16 n_B r_B^3)], \tag{4.9}$$

where r_B is the radius of each ball, v the velocity of collision, ρ_B the density of ball, E the effect of Young's modulus of the collision body, L the mill length, ρ_p the density of the powder, C_R the mass ratio of balls and powder, and D_m the diameter of the mill container.

All the parameters we used in this work are listed in Table 4.5. The volume of $Al_{85}Ni_{10}La_5$ powder entrapped by each impact is V_c=5.46x10^{-4}cm^3.

Table 4.5: The parameters used in this work for SPEX mixer mill with ZrO_2 balls and ZrO_2 container.

r_B	v	ρ_B	E	L	ρ_p	C_R	D_m	n_B
0.64 cm^3	3.9 m/s	9.7 g/cm^3	186.2 GPa	4 cm	3.5 g/cm^3	2	4 cm	2

Using Eq. (4.6) and (4.7), we can calculate the ratio of volume of shear bands and collision material for each impact, V_s/V_c = 5.5x10^{-3}.

Figure 4.24 shows a schematic diagram of shear bands induced by plastic deformation. The thickness of each shear band has been determined to 10 nm [117, 125]. Schuh et al [79] plotted a figure of average shear band spacing as a function of specimen dimension for metallic glasses. The diameter of powder in this work is in the range of 10 to 70 μm. The corresponding shear band spacing is therefore in the range from 1 to 10 μm. Using these parameters, we estimated the theoretical ratio V^*_s/V^*_c, ~10^{-3}, which is high compared to the result of V_s/V_c= 5.5x10^{-3}. This result is in agreement with the shear band model we proposed in this work.

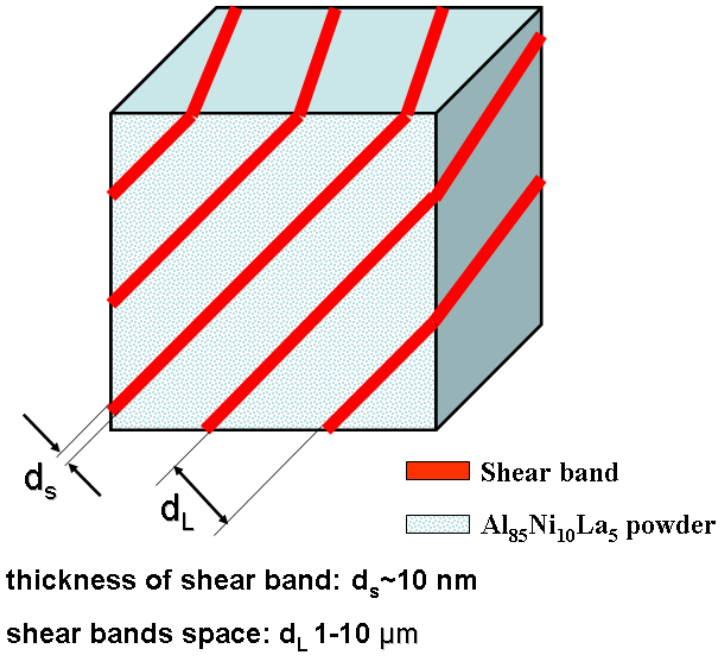

Figure 4.24: Schematic diagram of shear bands in ball-milled amorphous $Al_{85}Ni_{10}La_5$ powder.

5 Local Structure in Microalloyed Al-based Metallic Glasses

5.1 Results

5.1.1 Ni and Co edge on $Al_{86}TM_8RE_6$

The XRD patterns, see Figure 5.1, reveal broad diffuse intensity maxima at $2\theta \sim 38°$ confirming the amorphous structure of the alloys. The normalized Ni and Co XANES functions for the $Al_{86}Ni_6Co_2Y_{4.5}La_{1.5}$ alloy are shown in Figure 5.2 (a) and (b), respectively. These two signals were compared with the XANES spectra of pure metal foils of Ni and Co whose structures are well known. The XAFS spectra for each specimen and its reference foil were measured simultaneously to ensure accurate alignment of both edges. Figure 5.2 (a) and (b) reveal that the onsets of both edges of the XANES curves are shifted to lower energies compared with the onset of edge data of their respective standard reference. These shifts point to a charge transfer of electrons from neighbouring Al atoms of the first coordination shell to the Ni or Co atoms thus causing an increase in the electron density around both Ni and Co in the alloy splat.

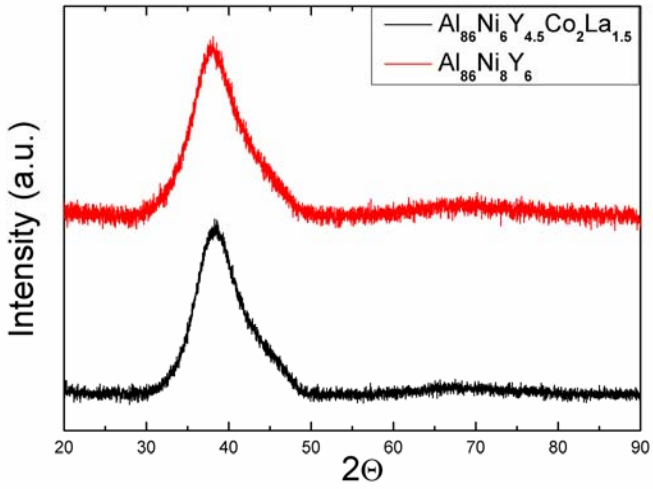

Figure 5.1: XRD pattern of $Al_{86}Ni_6Co_2Y_{4.5}La_{1.5}$ (bottom) and $Al_{86}Ni_8Y_6$ (top) splats in the as-quenched state measured with Cu-Kα radiation.

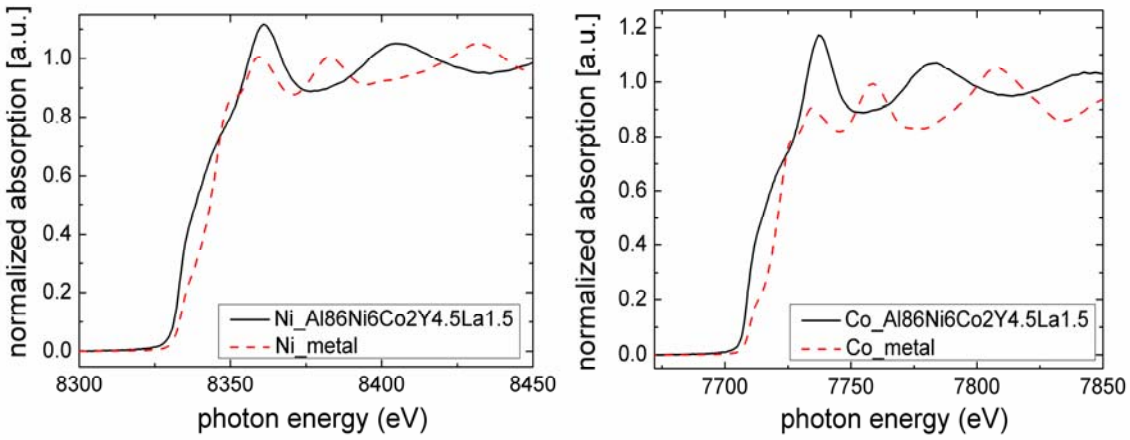

(a) (b)

Figure 5.2: Comparison of normalized Ni (a) and Co (b) K-edge XANES data for $Al_{86}Ni_6Co_2Y_{4.5}La_{1.5}$ BMG showing that the absorption edge for the alloy is shifted to lower energies compared to the pure element reference foil, indicating charge transfer from Al atoms of the first coordination sphere to Ni (a) and Co (b) atoms, respectively.

Figure 5.3 (a) shows the normalized EXAFS signal $\boldsymbol{k}^2 \cdot \chi(k)$ and Figure 5.3 (b) presents the Fourier transform of the $\boldsymbol{k}^2$-weighted EXAFS signal of $Al_{86}Ni_6Co_2Y_{4.5}La_{1.5}$ as a function of the radial distance R, measured at both the Ni- and Co-edges. For comparison, the $\boldsymbol{k}^2 \cdot \chi(k)$ and the FT measured at the Ni edge in $Al_{86}Ni_8Y_6$ are also given in Figure 5.3. The windows used

for FT in $k^2 \cdot \chi(k)$ is from 2.5 to 12 Å^{-1}. Three normalized spectra in (a) present similar oscillations and all three FT spectra in (b) have a similar qualitative appearance, too. The FT curves reveal a maximum near R = 2 Å. Above R = 2.5 Å, FT($k^2 \cdot \chi(k)$) does not reveal any distinct feature, indicating the absence of medium-range order.

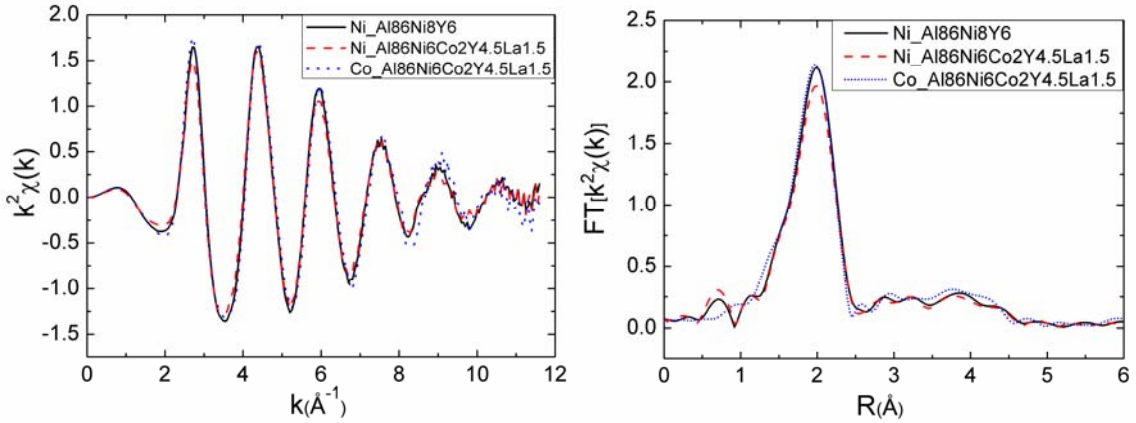

Figure 5.3: (a)Normalized EXAFS signal $k^2 \cdot \chi(k)$ and (b) Fourier transforms of the Ni and Co EXAFS functions of $Al_{86}Ni_6Co_2Y_{4.5}La_{1.5}$ and, for comparison, the Fourier transform of the Ni EXAFS function of $Al_{86}Ni_8Y_6$.

The Ni and Co EXAFS spectra and their Fourier-transforms along with the corresponding fits to the data are shown in Figure 5.4. The R-factors of all fits are less than 3.8 x 10^{-3} pointing to a good fit quality. The corresponding fit parameters are listed in Table 5.1. Within the experimental uncertainty, N, the distance $R_{TM\text{-}Al}$ of the Al nearest neighbours and σ^2, of both Co and Ni edge EXAFS are the same for the two alloys $Al_{86}Ni_6Co_2Y_{4.5}La_{1.5}$ and $Al_{86}Ni_8Y_6$. Therefore, the local structure around Ni and Co is concluded to be the same in $Al_{86}Ni_6Co_2Y_{4.5}La_{1.5}$. Moreover, the local structure around Ni in $Al_{86}Ni_6Co_2Y_{4.5}La_{1.5}$ and $Al_{86}Ni_8Y_6$ is the same. In other words, the partial substitution of Ni by Co does not change short-range-order around Ni in $Al_{86}Ni_8Y_6$. These similarities in structure are ascribed to the nearly identical atomic radii of Ni (r(Ni) = 1.24Å) and Co (r(Co) = 1.25Å) and to the similarity in their electronic structures reflected by similar electronegativities (1.91 for Ni and 1.88 for Co) and by similar negative mixing enthalpies with Al (ΔH_{mix}(Ni-Al) = –22 kJ/mol, ΔH_{mix}(Co-Al) = –19 kJ/mol [126]).

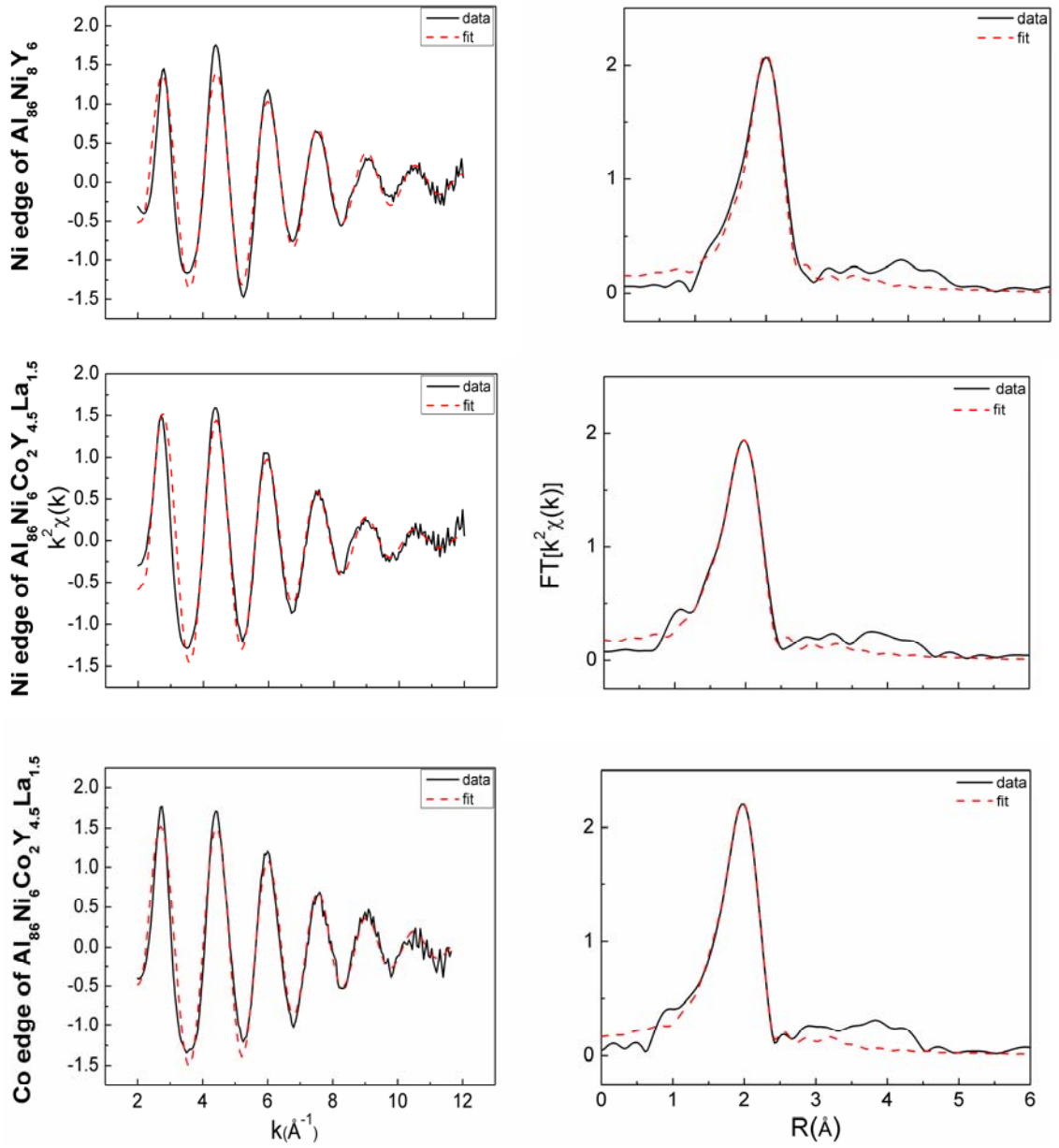

Figure 5.4: Normalized EXAFS signal k2·χ(k)(left) and Fourier Transform of the Ni EXAFS function (right) of $Al_{86}Ni_8Y_6$ (top) and both Ni and Co EXAFS functions of $Al_{86}Ni_6Co_2Y_{4.5}La_{1.5}$ (middle and bottom, respectively) along with fits to the data.

The bond lengths of the Al-Ni and Al-Co pairs, $\boldsymbol{R}_{\text{Ni-Al}}$ and $\boldsymbol{R}_{\text{Co-Al}}$, are appreciably smaller than the sum of the atomic radii $\boldsymbol{r}_{\text{Al}} + \boldsymbol{r}_{\text{Ni}}$ and $\boldsymbol{r}_{\text{Al}} + \boldsymbol{r}_{\text{Co}}$, see Table 5.1, reflecting bond-shortening due to s-p hybridization. Shortening of TM-Al bonds along with anomalously low coordination numbers has been observed in several amorphous Al-TM-RE alloys [26-32, 36] and has

been explained by the strong covalent character of these bonds: electrons with s-p character of Al are transferred to the d-states of the TM [28]. This interpretation in terms of charge transfer from Al atoms located in the first coordination shell around the TM atoms is supported by X-ray absorption near edge spectroscopy (XANES) of Ni and Co in $Al_{86}Ni_6Co_2Y_{4.5}La_{1.5}$, see Figure 5.2. The onset of the absorption edges are shifted to lower values compared to the data of the corresponding reference specimens. This shift in XANES data is ascribed to charge transfer from Al atoms to TM atoms[28], which is supposed to be the origin of the resulting covalent character of the bonds and the reduced bond lengths.

*Table 5.1: Parameters, obtained by fitting the one-shell model to the data. **N**: number of nearest neighbours; **R:*** phase-shift corrected *distance of nearest neighbours; σ^2: mean squared relative displacement of the effective interatomic distance. For comparison, the sum of the atomic radii of the absorbing atom and the aluminium atom, $R^* = r_{TM} + r_{Al}$ determined by the use of atomic radii listed in Ref [33], are listed.*

Alloy composition	Absorbing atom	*N*	R_{TM-Al} (Å)	*R** (Å)	σ^2 (Å^2)
$Al_{86}Ni_8Y_6$	Ni	6.3±0.2	2.45±0.01	2.68	0.0084±0.0007
$Al_{86}Ni_6Co_2Y_{4.5}La_{1.5}$	Ni	6.2±0.3	2.44±0.01	2.68	0.0093±0.0008
$Al_{86}Ni_6Co_2Y_{4.5}La_{1.5}$	Co	6.3±0.2	2.42±0.02	2.68	0.0083±0.0009

5.1.2 Substitution of Ni by Elements with Various Atomic Radii in an Al-based Amorphous Alloy

The elements used in this work for microalloying along with the atomic number Z, electro-negativity and atomic radii are shown in Table 5.2. When we compare the atomic radii, Ge, Ni and Co can be classified into one group of small elements, Al, Ag and Zr belong to a group of middle-size elements and Y and La are in the group of big elements. The aim of investigation of local structure of different elements in Al-transition metal (TM)-rare earth (RE) amorphous alloys is to investigate the influence of the atomic size and electron structure on local atomic arrangement.

$Ge_1Al_{86}Ni_7Y_6$, $Pd_1Al_{86}Ni_7Y_6$, $Ag_1Al_{86}Ni_7Y_6$ and $Zr_1Al_{86}Ni_7Y_6$ were measured on different edges by XAS in this work. Furthermore, the EXAFS experimental data of $Ag_1Al_{87}Ni_5La_7$ and $Zr_1Al_{87}Ni_5La_7$ measured by Wollgarten et al. at HASYLAB [127] were reanalysed in this chapter. Ge as a semiconductor was used to substitute Si, because the introduction of semiconducting elements can enhance GFA in Al-based metallic glasses [128], while Si cannot be detected by EXAFS due to its low edge energy. Ag and Pd were chosen due to their similar atomic radii which are close to that of Al. Furthermore, both elements (Ag and Pd) show strong metallic character. Finally, the mixing enthalpies with Al (ΔH_{mix}(Ag-Al) = –4 kJ/mol, ΔH_{mix}(Pd-Al) = –7 kJ/mol [126]) are similar and relatively low, which means the chemical properties of Ag and Pd are very similar to Al and similar to each other. The reason of using Zr is due to its great effect on glass formation of Al-based metallic glasses [8]. Furthermore, its chemical structure is close to Y while the atomic radius is between those of Al and Y.

Table 5.2: Atomic number, atomic radii and electronegativities of different elements used in the current work to plot atomic size distributions for a number of amorphous alloys.

Absorbing atom	Atomic No. Z	Pauling electronegativity	Atomic Radii (nm)	S_o^2
Ge	32	2.010	0.1240	0.9 [129]
Ni	28	1.910	0.1246	0.9 [129]
Co	27	1.880	0.1251	0.9 [129]
Pd	46	2.200	0.1375	0.84 [129]
Al	13	1.610	0.1432	---
Ag	47	1.930	0.1445	0.84 [129]
Zr	40	1.330	0.1603	0.9 [129]
Y	39	1.220	0.1802	0.9 [129]
La	57	1.100	0.1879	0.7 [109, 110]

The amount of these elements (Ge, Pd, Ag and Zr) used to substitute Ni in $Al_{86}Ni_8Y_6$ and $Al_{87}Ni_6La_7$, is based on a compromise of two considerations. One is the amount of these additional elements should be small to avoid significant changes in the main amorphous matrix. On the other hands, EXAFS experiments need a certain amount of additional elements to ob-

tain clear oscillation signals. Therefore, we choose 1 at% of additions (Ge, Pd, Ag and Zr) to substitute Ni in $Al_{86}Ni_8Y_6$ and $Al_{87}Ni_6La_7$ in this work.

S_o^2 was calculated by using the method introduce by Ref.[129]. Bowron et al. [110] and Anderson et al. [109] optimize the S_o^2 for the rare earth elements as 0.7. We use these values in the later fitting.

5.1.2.1 Local Structure of $Ge_1Al_{86}Ni_7Y_6$

The XRD pattern shown in Figure 5.5 indicates an amorphous structure of $Ge_1Al_{86}Ni_7Y_6$. The peak at $2\theta \approx 42°$ is assigned to the contamination of the splats with pure crystalline Cu of the piston in the splat quencher. The amorphous structure of the alloy is also reflected by the monotonous shape of the curves depicted in Figure 5.6 (a) and (c). A Hanning window between 3.3 and 10 $Å^{-1}$ was used in normalized $k^2 \cdot \chi(k)$ in Ge K-edge spectra and between 2.5 and 11$Å^{-1}$ in Y K-edge spectra of $Ge_1Al_{86}Ni_7Y_6$. Figure 5.6 (b) shows two intensity maxima at 2.2Å and 2.8Å in the Fourier-transformed Ge spectra, indicating two coordination shells. This spectrum is different from the Ni and La-spectra where only one peak was observed.

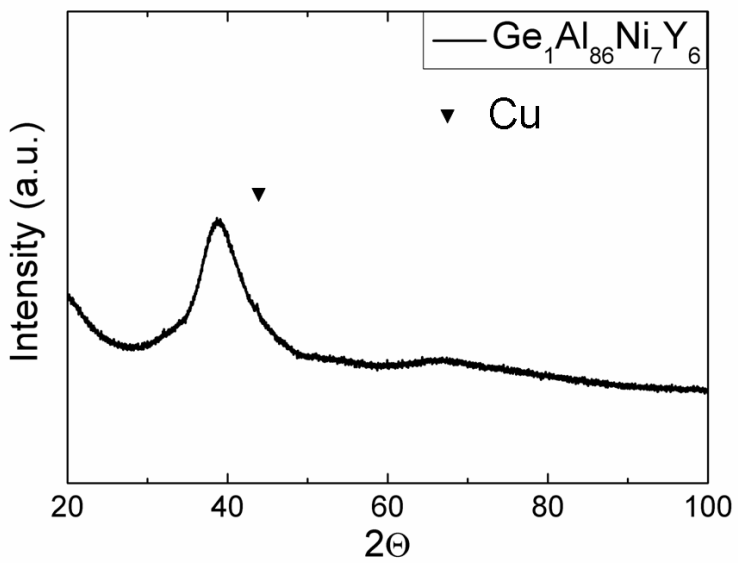

Figure 5.5: XRD pattern of $Ge_1Al_{86}Ni_7Y_6$ alloy. The peak at $2\theta = 44°$ is assigned to Cu contamination by the Cu piston of the splat quencher.

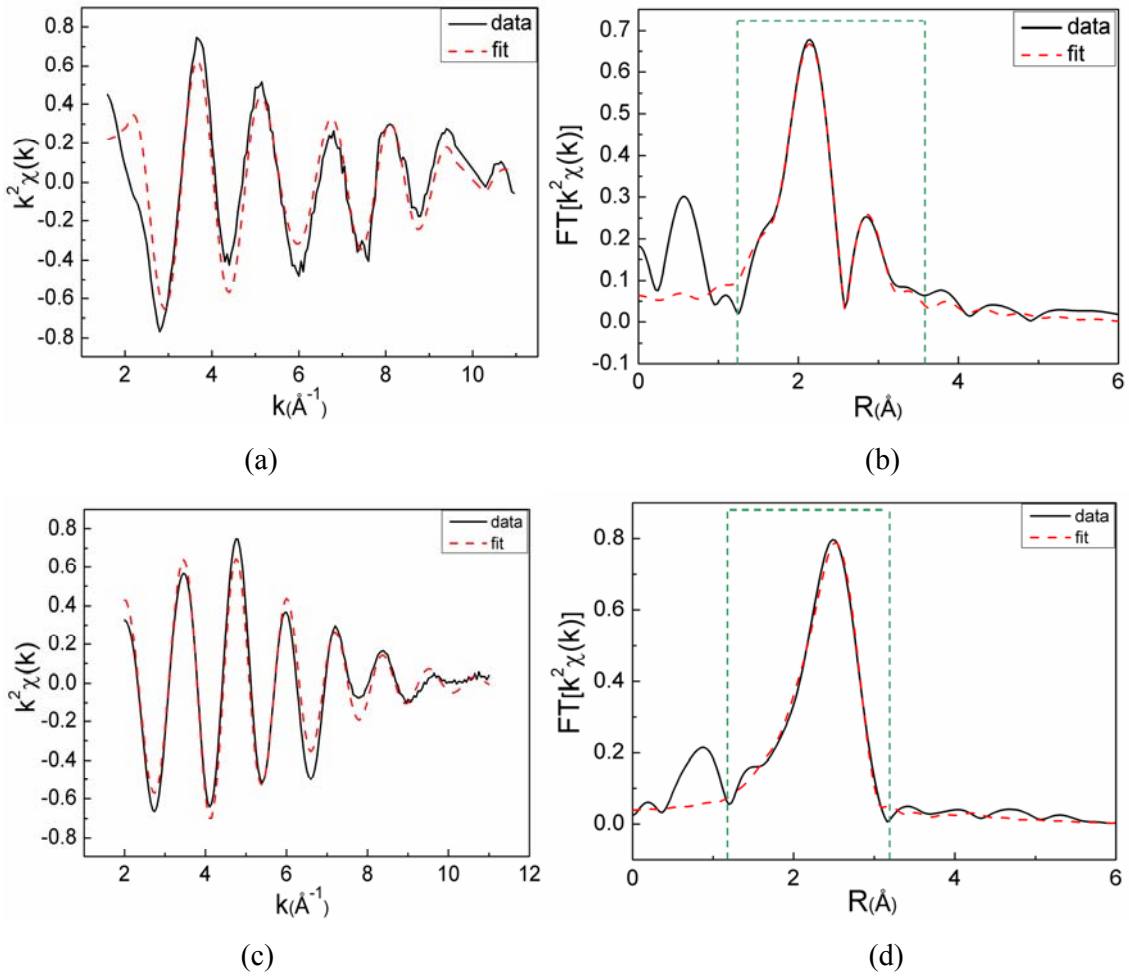

Figure 5.6: Normalized EXAFS spectra $k^2\chi(k)$*(a) and Fourier Transform (b) of the Ge K-edge EXAFS function of* $Ge_1Al_{86}Ni_7Y_6$ *along with fits to the data. (c) and (d) are normalized spectra and Fourier Transform of the Y K-edge data of* $Ge_1Al_{86}Ni_7Y_6$ *along with the fits to the data.*

The fit to the data was performed by using two shells with Aluminium atoms and a Hanning window from 1.2 to 3.5Å. The R-factor is 7.5 $\times 10^{-3}$ pointing to acceptable fit quality. The fitting parameters ***N(Ge)***, ***R(Ge)*** and σ^2***(Ge)*** are listed in Table 5.3. The average value of ***N(Ge)*** is 2.8 for the first coordination shell and 1.5 for the second shell. This two-peak shape in FT and relatively low numbers may due to the great effect of Ge on glass formation, which enhances the SRO from the first coordination shell to the second shell. This two-shell SRO is also observed in some Zr-based BMG with good GFA [69]. The distance ***R(Ge)*** of the Al nearest neighbour is about 2.62Å which is very close to the theoretical bond length ***R****. The theoretical bond length is calculated by $R^*=R_{AA}+R_{Al}$, where R_{AA} is the atomic radius of ab-

sorbing atoms and R_{Al} is the atomic radius of Al. $\sigma^2(Ge)$ is smaller than the corresponding values measured on Ni, Y, and La K-edge indicating that the local structure around Ge is less disordered. The Fourier-transformed Y K-edge spectrum along with the corresponding fits to the data are shown of Figure 5.6 (d). The $FT[k^2\chi(k)]$ shows a single peak at 2.5Å. The Hanning window was chosen from 1.2 to 3.2Å. The R-factor is 11 $\times 10^{-3}$ which is higher compared to the Ge K-edge but still acceptable. From Table 5.3, the ***N(Y)***, ***R(Y)*** and $\sigma^2(Y)$ values can be obtained as 8.9, 3.13Å and 0.014, respectively. ***N(Y)*** is in disagreement with Sadoc's [31] and Saksl's results [31, 130], who found that ***N*** is about 16 in Al-Y-Fe alloy. The reason for this discrepancy is not completely understood. One possibility might be the strong oxidizing property of Y. Though the splat quenching process is performed in Ar environment, the presence of minor amounts of O_2 in the Ar atmosphere cannot be completely excluded. If some O atoms arranges around Y, it should contribute to the intensity of the EXAFS signals on Y K-edge though the signal should be small compared to the contribution from the Al nearest neighbours and is expected to be at lower R-values in real space, see Figure 5.6 (d). Such contribution was not found in our data. Another reason for the low ***N(Y)*** may be due to a composition dependence of local structure of Y. The phase-shift corrected ***R(Y)*** value is similar to the theoretical bond length ***R****, thus pointing to small bond-shortening, only.

*Table 5.3: Parameters, **N, R**, and σ^2 obtained by fitting the two-shell model to the Ge K-edge data and a one shell model to the Y K-edge data. **N**: number of nearest neighbours; **R:** distance of nearest neighbours; σ^2: mean squared relative displacement of the effective interatomic distance. For comparison, the sum of the atomic radii of the absorbing atom and the aluminium atom, $R^* = r_{AA} + r_{Al}$ determined by the use of atomic radii listed in Ref [33], are listed.*

Alloy composition	Absorbing atom	N	R (Å)	R* (Å)	σ^2 (Å^2)
$Ge_1Al_{86}Ni_7Y_6$	Ge	1st shell: 2.8±0.3	2.62±0.01	2.67	0.007±0.001
		2nd shell:1.5±0.3	3.23±0.02		
$Ge_1Al_{86}Ni_7Y_6$	Y	8.9±0.5	3.13±0.01	3.23	0.014±0.001

5.1.2.2 Local Structure of $Pd_1Al_{86}Ni_7Y_6$

Figure 5.7 shows the XRD pattern of the as-atomized material revealing a broad maximum at $2\theta \approx 38°$, which gives evidence for the amorphous nature of $Pd_1Al_{86}Ni_7Y_6$ alloy.

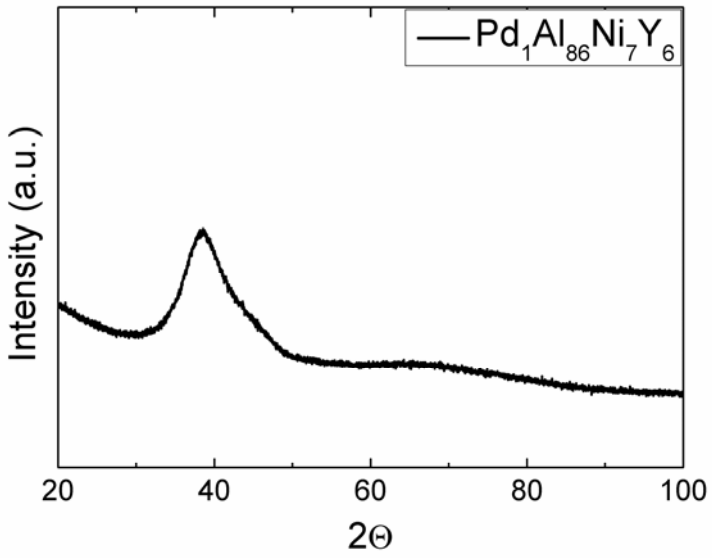

Figure 5.7: XRD pattern of $Pd_1Al_{86}Ni_7Y_6$ alloy

Normalized EXAFS spectra $\mathbf{k^2\chi}$(k) of Pd K-edge, Ni K-edge and Y K-edge of $Pd_1Al_{86}Ni_7Y_6$ alloy and the corresponding fits by single shell of Al atoms are shown in Figure 5.8 (a), (c) and (e), respectively. The quality of data of Pd and Y K-edge is good in the range from 2.5 to 10Å^{-1}, and becomes noisy at $\mathbf{k} > 11$ Å^{-1}. Therefore, we selected the Hanning window from 3.5 to 10.5 Å^{-1} for the Pd K-edge and from 2.5 to 10 Å^{-1} for the Y-edge. The normalized signal of the Ni K-edge is smooth from 2 to 12 Å^{-1}, so we have chosen a window between 2.5 and 12 Å^{-1}. The $FT[k^2\chi(k)]$ of the Pd, Ni and Y K-edge along with the fits to the data are shown in Figure 5.8 (b), (d), and (f), respectively. Single peaks were obtained from FTs of all edges. Peak positions of Pd, Ni, and Y K-edge are at 2.1 Å, 1.8 Å and 2.5Å, respectively, indicating that the distance ***R*** of nearest neighbours of Ni is smaller than Pd, and ***R*** of Y is longest. The windows of fitting are from 1.2 to 3.1 Å for the Pd K-edge, from 1.1 to 2.8 Å for the Ni K-edge and from 1.2 to 3.2Å for the Y K-edge, respectively. The R-factors of the fits to the Pd, Ni and Y data are $9.4\text{x}10^{-3}$, $1.6\ \text{x}10^{-3}$and $11\text{x}10^{-3}$, respectively, revealing acceptable fit quality.

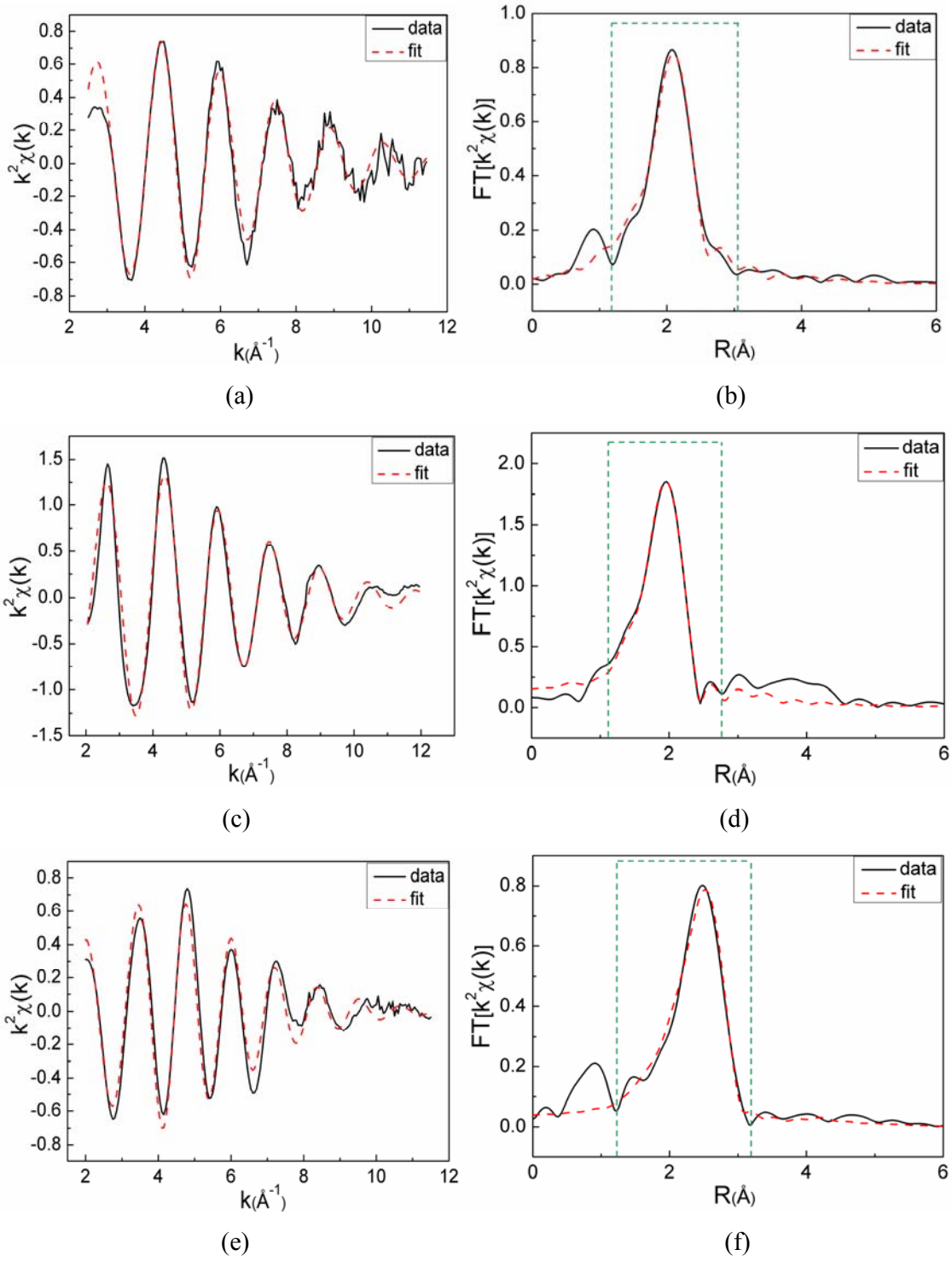

Figure 5.8：Normalized EXAFS spectra $\boldsymbol{k^2\chi}(k)$ *of the Pd, Ni, and Y K-edge of* $Pd_1Al_{86}Ni_7Y_6$ *along with fits to the data shown in (a), (c) and (e) respectively. (b), (d) and (f) are Fourier Transform of the Pd, Ni, Y K-edge EXAFS function of* $Pd_1Al_{86}Ni_7Y_6$ *along with fits to the data.*

The EXAFS fit parameters for Pd, Ni and Y are shown in Table 5.4. Due to the lower data quality of Pd and Y, the uncertainty in the number of nearest neighbours ***N*** of Pd and Y is bigger compared to Ni. ***N***(Pd) is 5.3 which is similar to ***N(Ni)***. ***N(Y)*** is 8.4 which is about the same as ***N(Y)*** in $Ge_1Al_{86}Ni_7Y_6$. The distance ***R*** to the Al nearest neighbours of Pd and Ni is 7% and 9%, respectively, which is shorter than the theoretical distance ***R****, while ***R(Y)*** shows only 3% of shortening. The mean squared relative displacement of the effective interatomic distance σ^2 of Y K-edge of $Pd_1Al_{86}Ni_7Y_6$ is the same as for $Ge_1Al_{86}Ni_7Y_6$ and higher than σ^2 of Pd and Ni due to the bigger size of Y which makes more mismatch at local environment. As the values of ***N*** and σ^2 for Pd and Ni are the same, one can conclude that these two elements have the same local order.

*Table 5.4: Parameters, obtained by using a one shell model to fit the Pd, Ni and Y K-edge data. **N**: number of nearest neighbours; **R:** distance of nearest neighbours; σ^2: mean squared relative displacement of the effective interatomic distance. For comparison, the sum of the atomic radii of the absorbing atom and the aluminium atom, $R^* = r_{AA} + r_{Al}$ determined by the use of atomic radii listed in Ref [33], are listed.*

Alloy composition	Absorbing atom	*N*	*R* (Å)	*R** (Å)	σ^2 (Å^2)
$Pd_1Al_{86}Ni_7Y_6$	Pd	5.3±0.5	2.61±0.01	2.81	0.008±0.002
$Pd_1Al_{86}Ni_7Y_6$	Ni	5.8±0.3	2.43±0.01	2.68	0.009±0.001
$Pd_1Al_{86}Ni_7Y_6$	Y	8.4±0.5	3.12±0.01	3.23	0.013±0.001

5.1.2.3 Local Structure of $Ag_1Al_{86}Ni_7Y_6$ and $Ag_1Al_{87}Ni_5La_7$

The XRD pattern of $Ag_1Al_{86}Ni_7Y_6$ is shown in Figure 5.9. It shows a broad maximum at $2\theta \approx 39°$ which is a typical XRD pattern of Al-based amorphous alloys. A fully amorphous $Ag_1Al_{87}Ni_5La_7$ alloy was prepared and measured by Wollgarten et al. [127] and we reanalysed the EXAFS data in this work.

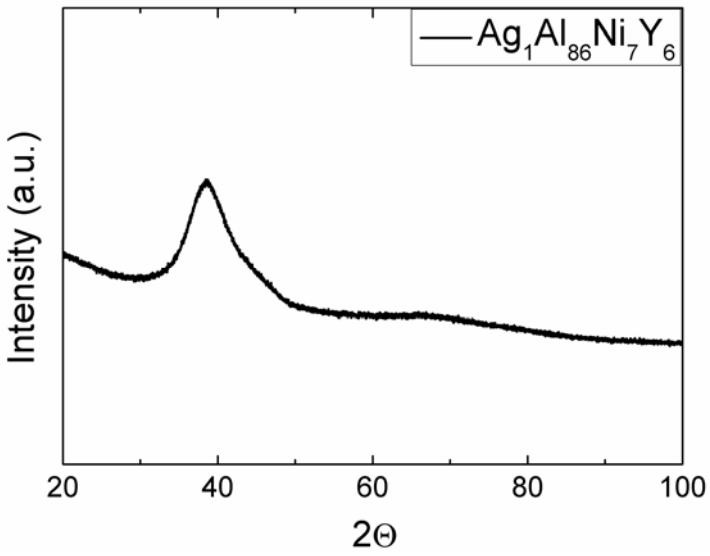

Figure 5.9: XRD pattern of $Ag_1Al_{86}Ni_7Y_6$ in the as-quenched condition.

The EXAFS spectra of $Ag_1Al_{86}Ni_7Y_6$ were measured in the transmission mode at BAMline, and the raw data of $Ag_1Al_{87}Ni_5La_7$ were obtained from measurements in the fluoresce mode at HASYLAB. The normalized EXAFS spectra $k^2 \cdot \chi(k)$ (solid line) after removing the back-ground and the corresponding fit data (dashed line) of $Ag_1Al_{86}Ni_7Y_6$ and $Ag_1Al_{87}Ni_5La_7$ of Ag and Ni K-edge are shown in Figure 5.10 (a), and (c) respectively. The FT (solid line) and the fitting results (dashed line) of $Ag_1Al_{86}Ni_7Y_6$ and $Ag_1Al_{87}Ni_5La_7$ of Ag and Ni K-edge are shown in Figure 5.10 (b) and (d), respectively. The normalized spectra obtained for the Ag and Ni edge are nearly identical for the $Ag_1Al_{86}Ni_7Y_6$ and $Ag_1Al_{87}Ni_5La_7$. Therefore, these two compositions have no change of the local order around the Ag and Ni atoms. However, the FT for the Ag K-edge of $Ag_1Al_{87}Ni_5La_7$ has a higher intensity than for $Ag_1Al_{86}Ni_7Y_6$ which may indicate a higher number of nearest neighbours around Ag in $Ag_1Al_{87}Ni_5La_7$ than in $Ag_1Al_{86}Ni_7Y_6$. The Hanning windows in FT spectra are from 1.1 to 3.1Å for the Ag-edge and from 1.1 to 2.8Å for the Ni-edge. The fits to the data of $\mathbf{k^2 \cdot \chi}(k)$ and $FT[k^2\chi(k)]$ look fairly good, which can be proved by the low R-factor of 8 $\times 10^{-3}$ for Ag-edge and of 1.3 $\times 10^{-3}$ for the Ni-edge.

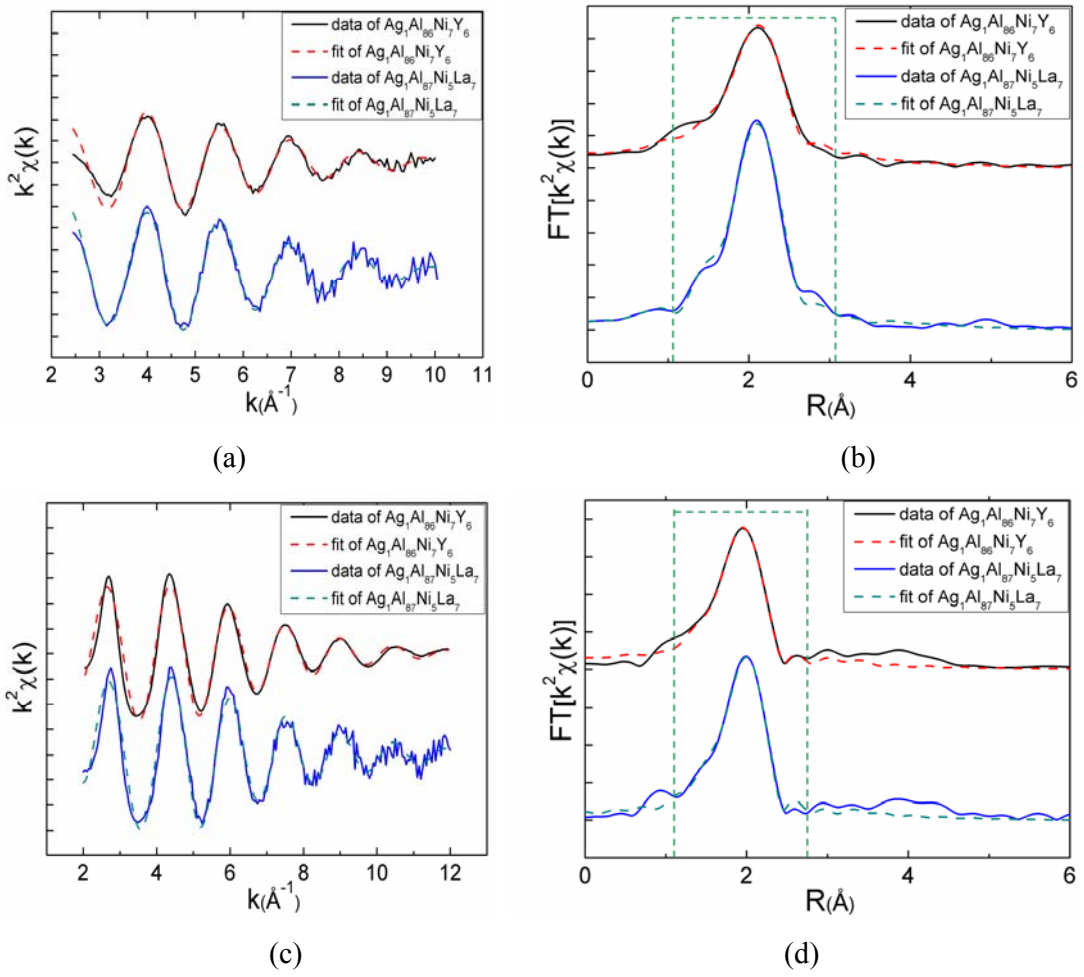

Figure 5.10: Normalized EXAFS signal of $\mathbf{k^2 \cdot \chi}$*(k) of Ag K-edge(a) and Ni K-edge (c) of* $Ag_1Al_{86}Ni_7Y_6$ *and* $Ag_1Al_{87}Ni_5La_7$ *alloys. Fourier Transform of the Ag K-edge (b) and Ni K-edge (d) of* $Ag_1Al_{86}Ni_7Y_6$ *and* $Ag_1Al_{87}Ni_5La_7$ *alloys.*

The normalized Y K-edge EXAFS spectra and the FTs of $Ag_1Al_{86}Ni_7Y_6$ are shown in Figure 5.11 (a) and (b), respectively. The window in $\mathbf{k^2 \cdot \chi}$(k) is selected between 2.5 and 10.5Å^{-1} , and the window in the FT spectra is from 1.2 to 3.2Å. The peak between 0 and 1.2Å is considered as the background noise, because it is impossible to get any information for the local structure within such small distance. The fitting quality is good as indicated by the R-factor of 11 x10^{-3}. Figure 5.11 (c) and (d) present the normalized EXAFS spectra and FTs of La K-edge of $Ag_1Al_{87}Ni_5La_7$, respectively. A Hanning window between 2.5 and 10 Å^{-1} was used in the normalized EXAFS signal, and a window for fitting from 1.5 to 3.3 Å in the ***R***-space as shown in Figure 5.11 (d). The R-factor of 36 x10^{-3} reflects the poor quality of the raw data.

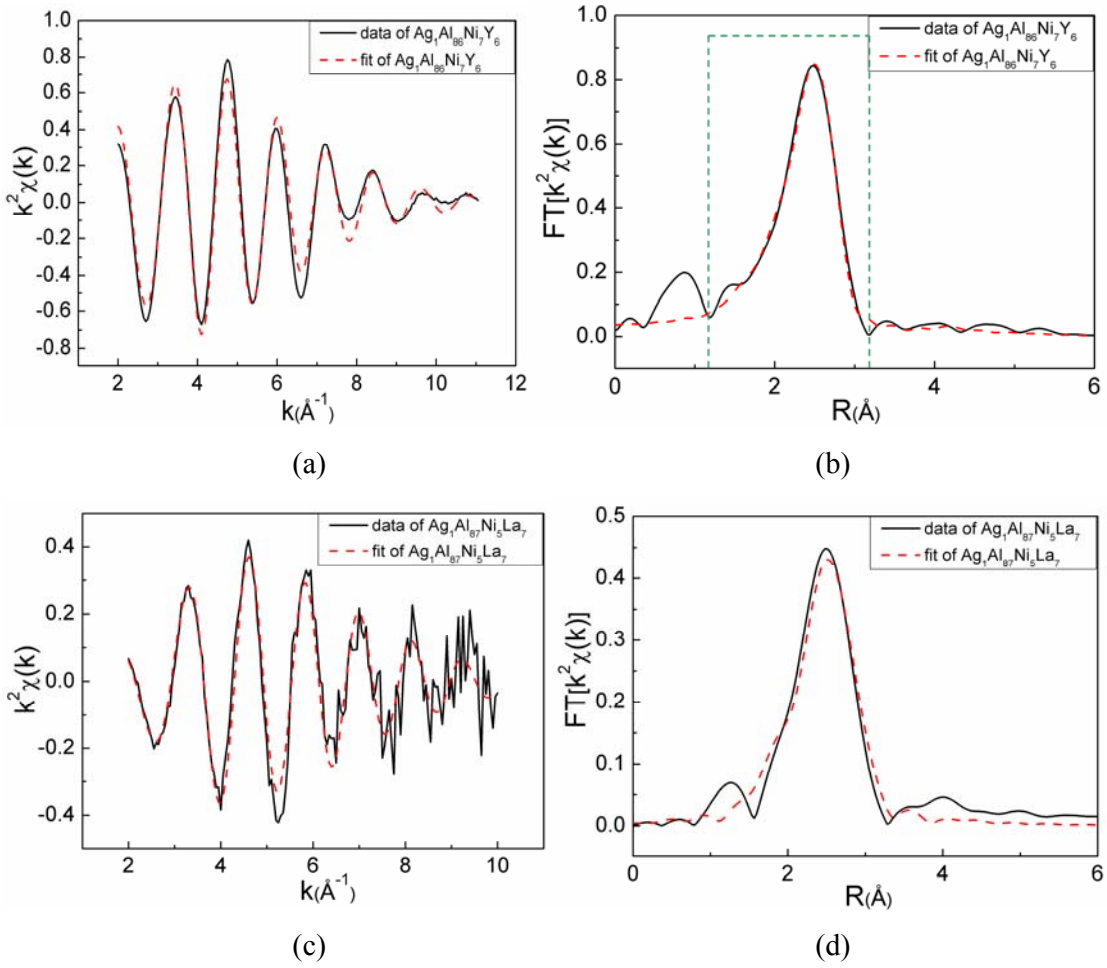

Figure 5.11: Normalized EXAFS signal $k^2 \cdot \chi(k)$ of Y K-edge(a) of $Ag_1Al_{86}Ni_7Y_6$ and La K-edge(c) of $Ag_1Al_{87}Ni_5La_7$ alloys. Fourier transform of the Y K-edge (b) of $Ag_1Al_{86}Ni_7Y_6$ and La K-edge (d) of $Ag_1Al_{87}Ni_5La_7$ alloys.

The parameters of fitting are shown in Table 5.5. Although the intensity of the peak of the Fourier transform, see Figure 5.10 (b), between the two alloys is different, the number ***N*** of nearest neighbours of Ag is the same, considering the fitting uncertainty. The ***R(Ag)*** ~2.66Å are the same in both alloys, which is much shorter than the theoretical distance ***R****. Furthermore, σ^2 is also the same for the two alloys indicating that the small difference in composition between the two alloys does not change the local order around Ag atoms. Similar values of ***N***, ***R*** and σ^2 are also observed for the fitting results of the Ni K-edge spectra. The ***R(Ni)*** values of both alloys are appreciably smaller than ***R****. Considering the Y K-edge of $Ag_1Al_{86}Ni_7Y_6$ alloy, the ***N(Y)*** value is similar to which of $Ge_1Al_{86}Ni_7Y_6$ and $Pd_1Al_{86}Ni_7Y_6$ in this work, but shows a big difference to the results reported by Sadoc et al. [31] and Saksl et al.[130]. Possible

scavenging of oxidation by Y may be the reason for the lower ***N(Y)***. The ***R*** value of Y is only slightly smaller than ***R**** compared with the shortening of ***R*** of Ag and Ni K-edge. The coordination number of La K-edge of $Ag_1Al_{87}Ni_5La_7$ is about 18.5 which is the same as the value of ***N*** of $Al_{85}Ni_{10}La_5$ as-atomized powder. Within the experimental uncertainty, this number is in agreement with the work of Saksl et al. [32]. The ***R*** value is in agreement with ***R****.

*Table 5.5: Parameters, obtained by fitting the one shell model to the Ag, Ni, Y, La K-edge data. **N**: number of nearest neighbours; **R:** distance of nearest neighbours; σ^2: mean squared relative displacement of the effective interatomic distance. For comparison, the sum of the atomic radii of the absorbing atom and the aluminium atom, $R^* = r_{AA} + r_{Al}$ determined by the use of atomic radii listed in Ref [33], are listed.*

Alloy composition	Absorbing atom	*N*	*R* (Å)	*R** (Å)	σ^2 (Å^2)
$Ag_1Al_{86}Ni_7Y_6$	Ag	4.5±0.5	2.66±0.01	2.88	0.013±0.002
$Ag_1Al_{87}Ni_5La_7$	Ag	5.1±0.4	2.67±0.01	2.88	0.012±0.002
$Ag_1Al_{86}Ni_7Y_6$	Ni	6.1±0.3	2.44±0.01	2.68	0.009±0.001
$Ag_1Al_{87}Ni_5La_7$	Ni	6.2±0.3	2.44±0.01	2.68	0.007±0.001
$Ag_1Al_{86}Ni_7Y_6$	Y	9.0±0.5	3.15±0.02	3.23	0.013±0.001
$Ag_1Al_{87}Ni_5La_7$	La	18.5±1.8	3.32±0.01	3.31	0.013±0.002

5.1.2.4 Local Structure of $Zr_1Al_{86}Ni_7Y_6$ and $Zr_1Al_{87}Ni_5La_7$

Figure 5.12 shows the XRD pattern of $Zr_1Al_{86}Ni_7Y_6$ alloy which exhibits the diffuse scattering typical for metallic glasses with a maximum at $2\theta=39°$. Amorphous $Zr_1Al_{87}Ni_5La_7$ alloy with small amount of crystals was prepared and measured by Wollgarten et al. [127] and we reanalysed the EXAFS data in this work.

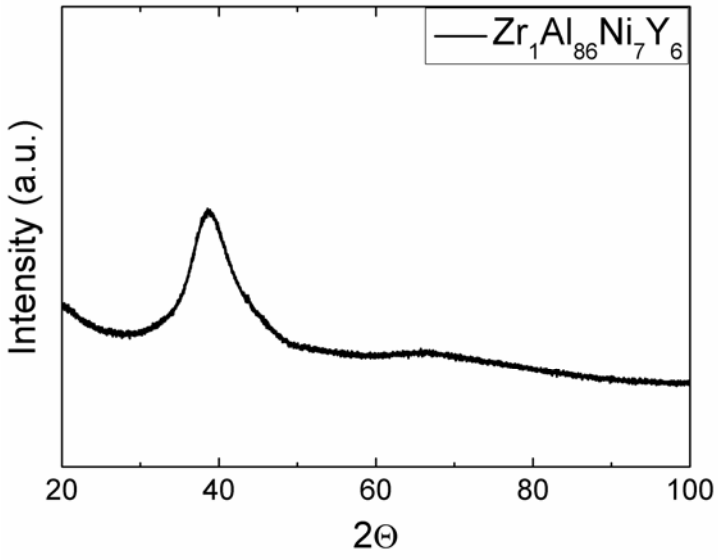

Figure 5.12: XRD pattern of $Zr_1Al_{86}Ni_7Y_6$ alloy in the as-quenched condition.

Figure 5.13 (a) and (b) show the absolute value of the k^2-weighted Zr-EXAFS signals and the corresponding Fourier transforms, respectively. The calculated single-shell fits (dashed line) are also shown in Figure 5.13 (a) and (b). The normalized Zr-EXAFS spectra of $Zr_1Al_{86}Ni_7Y_6$ and $Zr_1Al_{87}Ni_5La_7$ alloys show a small difference above 6Å^{-1}. The FT spectra show a maximum with a similar shape and similar intensity. However, the maximum of the FT of $Zr_1Al_{87}Ni_5La_7$ is shifted to a higher value compared with $Zr_1Al_{86}Ni_7Y_6$. This shift indicates that the distance of nearest neighbours increases from $Zr_1Al_{86}Ni_7Y_6$ to $Zr_1Al_{87}Ni_5La_7$. The normalized and k^2-weighted Ni-EXAFS data with the corresponding fit of $Zr_1Al_{86}Ni_7Y_6$ and $Zr_1Al_{87}Ni_5La_7$ alloys are shown in Figure 5.13 (c) and the FT signals with the corresponding fits are shown in Figure 5.13 (d). In both figures, the experimental data of $Zr_1Al_{86}Ni_7Y_6$ and $Zr_1Al_{87}Ni_5La_7$ have qualitatively the same shape of oscillation which reveals the same local structure around Ni atoms. The R-factor is 6×10^{-3} of fitting of Zr K-edge and 1.6×10^{-3} of fitting of Ni K-edge indicating good quality of the fits in both cases.

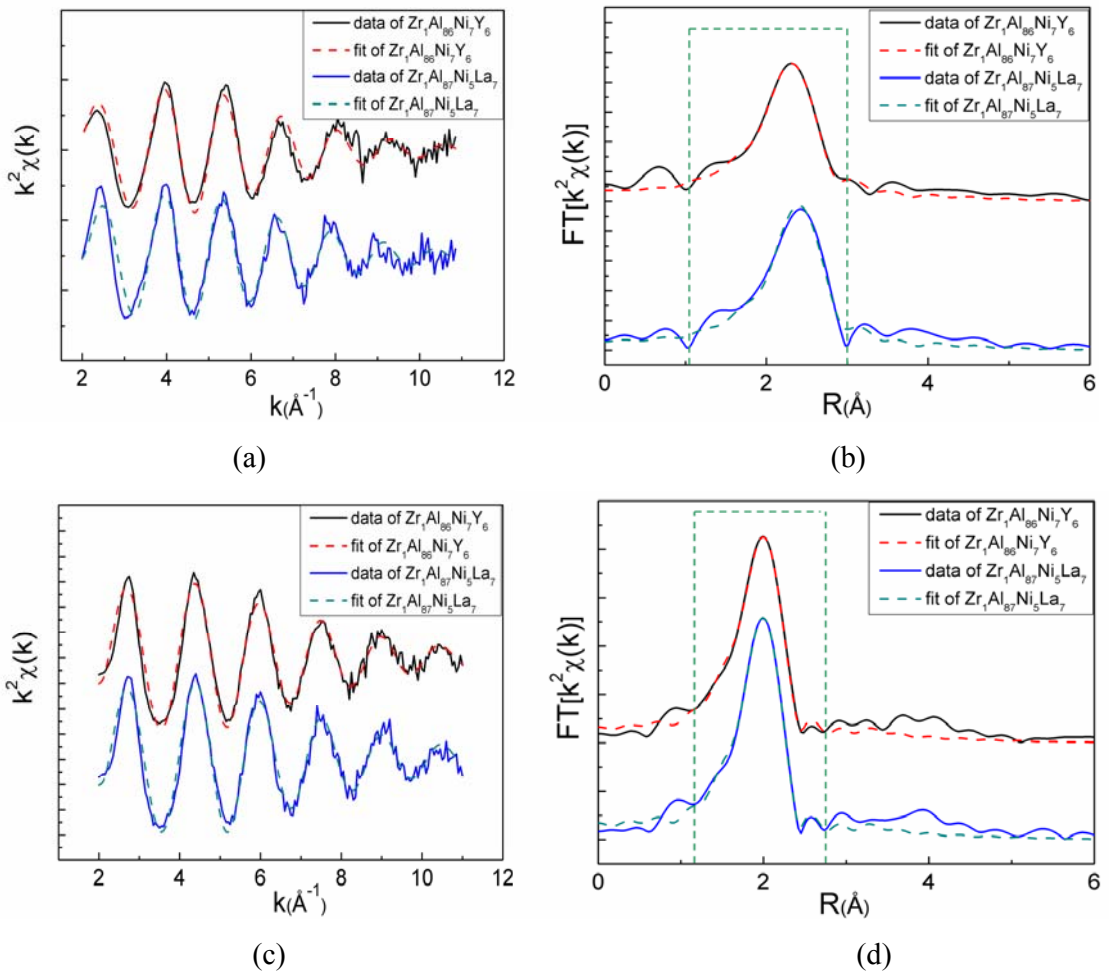

Figure 5.13: (a) and (c) Comparison of normalized and calculated one-shell fits obtained from $Zr_1Al_{86}Ni_7Y_6$ and $Zr_1Al_{87}Ni_5La_7$ alloys above Zr K-edge and Ni K-edge, respectively. (b) and (d) Comparison of Fourier transforms of experimental $\boldsymbol{k^2\cdot\chi(k)}$ signals and fitted data of Zr K-edge and Ni K-edge, respectively.

In Figure 5.14 (a) and (b), the solid lines represent the $\boldsymbol{k^2}$-weighted Y-EXAFS signals and their Fourier transforms, respectively, of $Zr_1Al_{86}Ni_7Y_6$. The dashed lines are the corresponding single-shell fits. Figure 5.14 (c) shows the normalized and $\boldsymbol{k^2}$-weighted La K-edge EXAFS signal with single-shell fit of $Zr_1Al_{87}Ni_5La_7$ alloy and (d) shows the Fourier transforms of experimental $\boldsymbol{k^2\cdot\chi(k)}$ signals and fitted data of La K-edge. The windows of fitting are shown in Figure 5.14 (b) and (d). The R-factor of fitting of Y K-edge is 11 $\times 10^{-3}$ and of La K-edge is 36 $\times 10^{-3}$ which is not very good, because of the moderate quality of the raw data.

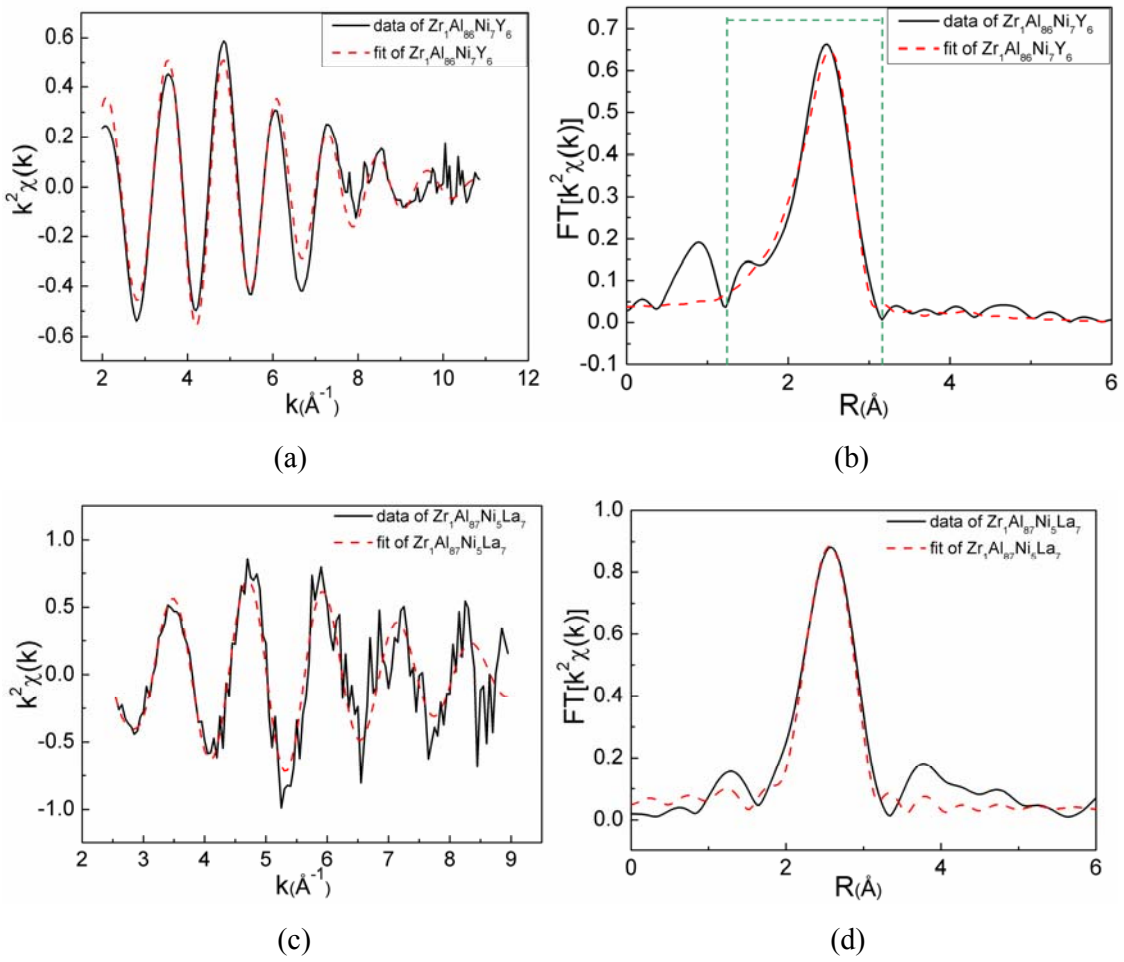

Figure 5.14:) Comparison of normalized spectra and calculated single-shell fits obtained from $Zr_1Al_{86}Ni_7Y_6$ above Y K-edge (a) and $Zr_1Al_{87}Ni_5La_7$ alloys above La K-edge (c) respectively. Comparison of Fourier transforms of experimental $\boldsymbol{k^2 \cdot \chi(k)}$ signals and fitted data of Y K-edge (b) and La K-edge (d), respectively.

The parameters of fitting are shown in Table 5.6. The number ***N*** of nearest neighbours of Zr atoms is about the same (~8.5) for both $Zr_1Al_{86}Ni_7Y_6$ and $Zr_1Al_{87}Ni_5La_7$ alloys. The distance ***R*** of nearest neighbours of Zr in $Zr_1Al_{87}Ni_5La_7$ is 2.91Å which is 0.06Å longer than in $Zr_1Al_{86}Ni_7Y_6$. This indicates that the distance of nearest neighbours around Zr in $Zr_1Al_{87}Ni_5La_7$ is slightly larger compared to $Zr_1Al_{86}Ni_7Y_6$, while $\boldsymbol{\sigma^2(Zr)}$ is the same for both alloys. Hence, apart from slightly different ***R*** values the local order of Zr in $Zr_1Al_{86}Ni_7Y_6$ reveals no significant change compared with $Zr_1Al_{87}Ni_5La_7$. All three fit parameters for the Ni edge are the same indicating that the atomic arrangement around Ni shows no change with a minor change of composition. The ***R(Ni)*** value is 9% shorter than the theoretical distance ***R****

which is the same as for other results on the Ni K-edge of similar composition, for instance, $Al_{85}Ni_{10}La_5$, $Al_{86}Ni_8Y_6$, etc. ***N(Y)*** is small compared with other values of N(Y) of various compositions studied in this work. The reasons for the small value of Y are not clear. It may be caused by a strong oxidation of Y in the process of sample production. Moreover, ***R*** and σ^2 are the same as for $Ge_1Al_{86}Ni_7Y_6$, $Pd_1Al_{86}Ni_7Y_6$ and $Ag_1Al_{86}Ni_7Y_6$. Considering the La K-edge, ***N***, ***R*** and σ^2 in $Zr_1Al_{87}Ni_5La_7$ have no significant difference compared with $Al_{85}Ni_{10}La_5$.

*Table 5.6: Parameters, obtained by fitting a single-shell model to the Zr, Ni, Y, La K-edge data. **N**: number of nearest neighbours; **R:** distance of nearest neighbours; σ^2: mean squared relative displacement of the effective interatomic distance. For comparison, the sum of the atomic radii of the absorbing atom and the aluminium atom, $R^* = r_{AA} + r_{Al}$ determined by the use of atomic radii listed in Ref [33], are listed.*

	Absorbing atom	*N*	*R* (Å)	*R** (Å)	σ^2 (Å^2)
$Zr_1Al_{86}Ni_7Y_6$	Zr	8.5±1.0	2.85±0.01	3.04	0.011±0.002
$Zr_1Al_{87}Ni_5La_7$	Zr	8.4±1.1	2.91±0.02	3.04	0.011±0.002
$Zr_1Al_{86}Ni_7Y_6$	Ni	6.0±0.2	2.44±0.01	2.68	0.007±0.001
$Zr_1Al_{87}Ni_5La_7$	Ni	6.0±0.2	2.44±0.01	2.68	0.006±0.001
$Zr_1Al_{86}Ni_7Y_6$	Y	6.5±0.5	3.12±0.01	3.23	0.013±0.001
$Zr_1Al_{87}Ni_5La_7$	La	19.3±2.5	3.31±0.02	3.31	0.014±0.003

5.2 Discussion

5.2.1 Site Substitution of Ni by Co in Amorphous $Al_{85}Ni_6Co_2Y_{4.5}La_{1.5}$ Alloy

Due to the empirical rule named "confusion principle" [8, 131, 132], the stabilization of a amorphous alloy can be increased by adding more components. The amorphous $Al_{85}Ni_6Co_2Y_{4.5}La_{1.5}$ alloy was first report by Yang et al. [24], who substituted Ni by Co and Y by La in $Al_{86}Ni_8Y_6$ alloy to obtain a better GFA. (Fully glassy rods of $Al_{85}Ni_6Co_2Y_{4.5}La_{1.5}$ alloy with 1 mm diameter could be successfully produced by mould casting.) Our EXAFS

fitting results revealed the same atomic environment around Ni and Co with 6 neighbouring Al atoms which suggests the occupation of the centre of Al octahedra by Ni and Co atoms. The distance $R_{TM\text{-}Al}$ of the Al nearest neighbours and the mean squared relative displacement of the effective interatomic distance, σ^2, of Co- and Ni-EXAFS in $Al_{85}Ni_6Co_2Y_{4.5}La_{1.5}$ and $Al_{86}Ni_8Y_6$ are the same within the experimental uncertainty. Therefore, the partial substitution of Ni by Co does not change the short-range-order (SRO) around Ni from $Al_{86}Ni_8Y_6$ to $Al_{85}Ni_6Co_2Y_{4.5}La_{1.5}$. These similarities mean that element substitution of Ni by Co can be regarded as a site substitution in the local structure, see Figure 5.15.

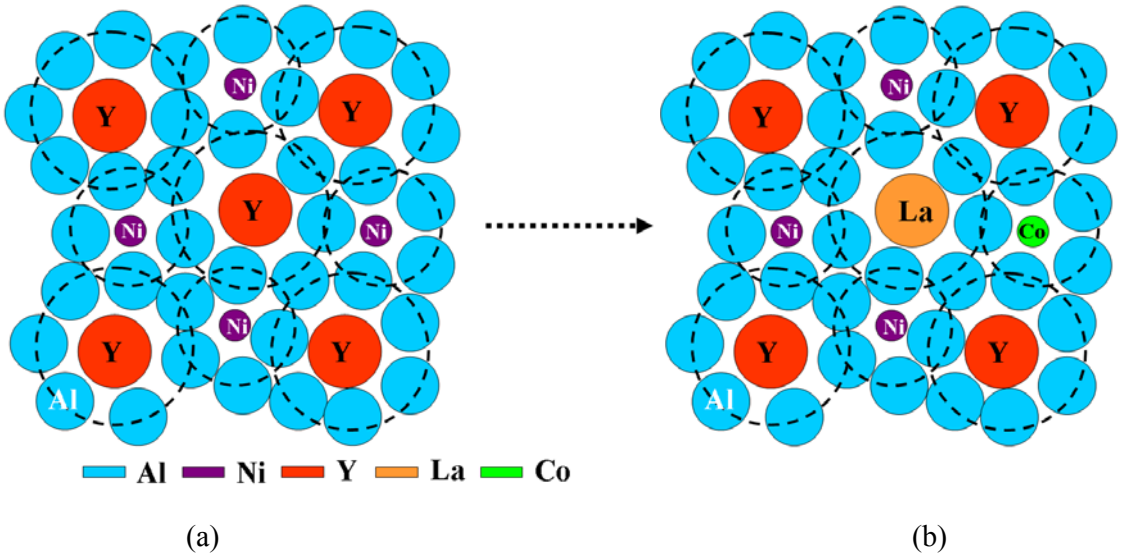

Figure 5.15: Schematical representation of $Al_{86}Ni_8Y_6$ (a) and $Al_{85}Ni_6Co_2Y_{4.5}La_{1.5}$ (b) in two dimensions according to Miracle's structural model [71]

Figure 5.15 shows a two-dimensional structural model to represent the atomic arrangement of $Al_{86}Ni_8Y_6$ (a) and $Al_{85}Ni_6Co_2Y_{4.5}La_{1.5}$ (b) accroding to Miracle [71]. The solvent Al atoms and the bigger solute atoms Y form a primary cluster, while the smaller solute atoms Ni stay at the octahedral site of 6 Al atoms and each Al atom consisted by a Y-Al cluster. The Ni atoms thus can be considered as "glue atoms" which due to their strong covalent bonds with the Al atoms act as a kind of paste media to connect primary clusters in $Al_{86}Ni_8Y_6$ alloy. After substitution of Ni by Co and of Y by La, the Co atoms go to the same position of octahedral site surrounded by Al as Ni atoms, because of the similar atomic size and nearly identical electronic structures reflected by similar electronegativities (1.91 for Ni and 1.88 for Co) and

similar negative mixing enthalpies with Al (ΔH_{mix}(Ni-Al) = –22 kJ/mol, ΔH_{mix}(Co-Al) = –19 kJ/mol[126]). La atoms are also predicted to go to the same position as Y. This experiment will be done in a future work.

5.2.2 Glass-Forming-Ability Improvement by Increasing the Mixing Entropy

The idea of improvement of GFA by increase in entropy via substitution of elements with similar size and similar valence electronic structures [133] has been applied to a variety of alloy systems, e.g., Zr-Ti-Ni-Cu-Be [47], Zr-Ni-Cu-Al [134], Pd-Cu-Ni-P [135], $(La_{0.5}Ce_{0.5})_{65}Al_{10}(Co_{0.6}Cu_{0.4})_{25}$ [136], $(La_{0.5}Ce_{0.5})_{65}Al_{10}Co_{25}$ [133] and $Al_{86}Ni_6Co_2Y_{4.5}La_{1.5}$ [23, 24] bulk metallic glasses (BMGs). Li et al. [133] assigned the improvement of GFA of La-based amorphous alloys by substitution of elements with similar size and similar valence electronic structures to an increase in entropy. To explain this view, we evaluated the mixing Gibbs free energy (ΔG) in $Al_{86}Ni_8Y_6$ and $Al_{85}Ni_6Co_2Y_{4.5}La_{1.5}$.

From a thermodynamic point of view, the difference in energy between the liquid and the solid state, $G^l - G^s$, generally reflects the stability of the glassy state. However, it is impossible to estimate the energies accurately as a function of composition and temperature for multi-component systems. Since $G^l - G^s$ is assumed to be proportional to the free energy of mixing ΔG in the liquid state [133, 137], we use ΔG to understand the influence of substitution on GFA.

When pure elements are in a standard state, ΔG is defined by its enthalpy of mixing ΔH, the entropy of mixing ΔS and the temperature T:

$$\Delta G = \Delta H - T\Delta S \tag{5.1}$$

In our calculation, we choose T of 1050 K, which is slightly above the melting temperature of both alloys. Considering that the partial substitution of Ni by Co did not change the local structure, one can imagine that the La atoms sit on positions that have previously been occupied by the substituted Y atoms in the glassy structure. This means, the coordination number and the kinds of neighbouring elements are not significantly changed. In the present study, ΔS

is equal to the sum of the configurational entropy (ΔS_{conf}) and the mismatch entropy (ΔS_{mis}), resulting from atomic size mismatch:

$$\Delta S = \Delta S_{conf} + \Delta S_{mis} \tag{5.2}$$

In the ideal multicomponent solid solution containing Z elements, ΔH and ΔS_{conf} are defined as:

$$\Delta H = \sum_{i=1, i\neq j}^{Z} \Omega_{ij} c_i c_j \tag{5.3}$$

$$\Delta S_{conf} = -R_{conf} \sum_{i=1}^{Z} (c_i \ln c_i) \tag{5.4}$$

Where Ω_{ij} is the regular solution interaction parameter between i and j elements, R_{conf} is the gas constant, c_i and c_j are the mole concentration for element i and j respectively. Takeuchi and Inoue [138] simplified ΔH by using Miedema's macroscopic model for binary liquid alloys. In the calculation, the mixing enthalpy ΔH_{AB}^{mix} was substituted for Ω_{ij} with the equation:

$$\Omega_{ij} = 4 \times \Delta H_{AB}^{mix} \tag{5.5}$$

The coefficient four is defined in Eq. (5.3) at equiatomic composition in a binary system [139].

The equation to calculate ΔS_{mis} is given as:

$$\Delta S_{mis} = k_B \left[\frac{3}{2}(\varsigma^2 - 1) y_1 + \frac{3}{2}(\varsigma - 1)^2 y_2 - \left\{ \frac{1}{2}(\varsigma - 1)(\varsigma - 3) + \ln \varsigma \right\} (1 - y_3) \right], \tag{5.6}$$

where k_B is the Boltzmann constant, ς is a parameter being defined as $\varsigma = 1/(1-\xi)$, where ξ is a packing fraction which is fixed to be 0.64 in this work according to the dense random packing model [140]. y_1, y_2 and y_3 are parameters following the relation of $y_1 + y_2 + y_3 = 1$, and are defended as:

$$y_1 = \frac{1}{\sigma^3} \sum_{j>i=1}^{n} (d_i + d_j)(d_i - d_j)^2 c_i c_j \tag{5.7}$$

$$y_2 = \frac{\sigma^2}{(\sigma^3)^2} \sum_{j>i=1}^{n} d_i d_j (d_i - d_j)^2 c_i c_j \tag{5.8}$$

$$y_3 = \frac{(\sigma^2)^3}{(\sigma^3)^2} \tag{5.9}$$

$$\sigma^k = \sum_{i=1}^{n} c_i d_i^k \qquad k = 2,3 \tag{5.10}$$

Here, d_i is the atomic diameter of the i-th element. The mismatch entropy of the multicomponent system with N elements is calculated as a function of the atomic diameter, composition and packing fraction.

The calculated results are ΔH = -14.5 kJmol^{-1} for $Al_{86}Ni_8Y_6$ and ΔH = -14.1kJmol^{-1} for $Al_{86}Ni_6Co_2Y_{4.5}La_{1.5}$, respectively. The difference of ΔH between $Al_{86}Ni_8Y_6$ and $Al_{85}Ni_6Co_2Y_{4.5}La_{1.5}$ is small because the enthalpy of mixing (ΔH^{mix}) of La-Y and Ni-Co is nearly 0, and there is no large difference in ΔH^{mix} between Y-Al (-38 kJmol^{-1}) and La-Al (-38 kJmol^{-1}), similarly as between Ni-Al (-22 kJmol^{-1}) and Co-Al (-19 kJmol^{-1}). Furthermore, because of the similar size of Ni and Co as well as of Y and La, the change of mismatch entropy ΔS_{mis} according to the atomic size difference should be small either. The values of $T\Delta S_{mis}$ of $Al_{86}Ni_8Y_6$ and $Al_{85}Ni_6Co_2Y_{4.5}La_{1.5}$ are 2.0×10^{-22} kJmol^{-1} and 1.9×10^{-22} kJmol^{-1}, respectively, which can be neglected compared to the changes in ΔH.

The main difference in ΔG is contributed by the change of ΔS_{conf}. In this work, though we only substitute 2 at% of Ni by Co, and 1.5 at% of Y by La, the $T\Delta S_{conf}$ increase is from 4.4 to 5.1 kJmol^{-1} which is about 0.7 kJmol^{-1}. This indicates that small amounts of substitution can increase ΔS_{conf} thereby increasing the GFA. The ΔG of $Al_{86}Ni_8Y_6$ and $Al_{85}Ni_6Co_2Y_{4.5}La_{1.5}$ are -18.8 and -19.3 kJmol^{-1} at 1050K which is above the liquidus temperature of both alloys. The main effect to change ΔG by different ΔS_{conf} of the two alloys thus can clearly be understood. Though the change of ΔG resulting from the increase in ΔS_{conf} is small, it obviously causes an increase in GFA. Further lowering of ΔG and a correlated increase in GFA can thus be achieved when a bigger amount of elements is substituted.

5.2.3 The Cluster Line Model

The composition of Al-rich Al-Ni-Y alloy with maximum GFA has been determined by the use of the cluster line model [23, 24]. This model assumes pronounced SRO around both Ni and Y in the alloy which can be described as local clusters with Ni or Y in their centres. The numbers of nearest Al neighbours (coordination number) was taken from ab-initio simulations based on density functional theory [74]. The composition of the alloy having the best GFA in the three-component Al-TM-RE alloy system is given by the intersection of the two cluster lines, the composition of each of them being determined by the number of nearest neighbours given by the atomic radii of the corresponding elements. The coordination numbers of 9.4 for Ni and 16.9 for Y taken from ref [74] yielded an alloy with composition $Al_{85.8}Ni_{9.1}Y_{5.1}$ [24] in reasonable agreement with the composition $Al_{86}Ni_8Y_6$ which was determined experimentally to possess the best GFA in this alloy system.

In our work, however, the EXAFS results yielded coordination numbers $\boldsymbol{N} \sim 6$ for Ni and $\boldsymbol{N} \sim 9$ for Y which is in large disagreement with the values obtained by Sheng et al. [74] by ab-initio calculations for Ni ($\boldsymbol{N}$=9.4) and Y ($\boldsymbol{N}$=16.9). Those values served as input parameters to determine the favourable composition of $Al_{85.8}Ni_{9.1}Y_{5.1}$ alloy by the use of cluster line model. Using this prediction Yang produced Al-based bulk metallic glass in the composition of $Al_{86}Ni_8Y_6$ [24].

Six nearest neighbours around Ni is proved by some articles [32, 36]. The value of N(Y) = 9 is relatively low (see discussion above). Saksl et al. [31] and Sadoc et al. [130] reported that ***N(Y)*** is around 16 which agrees with the results of Sheng's work . In the present work, the use of the coordination number obtained from EXAFS analysis to determine the optimum composition for easy glass-formation by the cluster line model results in $Al_{78.3}Ni_{13.0}Y_{8.7}$ amorphous alloy, which has appreciably lower Al content compared to the value reported by Yang et al. The illustration of Yang's composition design and our new composition design is shown in Figure 5.16.

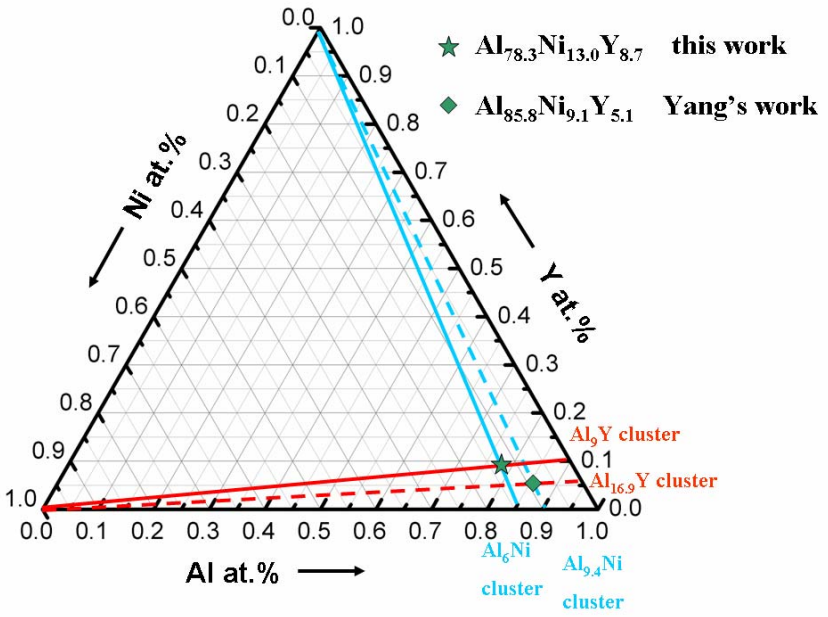

Figure 5.16: An illustration of the composition design of our alloy using the results of the EXAFS measurements.. The two solid lines denote the cluster lines obtained from our EXAFS measurements. For comparison, the cluster lines the used by Yang et al[23, 24]are added. The cubic symbol at the intersection of two dashed line is the favourable composition predicted from Yang's work, and the star symbol is what we predict in this work.

5.2.4 Dense Random Packing of Hard Spheres

The coordination number can be estimated by using the dense random packing of hard spheres (DRPHS) model. Using the principle of two-dimensional packing, results in [140]:

$$\omega_{BA} = 2\pi\left[1 - \frac{\sqrt{R_B(R_B + 2R_A)}}{R_A + R_B}\right] \tag{5.11}$$

and

$$\dot{N}_{BA} = 4\pi\frac{\eta_{\Pi}}{\omega_{BA}} \tag{5.12}$$

where ω_{BA} is the solid angle covered by ***A*** atom at ***B*** atom, $\boldsymbol{R_{A(B)}}$ is the atomic radius of ***A(B)*** atoms, $\dot{N}_{BA}$ is the number of nearest neighbours of ***A*** atoms coordinating the ***B*** atoms. In this work, ***B*** atoms are Al atoms in Al-based amorphous alloys, η_{Π} is the density of two-

dimensional packing (=0.842 for dense random packing). The calculated result of $\dot{N}_{BA}$ is listed in Table 5.7. This table contains EXAFS fitting parameters from our results and references. The coordination number ***N*** of Ge in this work and of Y and La in Ref. [31-33, 130] is the sum of the two shells obtained by fitting a two-shell model.

Table 5.7: Parameters, obtained by fitting EXAFS data from this work and from literature. ***N****: number of nearest neighbours;* ***R:*** *distance of nearest neighbours. For comparison, the sum of the atomic radii of the absorbing atom and the aluminium atom,* $\boldsymbol{R^* = r_{AA} + r_{Al}}$ *determined by the use of atomic radii listed in Ref [33],* $\dot{N}_{Al-A}$ *, the number of nearest neighbours of* ***Al*** *atoms coordinating the A atom, is listed.*

alloy	Absorbing atom	***N***	***R***(Å)	$\dot{N}_{Al-A}$	$R_{Al\text{-}A}$ (Å)	reference
$Ge_1Al_{86}Ni_7Y_6$	Ge	4.3±0.6 (2 shells)	2.62±0.01 (1^{st} shell)	10.8	2.67	This work
$Al_{88}Fe_5Y_7$	Fe	9±0.5	2.46±0.05	10.8	2.67	Sadoc[130]
$Al_{87.5}Fe_5Y_7Ti_{0.5}$	Fe	9±0.5	2.46±0.05	10.8	2.67	Sadoc[130]
$Al_{90}Fe_5Ce_5$	Fe	6.2	2.49	10.8	2.67	Hsieh[34, 35]
$Al_{90}Fe_7Ce_3$	Fe	6.3	2.49	10.8	2.67	Hsieh[34, 35]
$Al_{88}Fe_5Y_7$	Fe	7.2±0.3	2.45±0.01	10.8	2.67	Saksl[31]
$Al_{80}Fe_{10}Ce_{10}$	Fe	6.4±0.2	2.46±0.01	10.8	2.67	Mansour[28]
$Al_{85}Ni_{10}La_5$	Ni	5.9±0.3	2.44±0.01	10.9	2.68	This work
$Al_{86}Ni_8Y_6$	Ni	6.3±0.2	2.45±0.01	10.9	2.68	This work
$Al_{86}Ni_6Co_2Y_{4.5}La_{1.5}$	Ni	6.2±0.3	2.44±0.01	10.9	2.68	This work
$Ge_1Al_{86}Ni_7Y_6$	Ni	6.0±0.2	2.44±0.01	10.9	2.68	This work
$Pd_1Al_{86}Ni_7Y_6$	Ni	5.8±0.3	2.43±0.01	10.9	2.68	This work
$Ag_1Al_{86}Ni_7Y_6$	Ni	6.1±0.3	2.44±0.01	10.9	2.68	This work
$Ag_1Al_{87}Ni_5La_7$	Ni	6.2±0.3	2.44±0.01	10.9	2.68	Wollgarten[127]
$Zr_1Al_{86}Ni_7Y_6$	Ni	6.0±0.2	2.44±0.01	10.9	2.68	This work
$Zr_1Al_{87}La_7Ni_5$	Ni	6.0±0.2	2.44±0.03	10.9	2.68	Wollgarten[127]
$Al_{88}Ni_2Y_{10}$	Ni	5.9±1.0	2.43±0.03	10.9	2.68	Zalewski[36]
$Al_{88}Ni_2Sm_8$	Ni	5.7±1.0	2.44±0.03	10.9	2.68	Zalewski[36]
$Al_{88}Ni_4Sm_8$	Ni	5.7±1.0	2.44±0.03	10.9	2.68	Zalewski[36]
$Al_{88}Ni_5Y_{10}$	Ni	5.2±1.0	2.44±0.03	10.9	2.68	Zalewski[36]
$Al_{88}Ni_8Y_{10}$	Ni	5.1±1.0	2.44±0.03	10.9	2.68	Zalewski[36]
$Al_{89}Ni_5La_6$	Ni	6±0.5	2.43±0.01	10.9	2.68	Saksl[32]
$Al_{86}Ni_6Co_2Y_{4.5}La_{1.5}$	Co	6.3±0.2	2.42±0.02	10.9	2.68	This work
$Al_{88}Co_4Sm_8$	Co	5.1±1.0	2.43±0.03	10.9	2.68	Zalewski[36]

$Al_{88}Co_5Y_{10}$	Co	5.9±1.0	2.45±0.03	10.9	2.68	Zalewski[36]
$Al_{80}Co_{10}Ce_{10}$	Co	5.8±0.2	2.44±0.01	10.9	2.68	Mansour[28]
$Al_{82}Co_9Ce_9$	Co	6.2±0.2	2.44±0.01	10.9	2.68	Mansour[28]
$Al_{84}Co_8Ce_8$	Co	6.4±0.2	2.44±0.01	10.9	2.68	Mansour[28]
$Pd_1Al_{86}Ni_7Y_6$	Pd	5.7±0.5	2.61±0.01	12.0	2.81	This work
$Al_{88}Fe_5Y_7$	Al	12±0.5	2.77±0.05	12.6	2.86	Sadoc[130]
$Al_{87.5}Fe_5Y_7Ti_{0.5}$	Al	12±0.5	2.75±0.05	12.6	2.86	Sadoc[130]
$Ag_1Al_{86}Ni_7Y_6$	Ag	4.8±0.5	2.66±0.01	12.7	2.88	This work
$Ag_1Al_{87}Ni_5La_7$	Ag	5.5±0.4	2.67±0.01	12.7	2.88	Wollgarten[127]
$Zr_1Al_{86}Ni_7Y_6$	Zr	8.5±1.0	2.85±0.01	14.2	3.03	This work
$Zr_1Al_{87}Ni_5La_7$	Zr	8.4±1.1	2.91±0.02	14.2	3.03	Wollgarten[127]
$Ag_1Al_{86}Ni_7Y_6$	Y	9.0±0.5	3.15±0.02	16.3	3.23	This work
$Zr_1Al_{86}Ni_7Y_6$	Y	7.8±0.5	3.10±0.01	16.3	3.23	This work
$Ge_1Al_{86}Ni_7Y_6$	Y	8.9±0.5	3.13±0.01	16.3	3.23	This work
$Pd_1Al_{86}Ni_7Y_6$	Y	8.4±0.5	3.12±0.01	16.3	3.23	This work
$Al_{86}Ni_8Y_6$	Y	9.2±0.4	3.12±0.01	16.3	3.23	This work
$Al_{86}Ni_6Co_2Y_{4.5}La_{1.5}$	Y	9.2±0.6	3.12±0.01	16.3	3.23	This work
$Al_{88}Fe_5Y_7$	Y	15.8 (2 shells)	3.09 (1^{st} shell)	16.3	3.23	Saksl[31]
$Al_{88}Fe_5Y_7$	Y	16 (2 shells)	3.11 (1^{st} shell)	16.3	3.23	Sadoc[130]
$Al_{87.5}Fe_5Y_7Ti_{0.5}$	Y	16 (2 shells)	3.11 (1^{st} shell)	16.3	3.23	Sadoc[130]
$Al_{80}Co_{10}Ce_{10}$	Ce	13.2±0.8	3.13±0.01	16.5	3.26	Mansour[28]
$Al_{80}Fe_{10}Ce_{10}$	Ce	13.7±1.3	3.11±0.01	16.5	3.26	Mansour[28]
$Al_{85}Ni_{10}La_5$	La	18.1±2.6	3.37±0.05	17.1	3.31	This work
$Ag_1Al_{87}Ni_5La_7$	La	18.5±1.8	3.32±0.01	17.1	3.31	Wollgarten[127]
$Zr_1Al_{87}Ni_5La_7$	La	19.3±2.3	3.31±0.02	17.1	3.31	Wollgarten[127]
$Al_{89}Ni_5La_6$	La	15.8 (2 shells)	3.28 (1^{st} shell)	17.1	3.31	Saksl[32]

We plotted ***N*** as a function of ***R*** by using all the data listed in Table 5.7. The results are shown in Figure 5.17. The dashed line follows the linear trend of the DRPHS model, which takes into account the metallic radii. The experimental EXAFS results show a large disagreement with DRPHS model except Sadoc's results [130] which is represented in three smaller dotted circles. Because Sadoc's results are also in disagreement with Mansour's and Saksl's works, we donot consider Sadoc's results in this discussion. Three groups of atoms can be distin-

guished by comparing coordination numbers. The first group which we named 'small atoms' contain Ge, Fe, Ni, Co, Pd and Ag with metallic radii <1.45Å [141]. Their coordination number ***N*** is keeping around 4 to 7, which is in disagreement with most topological structure models. This is because most models are based on DRPHS models. However, it is possible to explain the low coordination number by using Senkov and Miracle's topological model [71-73, 142]. They proposed smallest solutes in ternary metallic glasses which occupy the centre of octahedral or tetrahedral clusters. The low coordination number can be considered that the solute atoms form octahedral or tetrahedral clusters with Al atoms, and this cluster acts as a "glue cluster" to connect 6 or 4 clusters formed by Al and big solute (Y and RE elements). In other words, the group of "small atoms" forms a "glue cluster" which occupies the centre of cluster-octahedra or cluster-tetrahedra. We have to point out that the metallic radius of Ag (1.44 Å) is larger than that of Al solvent (1.43 Å) atoms, however, Ag atoms occupy the octahedral centre of Al with a significant bond length shorting of 6.2% which indicates a strong covalent Ag-Al bond. Furthermore, for the atoms in this group, the metallic radii cannot be used to estimate the topological structure e.g., by DRPHS model. The second group named 'medium atoms' includes Zr and Y, and has 8 to 9 nearest neighbouring Al atoms. The atoms in this group will not occupy the centres of octahedra or tetrahedra as group of "small atoms" and also not agree with the DRPHS estimation. Finally, the coordination numbers of Al clusters with "big atoms" in their centres, as La and Ce, are close to the DRPHS line, whose local structure can be estimated by metallic atomic radii.

The value of ***N***(Y) = 9 in this work is in disagreement with the results of Saksl et al. [31] and Sadoc et al. [130] who found that N of Y is ~16. As discussed above, the values of ***N(Y)*** strongly depend on the composition and the reasons for these variations are not clear. We therefore ignore the values of ***N(Y)*** in the following discussion. An approximately linear trend of ***N*** can be seen which increases from 5 to 18 from Ag via Zr, and Ce to La. This result indicates that the size of Ag is a limitation to occupy the centres of octahedral clusters. It just fits into the centres of the Al-octahedra due to its dramatic decrease in the effective radius. Beyond the size of Ag, the metallic size of the elements plays more and more the dominating role to decide the local structure.

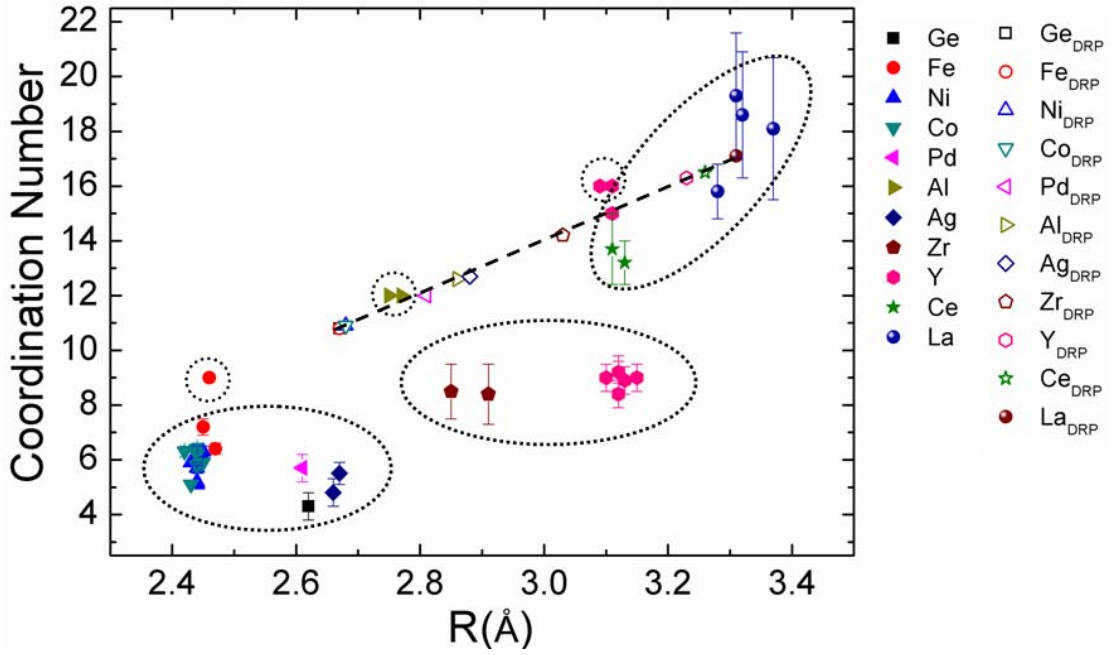

Figure 5.17: Coordination number N as a function of bond length R

Furthermore, the effective radii r_{eff} in the amorphous alloys are estimated from the ***N*** and ***R*** values determined by EXAFS, applying Eqs.5.11 and 5.12, and employing the fact that ***R*** is equal to the sum of the effective atomic radii. The values of r_{eff} are listed in Table 5.8. Ge, Ni, Co, Pd and Ag which belong to the "small atoms" group show a strong shortening from their atomic radii by 55%, 46%, 46%, 45% and 49%, respectively. The shortening of r_{eff} ***(Zr)*** and r_{eff} ***(Y)*** which belong to the "medium atoms" group are 27% and 27%, respectively, which is small compared to the values observed for the "small atoms". r_{eff} ***(La)*** of a "large atom" corresponds nearly to the atomic radius. The rather reduced effective radii of "small atoms" and increased size of Al may be explained in a electronic view [35]. The electrons in s-p orbitals of Al transfer to the d-orbitals of Ni and Co, the 4 p-orbital of Ge, and the 5 s-orbital of Ag and Pd to form delocalized d-, p-, or s- bands. Hsieh et al. [35] and Mansour et al. [28] discussed this electronic view for Fe-Al bonds in Al-based amorphous alloys which supports the above interpretation.

The reduced effective radii of "small atoms" and "medium atoms" suggests that the application of DRPHS models to predict glass-forming ability must be revised due to the strong

bond-shortening of the elements in the alloy while the SRO of Lanthanides in Al-based amorphous alloys can be well described within the DRPHS model using the radii of the atoms in the pure systems.

Table 5.8: Comparison of atomic radii ***r*** *and effective radii* r_{eff} *of different atomic bonds.*

Atomic bond	r_{eff} (Å)	r(Å)	Electron configuration
Ge-Al	Ge: 0.56 Al: 2.06	Ge: 1.24 Al: 1.43	Ge:{Ar}$3d^{10}$ $4s^2$ $4p^2$
Ni-Al	Ni: 0.67 Al: 1.68	Ni: 1.25 Al: 1.43	Ni: {Ar} $4s^2$ $3d^8$ or {Ar} $4s^1$ $3d^9$
Co-Al	Co: 0.67 Al: 1.68	Co: 1.25 Al: 1.43	Co: {Ar} $4s^2$ $3d^7$
Pd-Al	Pd: 0.76 Al: 1.85	Pd: 1.38 Al: 1.43	Pd: {Kr} $4d^{10}$
Ag-Al	Ag: 0.74 Al: 1.93	Ag: 1.44 Al: 1.43	Ag: {Kr} $4d^{10}$ $5s^1$
Zr-Al	Zr: 1.17 Al: 1.71	Zr: 1.60 Al: 1.43	Zr: {Kr} $4d^2 5s^2$
Y-Al	Y: 1.30 Al: 1.82	Y: 1.80 Al: 1.43	Y: {Kr} $4d^1$ $5s^2$
La-Al	La: 1.94 Al: 1.39	La: 1.88 Al: 1.43	La: {Xe} $5d^1$ $6s^2$

6 Summary and Conclusions

The He-atomized Al-based amorphous alloy was investigated by scanning electron microscopy, differential scanning calorimetry, X-ray diffractometry, transmission electron microscopy, and X-ray absorption spectroscopy in the as-atomized state and after ball milling for different times. Several pronounced changes in atomic arrangement and thermal behaviour were observed and discussed concerning topological, kinetic and thermodynamic aspects. The main results are as following:

1. Nanocrystalline fcc-Al precipitated in the amorphous matrix during ball milling. The crystallite size of about 10 nm was constant because of the limitation of the thickness of the shear bands induced by severe plastic deformation. After ball milling for 6000 min, the volume fraction of α-Al reached about 6%.
2. The thermal behavior of He-atomized $Al_{85}Ni_{10}La_5$ powder changed during ball milling. In the as-atomized state, the crystallization process of the $Al_{85}Ni_{10}La_5$ amorphous alloy is governed rather by a simultaneous reaction than by a primary reaction. During ball milling, the glass transition gradually vanished and led to a decrease of the first exothermal peak while the second exothermal peak at higher temperature gradually increased. After ball milling for 6000 min, the first crystallization peak had gone.
3. It is proved in this work that the devitrification of the Al-based amorphous alloy during ball milling was due to a combined influence of temperature and plastic deformation.
4. XAS measurements on He-atomized $Al_{85}Ni_{10}La_5$ glassy alloy in the as-atomized state and in the plastically deformed condition were done in this work. The coordination

number ***N(Ni)*** decreased exponentially from nearly 6 in as-atomized state to 5 in highly damaged state.

5. A shear-band model was introduced to describe the exponential decrease, in which ***N(Ni)*** = 5 in the shear bands and ***N(Ni)*** = 6 outside.
6. Ball milling leads to a reduced ordering and a concomitant excess free volume, which is an opposite effect to that of heat treatment. It is found that plastic deformation causes an effect analogous to an increase of temperature in the liquid state.

The local structure of Al-based amorphous alloy after microalloying by element substitution was investigated in the second part of this work. Minor substitutions of Ni by Co, Ge, Pd, Ag and Zr in the Al-Ni-Y and Al-Ni-La systems were investigated by XAS. The main findings include:

1. Partial substitution of Ni by Co does not change short-range order (SRO) around Ni in $Al_{86}Ni_8Y_6$. The similarities of ***N, R,*** $\boldsymbol{\sigma^2}$ imply that element substitution of Ni by Co can be considered as a site substitution.
2. After substitution of Ni by Co and Y by La, Co goes to the same octahedral site surrounded by Al as Ni, which matches Miracle's topological model of atomic arrangement in metallic glasses.
3. The enhancement of glass-forming ability by substituting Ni by Co was discussed under a thermodynamic viewpoint. The free energy of mixing $\boldsymbol{\Delta G}$, the mixing enthalpy $\boldsymbol{\Delta H}$ and the mixing entropy $\boldsymbol{\Delta S}$ of $Al_{86}Ni_8Y_6$ and $Al_{86}Ni_6Co_2Y_{4.5}La_{1.5}$ were calculated. The main difference in $\boldsymbol{\Delta G}$ is contributed by the change of the configurational part of the mixing entropy $\boldsymbol{\Delta S_{conf}}$.
4. The XAS results show a coordination number ***N*** of ~6 for Ni and ~11 for Y, which disagrees with the ab-initio calculations of Sheng et al. and with the results obtained by Yang using the cluster line model.
5. Most of the XAS results are in large disagreement with the model of dense random packing hard spheres (DRPHS). Furthermore, geometric models based on the metallic radii of the constituting elements are not appropriate to describe the structure of Al-TM-RE amorphous alloys and should be corrected. Three groups of elements which are denoted as "small", "medium" and "large" atoms were identified when substituting

elements in the alloys. The “small” atoms can be described by Miracle’s model while the “large” atoms match the DRPHS model.

7 Outlook

Many interesting phenomena in this research area are still not clear and need further research in the future. For example:

1. Ball milling at the temperature of liquid N_2 could be performed to determine the critical temperature, below which Al precipitates cannot be produced by ball milling.

2. Up to date, it is not entirely clear whether the composition change by fcc-Al precipitation or the free volume induced in local structure is the reason for the decrease of the coordination number ***N*** during plastic deformation. In this work, EXAFS was shown that the peak amplitude of Fourier transforms of ball-milled powder increases after annealing which is the opposite compared to ball milling. This result should be confirmed by further measurements because it could prove that the decrease of ***N*** is not due to a change of composition. In order to get sufficiently large differences in the EXAFS-signals, these measurements should be done on specimens ball-milled for longer times than 1200 min, followed by appropriate subsequent annealing.

3. Small-angle neutron scattering (SANS) experiments on ball-milled powder at the neutron reactor in HZB have been performed. The results show a decrease of heterogeneities at the nm range with increasing ball milling time. In order to interprete the results, a reasonable structural model to fit these data should be developed.

4. We started to ball-mill and analyze a partially crystalline powder with composition $Al_{86}Ni_8La_6$, which is different from the $Al_{85}Ni_{10}La_5$ alloy described in this work. XRD shows that the peak intensities of the diffraction peaks of fcc-Al decrease with increased ball milling time. This provided the motivation to ball-mill amorphous powder of the same composition to see whether fcc-Al nanocrystals form under deformation and whether the number and size of fcc-Al nanocrystals reach the same values independent from the initial state of the alloy. This would indicate a kind of equilibrium state which can be approached from different starting conditions. Furthermore, it would also be interesting to investigate the structure change of Al crystals and metastable phases contained in the Al-based amorphous alloy during ball milling.

References

1. Inoue, A., et al., *New Amorphous-alloys with good ductility in Al-Ce-Nb, Al-Ce-Fe, Al-Ce-Co, Al-Ce-Ni, Al-Ce-Cu systems.* Japanese Journal of Applied Physics Part 2-Letters, 1988. **27**(10): p. L1796-L1799.

2. Wilde, G., et al., *Nanocrystallization in Al-rich metallic glasses.* Advanced Engineering Materials, 2003. **5**(3): p. 125-130.

3. Kim, S.G., A. Inoue, and T. Masumoto, *Increase of mechanical strength of a Mg85Zn12Ce3 amorphous alloy by dispersion of ultrafine HCP-Mg particals.* Materials Transactions Jim, 1991. **32**(9): p. 875-878.

4. Bassim, N., C.S. Kiminami, and M.J. Kaufman, *Phases formed during crystallization of amorphous Al84Y9Ni5Co2 alloy.* Journal of Non-Crystalline Solids, 2000. **273**(1-3): p. 271-276.

5. Calin, M., A. Rudiger, and U. Koster, *Primary crystallization of Al-based metallic glasses*, in *Metastable, Mechanically Alloyed and Nanocrystalline Materials, Pts 1 and 2*, J. Eckert, H. Schlorb, and L. Schultz, Editors. 2000, Trans Tech Publications Ltd: Zurich-Uetikon. p. 359-364.

6. Foley, J.C., D.R. Allen, and J.H. Perepezko, *Analysis of nanocrystal development in Al-Y-Fe and Al-Sm glasses.* Scripta Materialia, 1996. **35**(5): p. 655-660.

7. Gogebakan, M., P.J. Warren, and B. Cantor, *Crystallization behaviour of amorphous Al85Y11Ni4 alloy.* Materials Science and Engineering a-Structural Materials Properties Microstructure and Processing, 1997. **226**: p. 168-172.

8. Inoue, A., *Amorphous, nanoquasicrystalline and nanocrystalline alloys in Al-based systems.* Progress in Materials Science, 1998. **43**(5): p. 365-520.

9. Paik, J.H., W.J. Botta, and A.R. Yavari, *Al-based nanostructures obtained from amorphous precursors*, in *Metastable, Mechanically Alloyed and Nanocrystalline Materials, Pts 1 and 2*, R. Schulz, Editor 1996, Transtec Publications Ltd: Zurich-Uetikon. p. 305-310.

10. Wu, R.I., G. Wilde, and J.H. Perepezko, *Glass formation and primary nanocrystallization in Al-base metallic glasses.* Materials Science and Engineering a-Structural Materials Properties Microstructure and Processing, 2001. **301**(1): p. 12-17.

11. Yavari, A.R., et al., *Nanostructured bulk Al90Fe5Nd5 prepared by cold consolidation of gas atomised powder using severe plastic deformation.* Scripta Materialia, 2002. **46**(10): p. 711-716.

12. Chen, H., et al., *Deformation-induced nanocrystal formation in shear bands of amorphous-alloys.* Nature, 1994. **367**(6463): p. 541-543.

13. He, Y., G.J. Shiflet, and S.J. Poon, *Ball Milling-induced Nanocrystal Formation in Aluminum-based Metallic Glasses.* Acta Metallurgica Et Materialia, 1995. **43**(1): p. 83-91.

14. Jiang, W.H. and M. Atzmon, *The effect of compression and tension on shear-band structure and nanocrystallization in amorphous Al90Fe5Gd5 : a high-resolution transmission electron microscopy study.* Acta Materialia, 2003. **51**(14): p. 4095-4105.

15. Liu, Y., et al., *Devitrification of glassy Al85Ni10La5 powder by thermal treatment and ball-milling.* Journal of Alloys and Compounds, 2011. **509**: p. S78-S81.

16. Vierke, J., et al., *Deformation-induced crystallization in amorphous Al85Ni10La5 alloy.* Journal of Alloys and Compounds, 2010. **493**(1-2): p. 683-691.

17. Perepezko, J.H., R.J. Hebert, and R.I. Wu, *Nanostructure synthesis and amorphization during cold rolling*, in *Metastable, Mechanically Alloyed and Nanocrystalline Materials*, E. Ma, M. Atzmon, and C.C. Koch, Editors. 2002, Trans Tech Publications Ltd: Zurich-Uetikon. p. 11-20.

18. Kim, J.J., et al., *Nanocrystallization during nanoindentation of a bulk amorphous metal alloy at room temperature.* Science, 2002. **295**(5555): p. 654-657.

19. Boucharat, N., et al., *Nanocrystallization of amorphous Al88Y7Fe5 alloy induced by plastic deformation.* Scripta Materialia, 2005. **53**(7): p. 823-828.

20. Vierke, J., *Processing and consolidation of amorphous and nanocrystalline aluminum-nickel-lanthanum alloys*, in *Technische Universität Berlin* 2008, Technische Universität Berlin Berlin.

21. Zhang, Z.H., Y.Z. Zhou, and E.J. Lavernia, *Amorphization and crystallization in Al-Ni-La during mechanical milling.* Journal of Alloys and Compounds, 2008. **466**(1-2): p. 189-200.

22. Sun, B.A., et al., *Aluminum-rich bulk metallic glasses.* Scripta Materialia, 2008. **59**(10): p. 1159-1162.

23. Yang, B.J., et al., *Developing aluminum-based bulk metallic glasses.* Philosophical Magazine, 2010. **90**(23): p. 3215-3231.

24. Yang, B.J., et al., *Al-rich bulk metallic glasses with plasticity and ultrahigh specific strength.* Scripta Materialia, 2009. **61**(4): p. 423-426.

25. Mechler, S., et al., *Local structure and site substitution in amorphous and quasicrystalline Zr-Ti-Ni-(Cu) alloys.* Applied Physics Letters, 2010. **97**(4):p. 041914-3

26. Bacewicz, R. and J. Antonowicz, *XAFS study of amorphous Al-RE alloys.* Scripta Materialia, 2006. **54**(6): p. 1187-1191.

27. Mansour, A.N., et al., *Amorphous Al90FexCe10-x alloys: X-ray absorption analysis of the Al, Fe and Ce local atomic and electronic structures.* Physical Review B, 2002. **65**(13): p. 134207

28. Mansour, A.N., C.P. Wong, and R.A. Brizzolara, *Atomic Structure of amorphous Al100-2xCoxCex (x=8, 9, and 10) and Al80Fe10Ce10 alloys - an XAFS study.* Physical Review B, 1994. **50**(17): p. 12401-12412.

29. Sadoc, A., V.T. Huett, and K.F. Kelton, *Local,structure in Ti-Hf-Ni metallic glasses and its evolution with hydrogenation.* Journal of Physics-Condensed Matter, 2005. **17**(10): p. 1481-1492.

30. Sadoc, A., et al., *Evolution of the local structure with hydrogenation in Ti-Zr-Ni quasicrystals and approximants.* Journal of Physics-Condensed Matter, 2002. **14**(25): p. 6413-6426.

31. Saksl, K., et al., *Atomic structure of Al88Y7Fe5 metallic glass.* Journal of Applied Physics, 2005. **97**(11): p. 113507-8

32. Saksl, K., et al., *Atomic structure of Al89La6Ni5 metallic glass.* Journal of Physics-Condensed Matter, 2006. **18**(32): p. 7579-7592.

33. *International Table for X-ray Crystallography*. 1968: Birmingham, England.

34. Hsieh, H.Y., et al., *Short-range Ordering in Amorphous Al90FexCe10-x.* Journal of Non-Crystalline Solids, 1991. **135**(2-3): p. 248-254.

35. Hsieh, H.Y., et al., *Atomic-structure of Amorphous Al90FexCe10-x.* Journal of Materials Research, 1990. **5**(12): p. 2807-2812.

36. Zalewski, W., et al., *Local atomic order in Al-based metallic glasses studied using XAFS method.* Journal of Alloys and Compounds, 2009. **468**(1-2): p. 40-46.

37. Luborsky, F.E., *Amorphous metallic alloys*. Butterworths monographs in materials1983, London: Butterworths. xiv, 534 p.

38. Guentherodt, H.J. and H. Beck, *Glassy metals*. Topics in applied physics1981, Berlin ; New York: Springer-Verlag. v. <1-3 >.

39. Cahn, R.W., *Metallic Glasses.* Contemporary Physics, 1980. **21**(1): p. 43-75.

40. Perepezko, J.H., *Nucleation-controlled reactions and metastable structures.* Progress in Materials Science, 2004. **49**(3-4): p. 263-284.

41. Klement, W., R.H. Willens, and P. Duwez, *Non-crystalline structure in solidified gold-silicon alloys.* Nature, 1960. **187**(4740): p. 869-870.

42. Inoue, A., *Stabilization of metallic supercooled liquid and bulk amorphous alloys.* Acta Materialia, 2000. **48**(1): p. 279-306.

43. Inoue, A., T. Zhang, and T. Masumoto, *Al-La-Ni amorphus alloys with a wide supercooled liquid region.* Materials Transactions Jim, 1989. **30**(12): p. 965-972.

44. Inoue, A., et al., *New Amorphous Gg-Ce-Ni alloys with high-strength and good ductillity.* Japanese Journal of Applied Physics Part 2-Letters, 1988. **27**(12): p. L2248-L2251.

45. Ma, H., et al., *Discovering inch-diameter metallic glasses in three-dimensional composition space.* Applied Physics Letters, 2005. **87**(18): p. 181915-3

46. Waniuk, T.A., J. Schroers, and W.L. Johnson, *Critical cooling rate and thermal stability of Zr-Ti-Cu-Ni-Be alloys.* Applied Physics Letters, 2001. **78**(9): p. 1213-1215.

47. Peker, A. and W.L. Johnson, *A highly processable metallic glass Zr41.2Ti13.8Cu12.5Ni10.0Be22.5.* Applied Physics Letters, 1993. **63**(17): p. 2342-2344.

48. Zhang, T. and A. Inoue, *Thermal and mechanical properties of Ti-Ni-Cu-Sn amorphous alloys with a wide supercooled liquid region before crystallization.* Materials Transactions Jim, 1998. **39**(10): p. 1001-1006.

49. Zhang, T. and A. Inoue, *Preparation of Ti-Cu-Ni-Si-B amorphous alloys with a large supercooled liquid region.* Materials Transactions Jim, 1999. **40**(4): p. 301-306.

50. Inoue, A., N. Nishiyama, and T. Matsuda, *Preparation of bulk glassy Pd40Ni10Cu30P20 alloy of 40 mm in diameter by water quenching.* Materials Transactions Jim, 1996. **37**(2): p. 181-184.

51. Schwarz, R.B. and Y. He, *Formation and properties of bulk amorphous Pd-Ni-P alloys*, in *Synthesis and Properties of Mechanically Alloyed and Nanocrystalline Materials, Pts 1 and 2 - Ismanam-96*, D. Fiorani and M. Magini, Editors. 1997, Transtec Publications Ltd: Zurich-Uetikon. p. 231-240.

52. Inoue, A. and J.S. Gook, *Fe-based ferromagnetic glassy alloys with wide supercooled liquid region.* Materials Transactions Jim, 1995. **36**(9): p. 1180-1183.

53. Inoue, A., et al., *New Fe-Co-Ni-Zr-B amorphous alloys with wide supercooled liquid regions and good soft magnetic properties.* Materials Transactions Jim, 1997. **38**(4): p. 359-362.

54. Inoue, A., *Bulk amorphous alloys : preparation and fundamental characteristics*. Materials science foundations,1998, Uetikon-Zuerich, Switzerland ; Enfield, N.H.: Trans Tech. 116 p.

55. Inoue, A., *Bulk Amorphous Alloys*, in *Trans Tech Publication*1998: Zuerich.

56. Turnbull, D., *Under What Conditions Can a Glass Be Formed.* Contemporary Physics, 1969. **10**(5): p. 473-488.

57. He, Y., S.J. Poon, and G.J. Shiflet, *Synthesis and properties of metallic glasses that contain aluminum.* Science, 1988. **241**(4873): p. 1640-1642.

58. Nitsche, H., *Kinetics of Crystallization in Amorphous Alloys; Nucleation and Growth*, in *Max-Planck-Institut für Metallforschung*2005, Universität Stuttgart: Stuttgart.

59. de Oliveira, M.F., et al., *Topological instability, average electronegativity difference and glass forming ability of amorphous alloys.* Intermetallics, 2009. **17**(4): p. 183-185.

60. Fang, S.S., et al., *Two mathematical models for the hydrogen storage properties of AB(2) type alloys.* Journal of Alloys and Compounds, 1999. **293**: p. 10-13.

61. Cohen, M.H. and D. Turnbull, *Molecular Transport in Liquids and Glasses.* Journal of Chemical Physics, 1959. **31**(5): p. 1164-1169.

62. Turnbull, D. and M.H. Cohen, *Free-Volume Model of Amorphous Phase - Glass Transition.* Journal of Chemical Physics, 1961. **34**(1): p. 120.

63. Michael Miller, P.L., ed. *Bulk Metallic Glasses: An Overview*. 2008, Springer.

64. Chen, H.S., *Glassy metalls.* Reports on Progress in Physics, 1980. **43**(4): p. 353-432.

65. Spaepen, F., *Microscopic mechanism for steady state inhomogeneous flow in metallic glasses.* Acta Metallurgica, 1977. **25**(4): p. 407-415.

66. Steif, P.S., F. Spaepen, and J.W. Hutchinson, *Strain localization in amorphous metals.* Acta Metallurgica, 1982. **30**(2): p. 447-455.

67. Yang, B., et al., *Dynamic evolution of nanoscale shear bands in a bulk-metallic glass.* Applied Physics Letters, 2005. **86**(14): p. 141904-3.

68. Bernal, J.D., *The structure of liquids.* Scientific American, 1960. **203**(2): p. 124.

69. Beck, H., H.J. Gontherodt, and M. Von Allmen, *Glassy metals II : atomic structure and dynamics, electronic structure, magnetic properties*. Topics in applied physics1983, Berlin: Springer. xvi, 395 p.

70. Finney, J.L., *Random packing and structure of simple liquids 2. molecular geometry of simple liquids.* Proceedings of the Royal Society of London Series a-Mathematical and Physical Sciences, 1970. **319**(1539): p. 495.

71. Miracle, D.B., *A structural model for metallic glasses.* Nature Materials, 2004. **3**(10): p. 697-702.

72. Miracle, D.B. and O.N. Senkov, *A geometric model for atomic configurations in amorphous Al alloys.* Journal of Non-Crystalline Solids, 2003. **319**(1-2): p. 174-191.

73. Miracle, D.B. and O.N. Senkov, *Topological criterion for metallic glass formation.* Materials Science and Engineering a-Structural Materials Properties Microstructure and Processing, 2003. **347**(1-2): p. 50-58.

74. Sheng, H.W., et al., *Atomic packing in multicomponent aluminum-based metallic glasses.* Acta Materialia, 2008. **56**(20): p. 6264-6272.

75. Sahoo, K.L., et al., *Crystallization behavior and microhardness evolution in Al92-xNi8Lax amorphous alloys.* Journal of Materials Research, 2005. **20**(11): p. 2927-2933.

76. Valiev, R., *Nanostructuring of metals by severe plastic deformation for advanced properties.* Nature Materials, 2004. **3**(8): p. 511-516.

77. Koch, C.C., *Structural nanocrystalline materials: an overview.* Journal of Materials Science, 2007. **42**(5): p. 1403-1414.

78. Busch, R., J. Schroers, and W.H. Wang, *Thermodynamics and kinetics of bulk metallic glass.* Mrs Bulletin, 2007. **32**(8): p. 620-623.

79. Schuh, C.A., T.C. Hufnagel, and U. Ramamurty, *Overview No.144 - Mechanical behavior of amorphous alloys.* Acta Materialia, 2007. **55**(12): p. 4067-4109.

80. Argon, A.S. and H.Y. Kuo, *Plastic flow in a disordered bubble raft (an analog of a metallic glass).* Materials Science and Engineering, 1979. **39**(1): p. 101-109.

81. Jiang, W.H. and M. Atzmon, *Mechanically-assisted nanocrystallization and defects in amorphous alloys: A high-resolution transmission electron microscopy study.* Scripta Materialia, 2006. **54**(3): p. 333-336.

82. Jiang, W.H., F.E. Pinkerton, and M. Atzmon, *Effect of strain rate on the formation of nanocrystallites in an Al-based amorphous alloy during nanoindentation.* Journal of Applied Physics, 2003. **93**(11): p. 9287-9290.

83. Wesseling, P., et al., *Effects of annealing and annealing with pressure on devitrification of Al87Ni7Gd6*, in *Supercooled Liquids, Glass Transition and Bulk Metallic Glasses*, T. Egami, et al., Editors. 2003, Materials Research Society: Warrendale. p. 365-370.

84. Lewandowski, J.J. and A.L. Greer, *Temperature rise at shear bands in metallic glasses.* Nature Materials, 2006. **5**(1): p. 15-18.

85. Demetriou, M.D. and W.L. Johnson, *Shear flow characteristics and crystallization kinetics during steady non-isothermal flow of Vitreloy-1.* Acta Materialia, 2004. **52**(12): p. 3403-3412.

86. Karpe, N., K.K. Larsen, and J. Bottiger, *Eehanced interdiffusion in amorphous Ni-Zr thin films under tensile strain.* Philosophical Magazine B-Physics of Condensed Matter Statistical Mechanics Electronic Optical and Magnetic Properties, 1992. **66**(4): p. 507-512.

87. Wilde, G. and H. Rosner, *Nanocrystallization in a shear band: An in situ investigation.* Applied Physics Letters, 2011. **98**(25): p. 251904-6

88. Cini, E., B. Vinet, and P.J. Desre, *A thermodynamic approach to homogeneous nucleation via fluctuations of concentration in binary liquid alloys.* Philosophical Magazine a-Physics of Condensed Matter Structure Defects and Mechanical Properties, 2000. **80**(4): p. 955-966.

89. Inoue, A., et al., *New amorphous alloys with good ductility in Al-Y-M and Al-La-M (M=Fe, Co, Ni or Cu) systems.* Japanese Journal of Applied Physics Part 2-Letters, 1988. **27**(3): p. L280-L282.

90. Cullity, B.D. and S.R. Stock, *Elements of X-ray diffraction*. 3rd ed2001, Upper Saddle River: Pearson Education International : Prentice Hall. xviii, 664 p.

91. Cullity, B.D., *Elements of X-ray diffraction*. 2nd ed1978, Reading, Mass ; London: Addison-Wesley. 1 , xii, 555 p.

92. Chen, L.C. and F. Spaepen, *Analysis of calorimetric measurements of grain growth.* Journal of Applied Physics, 1991. **69**(2): p. 679-688.

93. Kissinger, H.E., *Variation of peak temperature with heating rate in differential thermal analysis.* Journal of Research of the National Bureau of Standards, 1956. **57**(4): p. 217-221.

94. Kissinger, H.E., *Reaction kinetics in differential thermal analysis.* Analytical Chemistry, 1957. **29**(11): p. 1702-1706.

95. Williams, D.B. and C.B. Carter, *Transmission electron microscopy : a textbook for materials science*1996, New York ; London: Plenum.

96. Newville, M., *EXAFS analysis using FEFF and FEFFIT.* Journal of Synchrotron Radiation, 2001. **8**: p. 96-100.

97. Ravel, B. and M. Newville, *ATHENA, ARTEMIS, HEPHAESTUS: data analysis for X-ray absorption spectroscopy using IFEFFIT.* Journal of Synchrotron Radiation, 2005. **12**: p. 537-541.

98. Teo, B.K., *EXAFS : basic principles and data analysis*1986, Berlin ; New York: Springer-Verlag. xviii, 349 p.

99. Teo, B.K., D.C. Joy, and Materials Research Society., *EXAFS spectroscopy, techniques and applications*1981, New York: Plenum Press. viii, 275 p.

100. Ravel, B., *ATOMS: crystallography for the X-ray absorption spectroscopist.* Journal of Synchrotron Radiation, 2001. **8**: p. 314-316.

101. Rehr, J.J., et al., *Thoretical X-ray absorption fine-structure standards.* Journal of the American Chemical Society, 1991. **113**(14): p. 5135-5140.

102. Louzguine, D.V., S. Sobu, and A. Inoue, *The influence of scandium in effecting fragile to strong glass transition in aluminium-based alloys.* Applied Physics Letters, 2004. **85**(17): p. 3758-3759.

103. Louzguine-Luzgin, D.V. and A. Inoue, *Structure and transformation behaviour of a rapidly solidified Al-Y-Ni-Co-Pd alloy.* Journal of Alloys and Compounds, 2005. **399**(1-2): p. 78-85.

104. Sahoo, K.L., et al., *Effect of La on the crystallization behaviour of amorphous Al94-xNi6Lax (x=4-7) alloys.* Acta Materialia, 2005. **53**(14): p. 3861-3870.

105. Hebert, R.J., et al., *Dislocation formation during deformation-induced synthesis of nanocrystals in amorphous and partially crystalline amorphous Al88Y7Fe5 alloy.* Scripta Materialia, 2006. **54**(1): p. 25-29.

106. Lee, S.W., et al., *Mechanism of the deformation-induced nanocrystallization in a Cu-based bulk amorphous alloy under uniaxial compression.* Scripta Materialia, 2006. **54**(8): p. 1439-1444.

107. Suryanarayana, C., *Mechanical alloying and milling.* Progress in Materials Science, 2001. **46**(1-2): p. 1-184.

108. Matsuura, M., et al., *EXAFS Debye-Waller factors of La and Ni in LaNi5.* Journal of Alloys and Compounds, 2005. **390**(1-2): p. 31-34.

109. Anderson, R., et al., *An EXAFS study of rare-earth phosphate glasses in the vicinity of the metaphosphate composition.* Journal of Non-Crystalline Solids, 1998. **232**: p. 286-292.

110. Bowron, D.T., et al., *EXAFS studies of rare-earth metaphosphate glasses.* Physical Review B, 1996. **53**(9): p. 5268-5275.

111. Zhuang, Y.X., et al., *Evidence of eutectic crystallization and transient nucleation in Al89La6Ni5 amorphous alloy.* Applied Physics Letters, 2001. **79**(6): p. 743-745.

112. Chen, H., et al., *Mechanical properties of partially crystallized aluminum based metallic glasses.* Scripta Metallurgica Et Materialia, 1991. **25**(6): p. 1421-1424.

113. Radiguet, B., et al., *Segregation-controlled nanocrystallization in an Al-Ni-Lametallic glass.* Applied Physics Letters, 2008. **92**(10): p. 103126-3.

114. Sahu, R., S. Chatterjee, and K.L. Sahoo, *Mechanical Properties and Nanocrystallization Behavior of Al-Ni-La Alloys.* Metallurgical and Materials Transactions a-Physical Metallurgy and Materials Science, 2010. **41A**(4): p. 861-869.

115. Perepezko, J.H., et al., *Nanocrystallization reactions in amorphous aluminum alloys.* Materials Transactions, 2003. **44**(10): p. 1982-1992.

116. Perepezko, J.H., et al., *Analysis of primary crystallization in amorphous aluminum alloys*, in *Supercooled Liquids, Glass Transition and Bulk Metallic Glasses*, T. Egami, et al., Editors. 2003, Materials Research Society: Warrendale. p. 347-352.

117. Zhang, Y. and A.L. Greer, *Thickness of shear bands in metallic glasses.* Applied Physics Letters, 2006. **89**(7): p. 071907-3.

118. Zhang, Z.H., D. Witkin, and E.J. Lavernia, *Crystallization behavior of a gas atomized Al85Ni10La5 amorphous alloy.* Journal of Non-Crystalline Solids, 2005. **351**(19-20): p. 1646-1652.

119. Zhang, P.N., et al., *Effect of rolling deformation on the structure of bulk Zr(60)Cu(30)Al(10) amorphous alloy.* Journal of Alloys and Compounds, 2009. **475**(1-2): p. 165-167.

120. Spaepen, F., *Metallic glasses: Must shear bands be hot?* Nature Materials, 2006. **5**(1): p. 7-8.

121. Wang, X.D., et al., *Atomic-level structural modifications induced by severe plastic shear deformation in bulk metallic glasses.* Scripta Materialia, 2011. **64**(1): p. 81-84.

122. Jacobs, G. and I. Egry, *EXAFS studies on undercooled liquid Co80Pd20 alloy.* Physical Review B, 1999. **59**(6): p. 3961-3968.

123. Takeuchi, S., *Structure and fluidity of metals in liquid state.* Materials Transactions Jim, 1989. **30**(9): p. 647-659.

124. Maurice, D.R. and T.H. Courtney, *The phiscs of mechanical alloying - a 1st report.* Metallurgical Transactions a-Physical Metallurgy and Materials Science, 1990. **21**(2): p. 289-303.

125. Pekarskaya, E., C.P. Kim, and W.L. Johnson, *In situ transmission electron microscopy studies of shear bands in a bulk metallic glass based composite.* Journal of Materials Research, 2001. **16**(9): p. 2513-2518.

126. F.R. de Boer, R.B., W.C.M. Mattens , A.R. Miedema , A.K. Niessen *Cohesion in Metals : Transition Metal Alloys*1988, Oxford/GB: Elsevier Science & Technology. 758.

127. M. Wollgarten, K. L. Sahoo, H.E.M., *unpublished results.*

128. Zhuo, L.C., et al., *Effect of cooling rate on microstructure and mechanical properties of rapidly solidified Al-based bulk alloys.* Journal of Alloys and Compounds, 2010. **504**: p. S117-S122.

129. Carlson, T.A., et al., *Calculation of electron shake-off for elements from Z=2 to 92 with use of self-consistent field wave function.* Physical Review, 1968. **169**(1): p. 27-36.

130. Sadoc, A., et al., *Local order and nanostructure induced by microalloying in Al-Y-Fe amorphous alloys.* Journal of Non-Crystalline Solids, 2007. **353**(29): p. 2758-2766.

131. Greer, A.L., *Materuaks science - confusion by design.* Nature, 1993. **366**(6453): p. 303-304.

132. Greer, A.L., *Metallic glasses.* Science, 1995. **267**(5206): p. 1947-1953.

133. Li, R., et al., *Influence of similar atom substitution on glass formation in (La-Ce)-Al-Co bulk metallic glasses.* Acta Materialia, 2007. **55**(11): p. 3719-3726.

134. Zhang, T., A. Inoue, and T. Masumoto, *Amorphous Zr-Al-TM (TM = Co, Ni, Cu) alloys with significant supercooled liquid region of over 100-K.* Materials Transactions Jim, 1991. **32**(11): p. 1005-1010.

135. Nishiyama, N. and A. Inoue, *Glass-forming ability of bulk Pd40Ni10Cu30P20 alloy.* Materials Transactions Jim, 1996. **37**(10): p. 1531-1539.

136. Zhang, T., R. Li, and S.J. Pang, *Effect of similar elements on improving glass-forming ability of La-Ce-based alloys.* Journal of Alloys and Compounds, 2009. **483**(1-2): p. 60-63.

137. Takeuchi, A. and A. Inoue, *Quantitative evaluation of critical cooling rate for metallic glasses.* Materials Science and Engineering a-Structural Materials Properties Microstructure and Processing, 2001. **304**: p. 446-451.

138. Takeuchi, A. and A. Inoue, *Calculations of mixing enthalpy and mismatch entropy for ternary amorphous alloys.* Materials Transactions Jim, 2000. **41**(11): p. 1372-1378.

139. Boer, F.R.d., *Cohesion in metals : transition metal alloys*. 2nd, corr. print ed1988, Amsterdam ; Oxford: North-Holland. xvi, 758 p.

140. Vitek, V., American Society for Metals. Materials Science Division. Computer Simulation Technical Activity., and Metallurgical Society of AIME. Nuclear Metallurgy Committee., *Amorphous materials : modeling of structure and properties : proceedings of symposium*1983, Warrendale, Pa: Metallurgical Society of AIME. viii, 347 p.

141. Senkov, O.N. and D.B. Miracle, *Effect of the atomic size distribution on glass forming ability of amorphous metallic alloys.* Materials Research Bulletin, 2001. **36**(12): p. 2183-2198.

142. Senkov, O.N. and D.B. Miracle, *A topological model for metallic glass formation.* Journal of Non-Crystalline Solids, 2003. **317**(1-2): p. 34-39.

Declaration

Ich erkläre hiermit, dass ich die vorliegende Dissertation selbst verfasst und keine anderen als die angegebenen Quellen und Hilfsmittel verwendet habe.

Berlin, Oktober 2011

_____

Yao Liu